TECHNISCHE UNIVERSITÄT WIEN
Vienna University of Technology

D I P L O M A R B E I T

MATROSHKA – Astronaut Doses Onboard the ISS

Ausgeführt am

Atominstitut
der Technischen Universität Wien

unter der Anleitung von
Prof. Dr. Norbert Vana und Dr. Michael Hajek

durch

Lucas Martin Ellmeier

Brigittenauerlände 18/12, 1200 Wien

02.05.2011 _____

TABLE OF CONTENTS

EXECUTIVE SUMMARY

Radiation exposure ranks among the foremost dangers to human enterprise into space. Being able to determine the accumulated dose and dose rates for organs and other body tissues is paramount to further exploration and a permanent human presence in space. The Matroshka experiment aimed at gaining deeper understanding of the exposure to ionizing radiation as posed for a stay on the International Space Station (ISS) in Low Earth Orbit (LEO).

The mixed radiation field onboard a spacecraft (intravehicular activity- IVA) as well as the exposure during space walks (extravehicular activity- EVA) differs significantly from that found on earth.

Dose rates are increased by at least a factor of one hundred and further complications arise through the build-up of secondary particles in the shielding structure and the human body.

The presence of heavy charged particles (HCP) that form one major constituent of space radiation in addition to electrons and protons from the trapped radiation belts (van Allen belts), which are absent on earth, make special radiation protection considerations for crew members necessary due to the particles' high relative biological effectiveness (RBE).

The Matroshka phantom was designed to give a deep insight into the various processes at hand. Its anthropomorphic torso consists of 33 polyurethane slices. The density was chosen according to organ tissue and donor bones are embedded. Channels for passive radiation detectors namely thermoluminescence dosemeters (TLDs) and cut-outs for active instruments are embedded within the structure. Six additional organ dose boxes for passive dosemeters were installed at the sites of radiosensitive organs and the head, a poncho and hood including polyethylene stripes with sewed in TLDs and six dosemeter packages simulated the skin. A containment was used to cover the structure. For an EVA a multilayer insulation was added.

The Experiment was conducted in three main phases: an outside exposure (EVA) – Matroshka I (active and passive instruments), an inside exposure (IVA) onboard the Pirs module (passive instruments only) – Matroshka II-A - which is the focus of this work- and an IVA onboard the Zarya module (active and passive instruments) – Matroshka II-B.

In the frame of Matroshka Phase II-A the Institute of Atomic and Subatomic Physics provided 996 TLDs for dose measurements with high spatial resolution. Three types of TLDs were used in order to account for thermal and intermediate neutron components and HCPs. From January to December 2006, 337 days of exposure inside the Russian segment of the ISS were recorded.

In contrast to the results of Matroshka I (EVA), a much flatter dose gradient can be seen and doses especially to the skin and head are roughly two times lower than for the outside exposure. On average, the skin received a dose rate of 0.25 mGy/day. This dose rate represents a conservative estimate for the whole body exposure. Build up and thermalisation of neutrons is significant for the organs, foremost the intestines, where they make up roughly a third of the ^{60}Co- equivalent neutron absorbed dose. Dose related hot spots in the monitored organs were not found.

In the event of further prolonged missions in LEO and beyond, these findings represent a valuable source for mission planners and policy makers in the space sector as well as terrestrial applications i.e. radiotherapy or radiation monitoring onboard aircraft.

Scenarios for missions to Mars or a permanent lunar habitat have to rely on accurate risk estimates in order to safeguard human lives and to ensure minimizing long term stochastic radiation effects such as cancerogenesis and hereditary effects.

ACRONYMS

ATI	Institute of Atomic and Subatomic Physics (formerly: Atomic Institute of the Austrian Universities)
ATV	Automated Transfer Vehicle
AU	Astronomical Unit
CME	Coronal Mass Ejection
DIAS	Dublin Institute of Advanced Studies
DLR	Deutsches Zentrum für Luft- und Raumfahrt
ERB	Earth's trapped Radiation Belts
EVA	Extravehicular Activity
GCR	Galactic Cosmic Radiation
HCP	Heavy Charged Particles
ICRP	International Commission on Radiological Protection
ISS	International Space Station
IVA	Intravehicular Activity
JAXA	Japan Aerospace Exploration Agency
LEO	Low Earth Orbit
LET	Linear Energy Transfer
MIT	Massachusetts Institute of Technology
NASA	National Aeronautics and Space Administration
NCRP	National Council on Radiation Protection and Measurements
NIRS	National Institute of Radiological Sciences
SAA	South Atlantic Anomaly
SCR	Solar Cosmic Radiation
SPE	Solar Particle Event
RBE	Relative Biological Effectiveness
TLD	Thermoluminescence Dosemeter
TL	Thermoluminescence

1. INTRODUCTION

1.1 RADIATION ENVIRONMENT IN LOW EARTH ORBIT

The radiation environment in space is characterized by a wide variety of charged particles covering a wide range of energies. When passing through the mass of a spacecraft and its contents, these (primary) particles can participate in a number of different types of nuclear interaction, producing a complex environment of both charged and neutral secondary particles.

Vessels traversing a Low Earth Orbit (LEO), a spherical region that extends from the Earth's surface up to an altitude of 2,000 km [1], will experience an altered radiation field than in free space. The main cause of this is earth's magnetosphere and the resulting (anisotropic) trapped radiation belts as we will see in this section. For a given mission a large number of parameters have to be taken into consideration: The inclination and altitude of the orbit, the orientation of the spacecraft relative to the Earth and the Sun and the particular phase of the 11- year solar cycle.

1.1.1 SPACE RADIATION COMPONENTS

Although components of space radiation in LEO vary significantly in terms of energy and particle species it is useful to place them into three main categories according to source: (1) trapped particles, (2) galactic cosmic radiation (GCR) and (3) solar particle events (SPE) as can be seen in Fig. 1.1.1.

In LEO a fourth source, albedo neutrons and protons, is sometimes mentioned. These are secondary particles produced in interactions between GCRs and Earth's atmosphere with trajectories that take them back up into space. The albedo component is small and of comparatively low energy and as such is not considered a significant source of radiation exposure.

A summarising chart (tab.1.1.1) and a graph of particle flux and energy of the different space radiation components (fig. 1.1.5) are presented at the end of this section to give an overview.
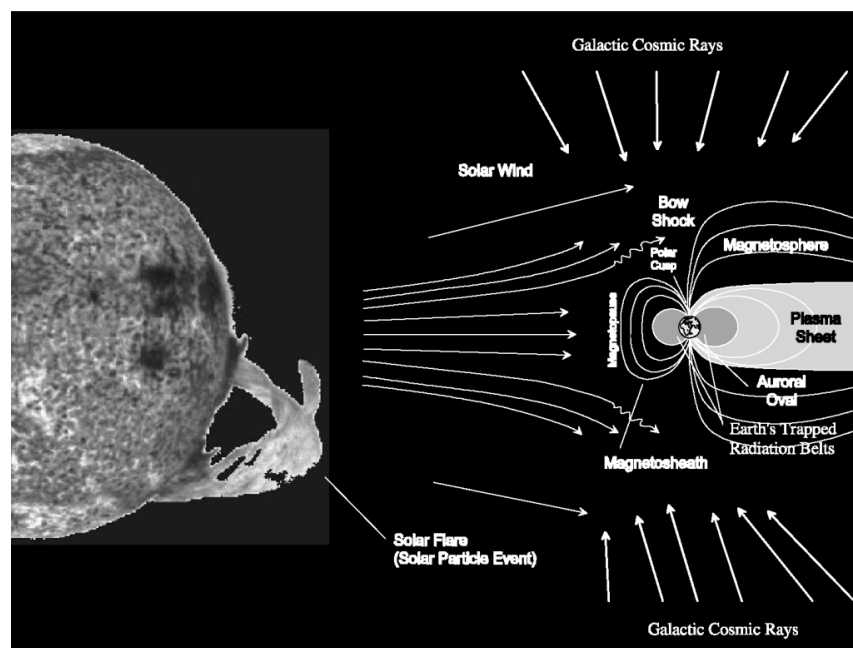

Fig. 1.1.1 The Earth's magnetosphere is compressed on the sunlit side (Bowshock). Radiation belts, GCR and SPEs constitute the main components of radiation in LEO [3].

1.1.1.1 TRAPPED PARTICLES

The Earth is surrounded by intense regions of energetic protons and electrons referred to as the Van Allen Belts or the Earth's trapped radiation belts (ERBs). These particles are trapped by the geomagnetic field where they follow a complex motion, illustrated in Fig. 1.2 . Other heavier ions e.g. helium, carbon and oxygen are also observed. The most plausible source of protons and electrons at lower altitudes is the decay of albedo neutrons produced by nuclear reactions between GCR and atmospheric components. At higher altitudes the ionosphere and the solar wind constitute for the trapped particles. Collision in the atmosphere, wave particle interactions as well as large geomagnetic storms can be seen as feasible loss mechanisms [2].

The geomagnetic field of Earth is roughly equivalent to that of a dipole and the field lines converge near the poles. This causes the charged particles to move back and forth along the field lines in a cyclotron motion, reversing their directions at mirror points near the poles. Finally there is a drift of the protons to the west and of the electrons to the east.

Trapped electrons occur in two belts or zones. The first, inner zone extends to about 2.4 Earth radii (R_E ~ 6370 km) and consists mostly of electrons with energies less than ~5 MeV. The second or outer zone extends from about 2.8 to 12 R_E and contains electrons with energies up to about 7 MeV. Electron flux is approximately an order of magnitude greater in the outer zone than in the inner zone. Most of the flux lies below the energy (~10 MeV) where bremsstrahlung production becomes important. Considering this it becomes clear that in LEO trapped electrons do not play a substantial part in overall exposure [2].

Trapped protons occur in only a single region that decreases in intensity as a function of distance from the Earth, which is identical with the inner zone mentioned above. Trapped protons extend in energy from several to several hundred MeV and form a broad peak between 150 and 250 MeV. Taking into consideration the arguments presented above, overall exposure onboard a space station (altitude ~400km) from this source should be insignificant. However, due to the fact that the dipole axis is slightly displaced from the Earth's axis of rotation causing the ERBs to get to unusually low altitudes there is a region off the coast of Brazil which is called the South Atlantic Anomaly (SAA). In the SAA the trapped proton belt intersects the orbits of low-altitude spacecraft such as the Space Shuttle and the International Space Station (ISS). For the 51.56° inclination, ~400 km altitude orbit of the ISS half of the ionizing radiation dose is received from the trapped proton belt in the SAA (and half is from GCR at higher latitudes) [3].
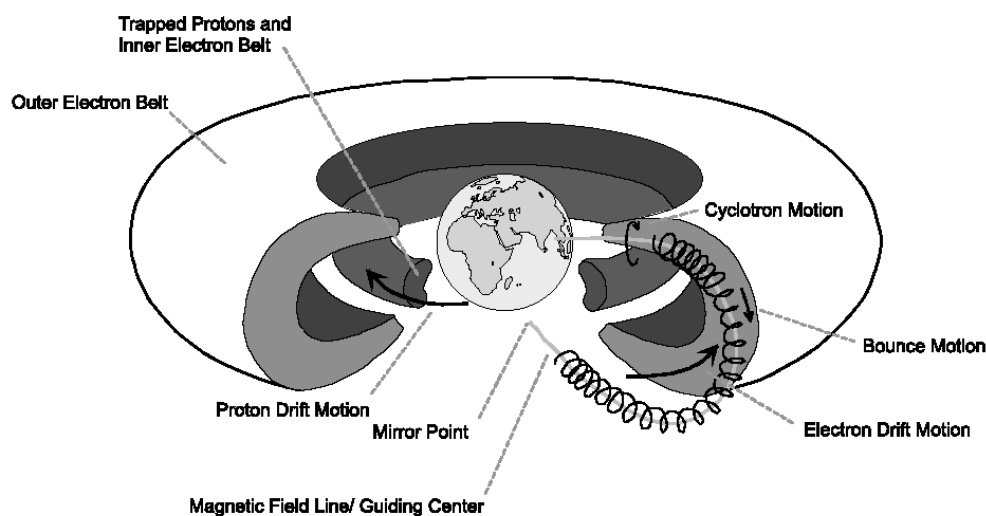

Fig. 1.1.2 The trapped radiation belts of Earth's magnetic field [3].

Models of the ERB have been developed, most notably the static omnidirectional AP-8 proton and AE-8 electron flux maps, but have proven to be insufficient due to the east-west anisotropy which leads to differences in doses received by different parts of the spacecraft [4].

1.1.1.2 GALACTIC COSMIC RAYS

Interstellar space is filled with high-energy charged particles, collectively called galactic cosmic radiation (GCR), ranging from protons (Z=1) to uranium ions (Z=92). Its distribution is believed to be isotropic and they originate from galactic sources. It consists of 98 percent protons and heavier ions (baryon component) and two percent electrons and positrons (lepton component). They baryon component is composed of 87% protons, 12% helium ions (alpha particles) and the remaining 1% heavy ions of charge 3 (Li) – 92 (U). Fig. 1.1.3 shows the relative abundance of GCR [20]. Highly energetic particles in the heavy ion component, referred to as Heavy Charged Particles (HCPs), play a particularly important role in space dosimetry since they transmit high energies and are highly penetrating. Furthermore, they do not exist in the natural radiation environment on Earth and therefore require special consideration for shielding. Their energy spectra in free space, outside earth's magnetosphere range from several tens up to 10^{14} MeV and, within the solar system, the GCR spectrum is peaked around 100 MeV [2].
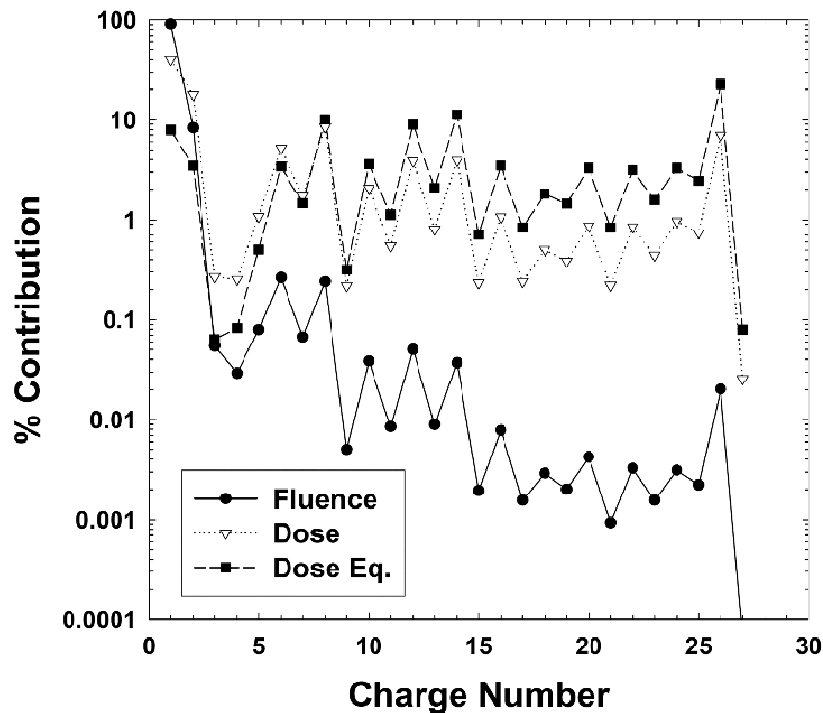
Fig. 1.1.3 Contributions from individual GCR elements for the particle flux, dose and dose equivalent at solar minimum [20].

GCR fluence rates are modified by the changing intensity of the solar wind and solar magnetic field (fig. 1.1.4). Maximum fluence is observed during solar minimum activity and minimum fluence during solar maximum activity. There are three main processes controlling the modulation: (1) diffusion of the particles through the scattering centres in the vicinity of Earth; (2) convection of the particles by the solar wind which is moving outward from the sun at roughly 400 km/s; and (3) adiabatic deceleration caused by the expansion of the solar wind, effectively "cooling" the GCR. Energy losses can add up to effectively "shield" the inner solar system [2].

Fig. 1.1.4 Solar activity modulation of GCR [3].

1.1.1.3 SOLAR PARTICLES

Solar particles are a regular component of the Solar Cosmic Radiation (SCR). SCR is emitted as solar wind and consists of electrons, protons, some heavier nuclei and electromagnetic waves over virtually all wavelengths. Althoug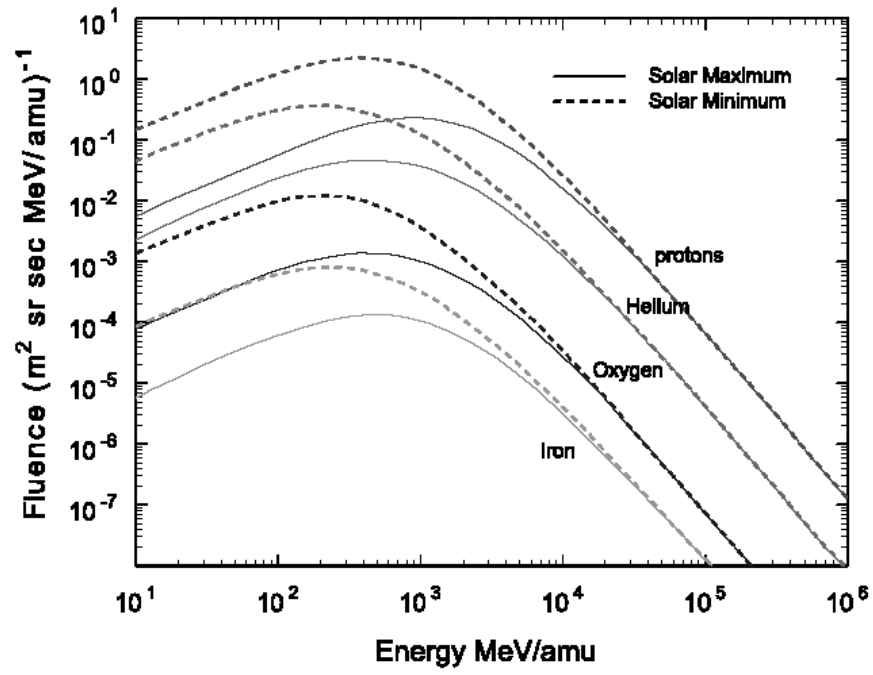h most of the regular particle flux of the sun is treated in the frame of trapped radiation sporadic outbursts from the solar corona, so-called solar particle events (SPEs), comprising the effects of solar flares and coronal mass ejections (CMEs), are a contributor to radiation levels in LEO therefore making it the third main component.

During an SPE, large amounts of energy are released in the form of electromagnetic waves (radio waves, gamma- and X-rays), energetic particles (electrons and protons) and mass flows. As electromagnetic emissions propagate faster (at the speed of light) and are not deflected by the interplanetary magnetic field they may be utilized advantageously for space weather alerts and warnings.

As can be seen in Fig. 1.5 SPEs seem to be correlated to general sun activity and approximately 50 such events can be expected over the course of a single solar cycle. A major SPE is defined as an event having a proton fluence of 10^{10} cm^{-2} (energies >10 MeV) [3]. One or two events can be expected per cycle.
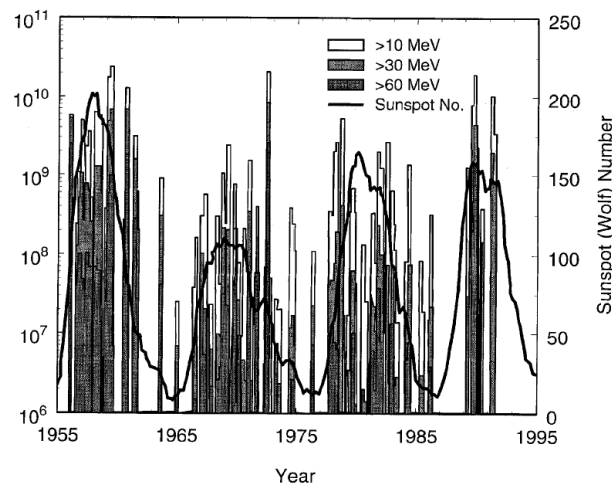
Fig. 1.1.5 Major SPEs over four solar cycles [3].

Fig. 1.6 depicts the general characteristic of a SPE build-up and decay. After an initial delay between solar flare and detected flux increase, a sharp rise followed by a smooth decrease is seen lasting up to a couple of days in the case of large CMEs but just hours for a small impulsive flare. The latter is of much less importance to radiation levels experienced in LEO.

Fig. 1.1.6 Behaviour of an SPE over time at a distance of 1 AU (mean distance Sun –Earth ~150 million km) [2].

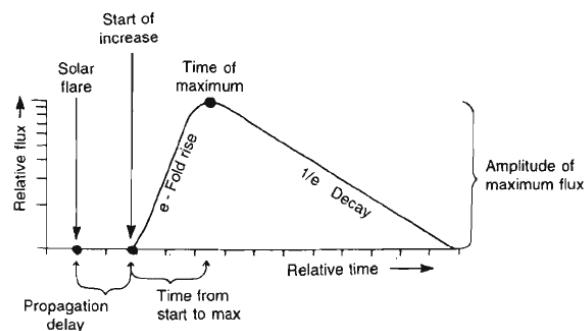|	Galactic cosmic rays	Earth's radiation belts	Solar particle events
Primary composition	98% hadrons $\begin{cases} \text{87% protons} \\ \text{12% } \alpha\text{-particles} \\ \text{1% heavy ions} \end{cases}$ 2% leptons (electrons and positrons)	• Electrons <6 MeV • Protons <250 MeV	• Mostly low-energy protons & electrons • Rarely higher-energy protons • Some heavy ions
Effect of solar cycle	• Flux inversely proportional to solar cycle • Solar modulation affects ⩽1 GeV/n component	• Solar cycle affects atmospheric scale height and east/west proton anisotropy • Creation of temporary belts during solar max	Frequency and magnitude of SPE proportional to solar cycle • High probability at solar max • Low probability at solar min
Effect of geomagnetic field	Protection in LEO due to cutoff Rigidity, function of geomagnetic latitude	• Raison d'être • South Atlantic Anomaly	Protection in LEO due to cutoff Rigidity, function of geomagnetic latitude
Effect of spacecraft shielding	• Little attenuation through ionization • Projectile and Target Fragmentation by heavy ions • Target fragmentation by protons	• Electrons fully attenuated, some production of Bremsstrahlung • Attenuation of low-energy protons • Target fragmentation by higher-energy protons	• Low-energy protons attenuated • Higher-energy protons and heavy ions can undergo nuclear interactions
Models/predictive capability	Good agreement with measurements • Badhwar/O'Neill • CREME96 (Nymmik)	Electrons: AE-8 (empirical model, old dataset, some refinements) Protons: AP-8 (empirical model, old dataset, some refinements) underpredicts at solar max overpredicts at solar min	Little predictive capability • NOAA Space Environment Center • GOES satellites • Neutron ground monitors
Relative contribution in LEO	• Dominates for high-inclination orbits • ~50% of ISS dose	• Dominates for low-inclination, high-altitude orbits • ~50% of ISS dose	• More severe in higher-inclination orbits • Unknown contribution to ISS Dose
	In LEO, relative contributions from all sources are dependent on orbital parameters (orbital inclination, altitude), spacecraft orientation, solar cycle and temporal variations in the geomagnetic field in a highly complex way.		
Relative contribution in free space	Omnipresent	N/A	Presents potentially large risk, especially during solar maximum
	In free space, relative contributions dependent on solar modulation and spacecraft shielding		

Tab. 1.1.1 The space radiation environment in LEO and in interplanetary space [3].
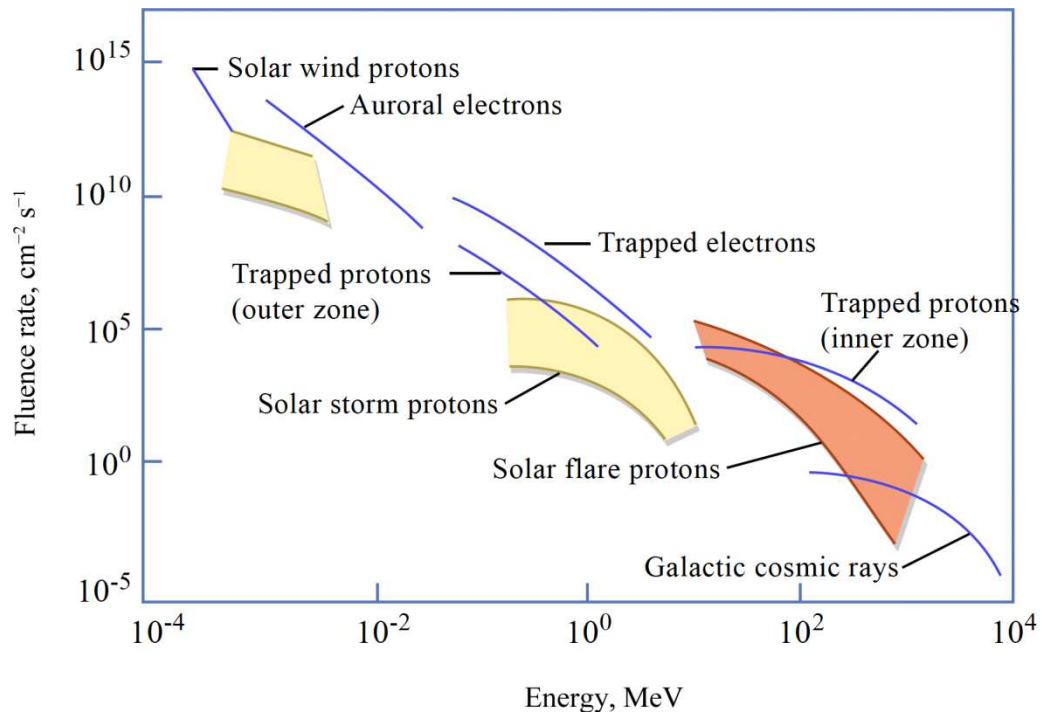
Fig. 1.1.5 Graph of flux over particle energy for different types of space radiation; radiation with higher particle energy tends to have lower flux. [courtesy MIT open course ware].

1.1.2 SECONDARY PARTICLE GENERATION WITHIN SHIELDING STRUCTURE

Most of the energy losses experienced by primary particles as they pass through the shielding of a spacecraft take the form of ionization. However, the energies of many of these particles are sufficiently high and they amount of shielding material is sufficiently large that a fraction of these primary particles will undergo nuclear interactions with the constituent nuclei of the spacecraft and its constituents, producing secondary particles [3]. The production of secondaries is summarized in Fig. 1.9. A more detailed look at the physical processes at hand will be given in section 1.2.1 for a qualitative approach suffices for now.

Primary Particles
Protons (from trapped (SAA), GCR, SPE, Albedo)
He nuclei & HZE particles (from GCR, rarely from SPE)
Electrons (from trapped)
Neutrons (from Albedo)

Spacecraft Skin

Spacecraft Structure, Equipment, Supplies...

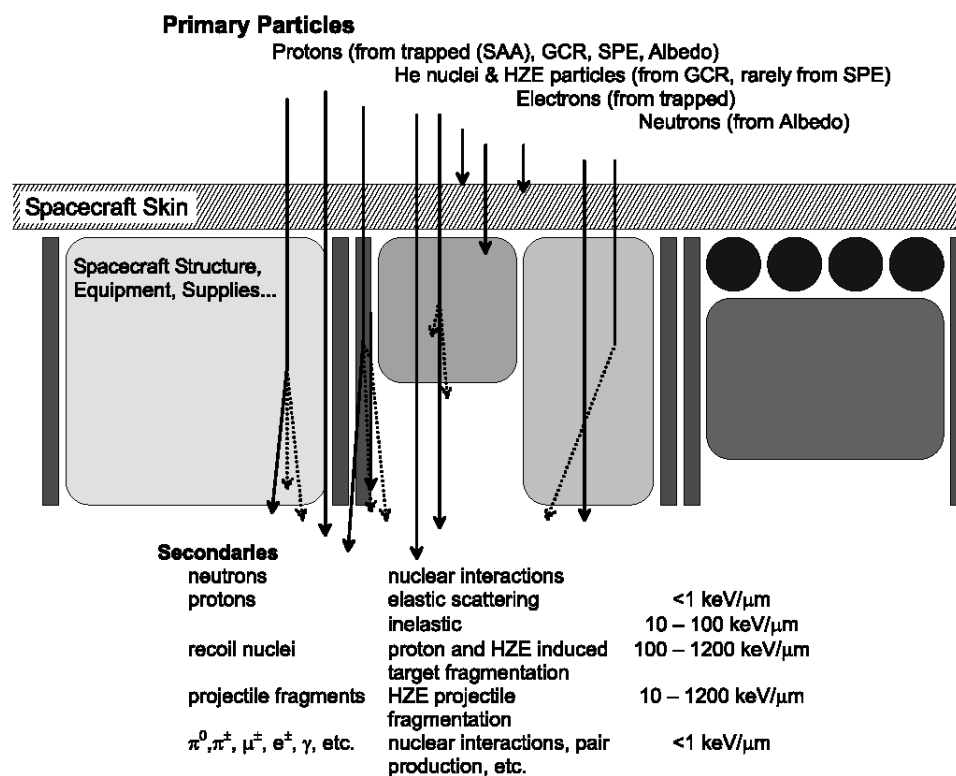| Secondaries		
neutrons	nuclear interactions	
protons	elastic scattering	<1 keV/µm
	inelastic	10 – 100 keV/µm
recoil nuclei	proton and HZE induced target fragmentation	100 – 1200 keV/µm
projectile fragments	HZE projectile fragmentation	10 – 1200 keV/µm
$\pi^0, \pi^\pm, \mu^\pm, e^\pm, \gamma$, etc.	nuclear interactions, pair production, etc.	<1 keV/µm

Fig. 1.1.9 The transport of primary radiation through the spacecraft structure and contents and the generation of secondaries. The most important secondaries in terms of radiation protection are neutrons and fragments from targets and projectiles. HZE particles refer to highly energetic ions heavier than helium [3].

Two types of nuclear interaction between primary charged particles and target nuclei of the spacecraft are of importance – target fragmentation and projectile fragmentation.

Target fragmentation occurs when a high-energy charged primary, typically a trapped or GCR proton, collides with a heavy nucleus such as an aluminium nucleus of the spacecraft structure. Depending on the kinetic energy of the primary charged particle, the nuclear interaction can follow a number of different channels, producing two or more secondary particles. These secondaries can include knockout protons, neutrons and alpha-particles, as well as recoil heavy nuclei.

Projectile fragmentation occurs when a HCP collides with a target nucleus. Again, depending on the energy and charge of the primary particle and the angle of the collision, a large number of reaction channels are possible. In addition to producing high-energy neutrons and protons, these reactions can also produce larger projectile fragments that retain much of the kinetic energy of the primary HCP.

The secondaries continue to traverse the spacecraft and may themselves undergo further nuclear reactions. This especially is valid for high-energy neutrons. Furthermore albedo effects can be assumed from the interior of the vessel making the orientation of instruments and compartments, i.e. interior design considerations, an important factor for radiation protection.

The spacecraft shielding structure should be seen as a transport medium rather than a barrier for it enables cascades of multiple reactions of which secondary neutron production is the most prominent. The neutron spectrum inside spacecraft can be considered to occupy several energy intervals: (1) evaporation neutrons of energy between 1 and about 20 MeV, (2) intranuclear cascade neutrons of energies between 20 and 200 MeV, (3) neutrons from fragmentation of high-energy GCR ranging in energy from between 500 MeV and 5 GeV and (4) moderated neutrons with energy <1 MeV (thermal, intermediate < 200 keV included). It is estimated that neutrons in each of the first three energy regions make a roughly equal contribution to dose equivalent [3].

1.2 RADIATION DOSIMETRY

Radiation components (charged and neutral particles, electromagnetic waves) have a wide variety of interactions with target atoms as is the case with space vessels, equipment and human tissue. Definitions will be given in this section to qualitatively and quantitatively assess these. Predominantly, interaction processes take the form of ionization. This has to be further distinguished between direct and indirect ionization according to the type of radiation involved. Radiation dosimetry aims at measuring these energetic incidents and to asses the central quantity – the dose. By doing so it becomes possible to assess risks posed to humans and to use ionising radiation for medical therapy.

By pushing the limits of human endeavour and exploration beyond earth's atmosphere, space dosimetry becomes a keystone to any attempt to maintain an endured human presence in outer space and a lot of experimental data has been retrieved to consolidate our present knowledge, though large uncertainties remain.

1.2.1 CONCEPTS AND METHODS

Radiation that penetrates material excites and ionizes molecules and atoms along their path. Thus all types of radiation that cause ionization are subsumed under the term ionizing radiation. A distinction is made between direct and indirect ionizing radiation (fig. 1.2.1) and further between sparsely and densely ionizing radiation. A Monte Carlo simulation of the track structure of an HCP is given in comparison to one of an electron to illustrate the difference (fig 1.2.2).

The ionization energy of soft tissue is 12.4 eV (≤ 100 nm wavelength) below that threshold any type of radiation is called non-ionizing radiation [19].

Directly ionizing radiation consists of charged particles with a finite rest mass (α, β^-, β^+ -particles, protons, etc.). Its kinetic energy is high enough to cause ionization by collision.

Indirectly ionizing radiation consists of neutral particles with finite rest mass (neutrons) or photons (gamma and X-rays) with rest mass zero, which release energetic charged particles or cause nuclei fragmentation.
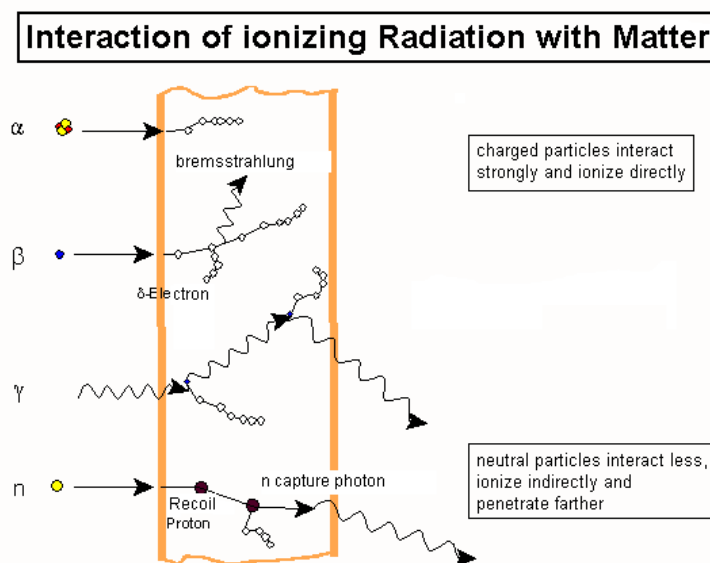

Fig. 1.2.1 Interaction of ionizing radiation with matter.

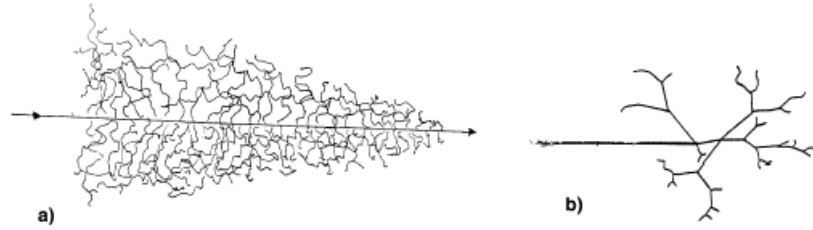**Fig. 1.2.2** Monte Carlo-simulated tracks of (a) a typical HCP and of (b) an electron [17].

Sparsely ionizing radiation is defined by <200 ion-pair incidents per micrometer and densely ionizing radiation by >200 such incidents per micrometer [26].

As radiation penetrates material it interacts with atoms. These interactions change the incoming radiation as well as the penetrated material. The radiation undergoes energy-losses and scattering processes. Energy is transferred to the interaction material causing it to heat up or change its physical, chemical and biological properties [6].

Interaction of Charged Particles with Atoms

Charged particles interact with target shell electrons and nuclei. Four different types of interaction can be distinguished.

<u>Inelastic Collisions with Shell Electrons</u>

Inelastic collisions of charged particles lead to excitation or ionization of atoms. Their deceleration is called collision stopping power S_{coll}. Heavier charged particles such as protons, deuterons, alpha-particles of fission products loose their energies primarily through this process. Each ionization event transmits only a small fraction of the kinetic energy of the penetrating particle, thus a high number of such events (for example a 1 MeV particle may undergo as many as 10^4 single collisions) is necessary to stop the particle completely. Particles with a high mass compared to an electron will not suffer much scattering. The mean differential energy-loss per unit path length can be computed by applying the Bethe-Bloch formula:

$$S_{coll} = -\left(\frac{\overline{dE}}{dx}\right)_{Coll} = \left(\frac{1}{4\pi\varepsilon_0}\right)^2 \frac{4\pi e_0{}^4 z^2}{m_e v^2} N_A Z (ln\frac{2m_e v^2}{\overline{I}(1-\beta^2)} - \beta^2)$$

ε_0...electric constant, ~8.85 10^{-12} As/(Vm)

e_0...elementary charge, ~1.60 10^{-19}C

z...charge of incident particle

v...velocity of incident particle

N_A...density of atoms of target material

Z...charge of atoms of target material

β...relativistic relation v/c_0, c_0...vacuum speed of light, 299,792,458 m/s

$\overline{I}$...mean ionization energy per target atom, empirical relation $\overline{I} = k_1 Z (1 + k_2 Z^{-\frac{2}{3}})$, k_1=7,6 eV, k_2=0,6;

The relativistic expression can be simplified considering velocities considerably smaller than the speed of light.

The Bethe-Bloch formula shows that energy loss via ionization is independent of the mass of the incident particle. It depends primarily on charge and velocity. The influence of the interaction material is described by the factor:

$$N_A Z = \frac{1}{A_r m_u} \rho Z$$

A_r...relative atomic mass

m_u...atomic mass number, ~1.66 10^{-27} kg

ρ...density

A high ratio of Z/A$_r$ (i.e. hydrogen) and a high density maximise the stopping power of an irradiated material.

The stopping power is proportional to the creation of ion pairs per unit length in first approximation. This measure is called specific ionization s.

$$-\left(\overline{\frac{dE}{dx}}\right)_{Coll} = s\overline{W_l}$$

$\overline{W_l}$ depicts the mean energy input for the creation of an ion pair and is ~30eV for common gases such as hydrogen and oxygen and roughly a tenth for solids.

The specific stopping power is proportional to $1/v^2$. At the end of the particle range the velocity decreases steadily and therefore s increases. This curve progression is called Bragg-curve with its distinct Bragg-peak (see fig. 1.2.3)
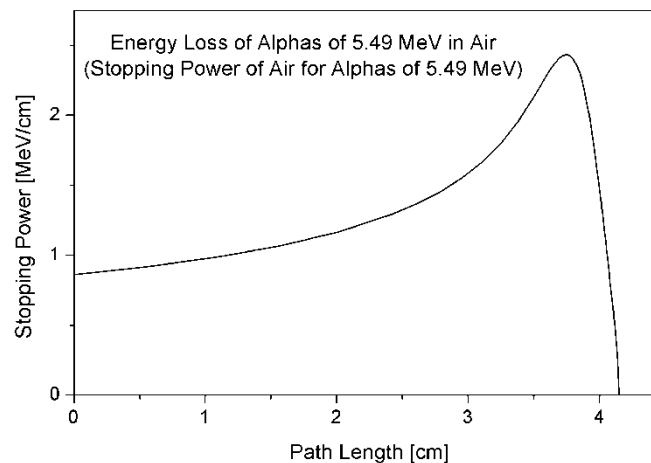
Fig. 1.2.3 Bragg curve and peak for alpha particles in air.

When the energy of an incident particle becomes very low it can capture shell electrons so that its z value decreases and thus ionization events decrease explaining the sudden drop after the peak of the curve.

Primary electrons that have been generated by incident charged particles can cause further ionization. Such electrons are referred to as δ- electrons. Therefore a distinction has to be made between specific primary ionization and total ionization. Electrons with energies 10 keV < E < 1 MeV loose their energy primarily through inelastic collisions with shell electrons and cause excitation and ionization. Due to their small mass they are highly scattered [6].

Inelastic Collisions with Nuclei

Charged particles with mass m and nuclear charge z experience a change of direction in the Coulomb field of nuclei. The attached deceleration is proportional to

$$\frac{zZ}{m}$$

The energy loss per unit length becomes

$$-\left(\frac{\overline{dE}}{dx}\right)_{Coll} \sim \frac{z^2 Z^2}{m^2}$$

and increases with particle energy. According to classical electrodynamics decelerated charged particles emit radiation called bremsstrahlung. Thus it becomes clear that bremsstrahlung is only relevant for incident light charged particles. Electrons loosing their energy via inelastic collisions will most likely undergo many such collisions whereas electrons loosing their energy via bremsstrahlung can do so in one interaction. Depending on target material there is a threshold energy for an equilibrium of both interactions above which bremsstrahlung dominates. Low-energetic electrons will predominately loose their energy via inelastic collisions [6].

Elastic Collisions with Shell Electrons

This interaction is only important with very low energies. The entire target atom is involved in the collision and a very small pulse transmission occurs [6].

Elastic Collisions with Nuclei

Incident particles are scattered and transfer parts of their energy to the target nuclei. Heavy particles are much less scattered than light ones. No ionization is caused [6].

Interaction of Neutrons with Atoms

Due to the fact that neutrons carry no electric charge they do not interact with matter through the interactions derived above. Only interactions with atomic nuclei play a role thereby creating secondary particles that can further excite and ionize [6].

Elastic Scattering with Nuclei

Elastic scattering leads to a change in trajectory and energy of the incident neutron. The sum of kinetic energies remains constant. On average a fast neutron of some MeV is decelerated after only 25 collisions with hydrogen atoms to thermal energy of molecules. This is called neutron moderation [6].

Inelastic Scattering with Nuclei

Inelastic Scattering leads to a change in trajectory and energy of the incident neutron as well. The energy losses will result in nuclear excitation thus reducing the total sum of kinetic energies. The excited nuclei return to their ground state by emitting characteristic gamma-rays [6].

Absorption of Neutrons

There is a third interaction process that neutrons can engage in. They can enter target nuclei and initiate nuclei reactions such as capture, exchange and fission [6].

Interaction of Photons with Atoms

High-energy photons such as gamma and X-rays have a multitude of interaction mechanisms. Partners of such interactions are shell electrons, Coulomb fields in the atom and nucleons. The most important are the photoelectric effect, the Compton effect, pair production and the photodisintegration. Their range is determined by incident photon energy and the atomic number of target materials as can be seen in figure 1.2.4.

Attenuation of photons follows an exponential law

$$\varphi(x) = \varphi(0)e^{-\mu x}$$

$\varphi(x)$...photon flux after traversing material with layer thickness x

$\varphi(0)$...initial photon flux

μ...linear attenuation coefficient

The linear attenuation coefficient μ derives as follows

$$\mu = N_a \sigma_{ta} = \sigma_{ta} \frac{\rho}{A_r m_u} = \sigma_{te} \frac{Z\rho}{A_r m_u}$$

σ_{ta}...total atomic cross section

σ_{te}...atomic cross section per unit charge

As opposed to particle radiation a maximum range cannot be obtained and measures attenuation lengths are commonly used [6].
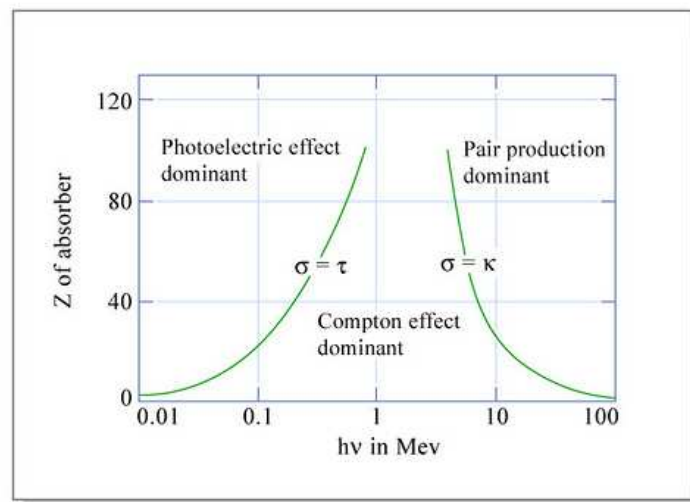

Fig. 1.2.4 Range of different photon – atom interactions (the abscissa denominates the energy of the incident atom in MeV and the ordinate the atomic number Z of the absorber) [courtesy MIT open course ware].

Deposition of Radiation Energy

The central quantity with ionizing radiation is the dose (absorbed/transferred energy per unit mass). However, there is a difference between energy transferred and energy deposited. The spatial distribution of deposition events is a significant aspect that is macroscopically explained by the linear energy transfer (LET). In microscopic dimensions the stochastic nature of energy deposition events becomes important as becomes evident in the energy deposition in the vicinity of a track of an ionizing particle as we have already seen in fig. 1.2.2. Taking this into consideration the concept of microdosimetry is introduced.

Definitions

The **dose *D*** is defined as the expectation value of the absorbed energy dE_{abs} divided by the mass dm of the volume:

$$D = \frac{\overline{dE_{abs}}}{dm}$$

Its unit is **Joule/kg** which equals the special name: **Gray (Gy)**.

The introduction of the expectation value follows from the stochastic nature of energy deposition and will be further discussed in the framework of microdosimetry.

The absorbed dose rate is given in Gy/unit time; mGy/d will be used in this work.

Only part of the incident energy is absorbed in a given mass element since secondary particles and photons may leave the volume carrying away a certain fraction of the originally transferred energy. Here it becomes evident that a clear distinction has to be made between transferred and deposited energy. Only if the path of any secondary particles lies entirely inside the mass element under consideration and no radiative losses occur, transferred and deposited energy equal each other.

To account for the total energy transferred to secondary particles a special quantity is defined. It is called **KERMA** (**kinetic energy released in matter per unit mass**) and is measured as well in J/kg.

Only if secondary particle equilibrium is obtained – i.e. for every secondary particle leaving the mass element another particle of the same type and energy enters - and bremsstrahlung losses are negligible, KERMA and absorbed dose are identical.

Spatial distribution of energy is accounted for within the concept of **linear energy transfer** (**LET**). It is defined as the amount of <u>locally</u> absorbed energy per unit length. An absorber material (water is often used) is given for reference. Its unit is **eV/m** (keV/μm is commonly used). Kinetic energy leaving the particular volume is excluded. A generally applicable definition of the term 'local' is not possible, for this would require specification of site dimensions. In the case of electrons a boundary of 100 eV is considered widely as to be local.

The total transferred energy per unit length is the stopping power as we have already come to understand in this section. It is numerically equal to LET_{∞}, i.e. without restriction.

$$LET_{\infty} \mathrel{\widehat{=}} S_{coll}$$

There are differences however concerning the very conceptual nature of these quantities. LET focuses on energy deposited while stopping power accounts for the energy loss of the incident particle.

Energies exceeding 'local' deposition have to be indicated by their cut-off energies and their values in eV appear in a subscript to LET.

Underlying the LET concept is the notion that energy deposition is a continuous process and stochastic variations are not taken into account. This limits its applicability especially when dealing with very small sites as for example biological cells.

In submicroscopical dimensions the macroscopic quantity dose looses its validity since we are dealing with energies that are deposited in very small volumes. A more appropriate approach considers the stochastic nature of the interaction processes at hand. This branch of radiation dosimetry is called microdosimetry.

The microscopic counterpart of absorbed dose is the **specific energy z.** It is defined as the energy dE deposited locally in a small volume divided by its mass dm.

$$z = \frac{dE}{dm}$$

z is a stochastic quantity fluctuating according to statistical laws which may be described by a distribution function. It turns out that the expectation value of z^2 depends in a linear-quadratic fashion ($\sim z^2 = \bar{z}d + d^2$) on the dose and that the linear term is governed by the dose-mean of the single event distribution.

The microscopical counterpart to LET is the **lineal energy y**. It is defined as the energy deposited in a specified spherical volume divided by the mean path length of random traversals.

1.2.2 BIOLOGICAL RELEVANCE OF ENERGETIC CHARGED PARTICLES

Different concepts have been developed to account for the biological impacts of ionizing radiation. Radiation hazards to biological organisms do not only depend on the dose received over time but also on the type of radiation.

The **relative biological effectiveness** (**RBE**) is a factor used to compare the biological effectiveness of absorbed radiation doses from different types of ionizing radiation; more specifically, the experimentally determined ratio of an absorbed dose of a radiation in question (D_T) to the absorbed dose of a reference radiation (D_X) required to produce an identical biological effect; if 10 mGy of fast neutrons equaled in lethality to 20 mGy 250 kV X-rays (or ^{60}Co), the RBE of the fast neutrons would be two [2]. Thus:

$$RBE = \frac{D_X}{D_T}$$

The RBE is only valid for specific biological endpoints. After taking into account all available biological information you can choose an envelope curve of the data for achieving realistic risk estimates.

Consequently the **quality factor** (**Q**) for stochastic effects was thus introduced to weight the dose D. The product of Q and D at a point in tissue (muscle tissue is usually taken as the absorbing material though bone marrow and other tissues are used when appropriate) results in a protection quantity, the **dose equivalent** (**H**). The name for this special unit of dose is the **Sievert** (**Sv** [J/kg]). Recommended values for Q have generally been made in terms of LET_∞.

$$Q = f(LET)$$

The dependence of Q on LET - as given in reports of the International Commission on Radiological Protection (ICRP), namely ICRP 26 and ICRP 60 - is shown in figure 1.2.5 .
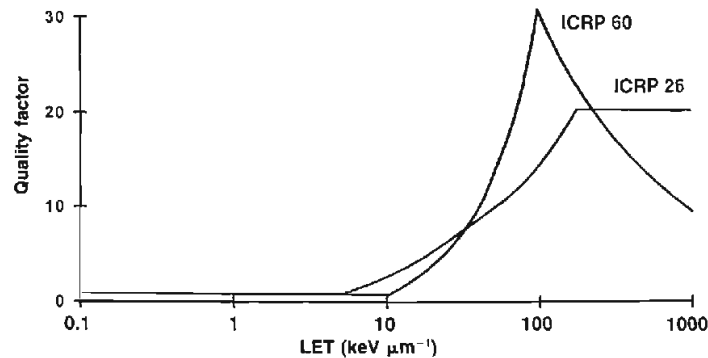
Fig. 1.2.5 Q as a function of LET (ICRP 60 and ICRP 26) [2].

Radiation weighting factors ω_R based on a review of the biological information, a variety of exposure circumstances and inspection of the results of traditional calculations of the ambient dose equivalent are introduced. Table 1.2.1 shows the ω_R values for different types of radiation. The NCRP endorses the ω_R values of the ICRP 60 [2]. The product of ω_R and the dose averaged over a specific organ or tissue (T) due to a radiation (R) incident is called **equivalent dose [Sv]** in a tissue or organ T and is denoted **H_T**.

$$H_T = \omega_R D_{T,R}$$

Type and Energy Range	ω_R
Photons, all energies	1
Electrons, positrons and muons, all energies	1
Neutrons, energy <10 keV	5
10 keV to 100 keV	10
>100 KeV to 2 MeV	20
>2 MeV to 20 MeV	10
>20 MeV	5
Protons, other than recoil protons, energy >2 MeV	5
Alpha particles, fission fragments, nonrelativistic heavy nuclei	20

Tab. 1.2.1 Radiation weighting factors [27].

The **effective dose** (**E**) is intended to handle nonuniform irradiation situations and is defined as the sum of weighted H_T for all irradiated tissues or organs. The **tissue weighting factor ω_T** weighs the different effect on each organ and tissue including the different mortality and morbidity risks from cancer and the length of life lost due to these effects (tab. 1.2.2) [2].

Tissue or Organ	ω_T
Bone surface, Skin	0.01
Bladder, Breast, Liver, Esophagus, Thyroid, Remainder (e.g. brain, kidney, small and large intestine...)	0.05
Bone marrow, Colon, Lung, Stomach	0.12
Gonads	0.20
$\Sigma =$	1.00

Tab. 1.2.2. ω_T for different tissues and organs [27].

To give a general overview of the system of dose quantities tab. 1.2.3 is presented. The **collective effective dose** is added at the bottom for completeness.
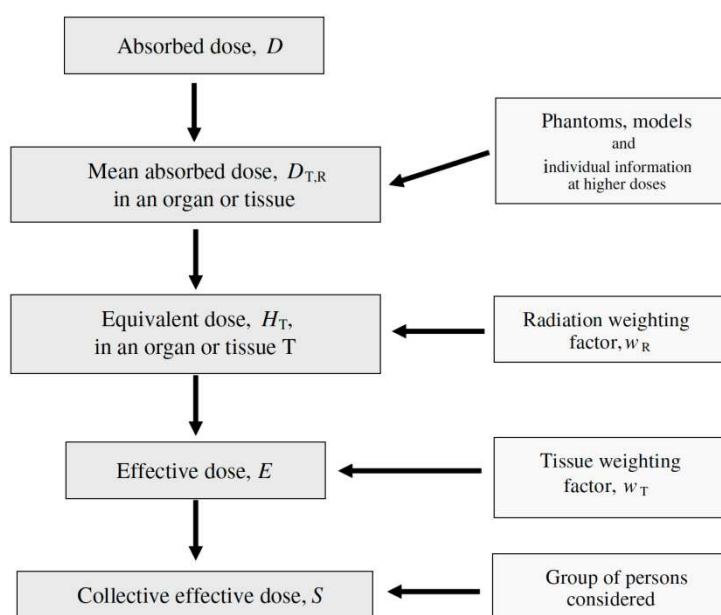
Tab. 1.2.3 The system of dose quantities for use in radiological protection.

Biological Effects of Ionizing Radiation

A clear distinction has to be made between deterministic and stochastic effects of ionizing radiation to biological systems.

Deterministic effects develop due to cell killing by high dose radiation, commonly appear above a given threshold dose, which is considerably higher than doses from natural radiation or from occupational exposure at normal operation. The severity of the effect depends on the dose, at a given high dose the effect is observed in severe form in all exposed cells, at higher doses the effect cannot increase.

Stochastic effects develop due to mutation effects in irradiated cells which cause cancer and hereditary effects. The severity of the effect does not depend on the dose, but the frequency of the appearance of the (probabilistic) effect in the exposed population group is dose dependent, (in most cases) linearly increasing with the dose. Since the spontaneous incidence of cancer in the general population is ~20%, low dose effects are 'submerged' in this occurrence. A linear no threshold model is assumed, though [2].

A timescale of radiation effects/actions is given in fig. 1.2.7 to illustrate the physical, chemical and biological reactions to irradiation.
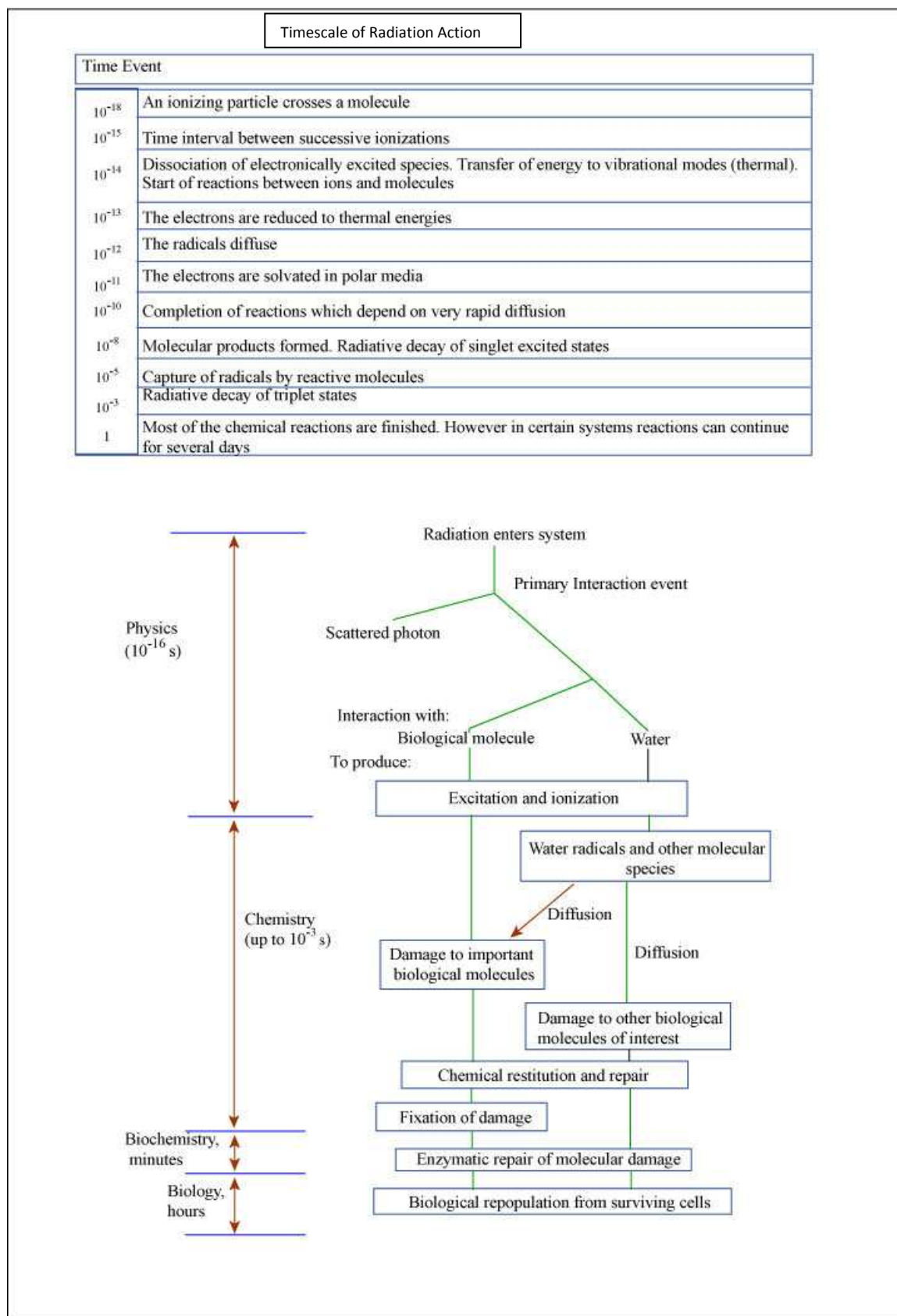
Fig. 1.2.7 Timescale of radiation action [courtesy MIT open course ware]

1.2.3 DOSIMETRIC EXPERIMENTS IN SPACE

Many space dosimetry data have been gathered over the past several decades mostly in the form of dose or mean dose rate using a variety of active and passive instrumentation. It can provide much useful information concerning crew exposure as functions of orbital altitude and inclination, spacecraft shielding and orientation and solar cycle phase. Considering the experimental protocol it is possible to compare different results from different groups done with different instruments. In the following tables (1.2.3 - 1.2.7) different results from US and Russian missions, namely Salyut orbital stations, Gemini, Apollo, Skylab, Apollo-Soyuz Test Project (ASTP) and Mir, obtained with TLDs are presented. Figure 1.2.7 shows the six permanent locations (DLOC) of area TLDs in the Space Shuttle. Their data is summarized in Figure 1.2.8 showing a graph of mean dose rates over the history of the STS program. Fig. 1.2.8 gives an overview of the detector positions inside Mir.

Orbital station	Transport spacecraft	Period and duration of mission	Cosmonaut	Absorbed dose rate (μGy/day)
Salyut-3	Soyuz 14	3–19 July 1974 16 days	Commander Engineer	165 ± 6 184 ± 11
Salyut-4	Soyuz 17	11 January–9 February 1975 30 days	Commander Engineer	257 ± 57 213 ± 27
Salyut-4	Soyuz 18	24 May–26 July 1975 63 days	Commander Engineer	484 ± 48 344 ± 30
Salyut-5	Soyuz 21	6 July–24 August 1976 49 days	Commander Engineer	169 ± 14 167 ± 6
Salyut-5	Soyuz 24	7–25 February 1977 18 days	Commander Engineer	193 ± 7 188 ± 5
Salyut-6	Soyuz-26	10 December 77–16 March 78 96 days	Commander Engineer	214 ± 10 224 ± 8
Salyut-6	Soyuz 29 & Soyuz 31	16 June–2 November 1978 140 days	Commander Engineer	225 ± 14 239 ± 14
Salyut-6	Soyuz 32 & Soyuz 34	25 February–19 August 1979 175 days	Commander Engineer	210 ± 11 210 ± 11
Salyut-6	Soyuz 35 & Soyuz 37	9 April–11 November 1980 185 days	Commander Engineer	146 ± 9 146 ± 9
Salyut-6	Soyuz T4	12 March–26 May 1981 75 days	Commander Engineer	147 ± 5 141 ± 5

Tab. 1.2.3 Crew dose rates measured using TLDs aboard the Salyut orbital stations [2].

Mission	Duration	Inclination	Apogee (km)	Perigee (km)	Absorbed dose (mGy)	Mean dose rate (μGy/day)
Gemini 4	97.3 h	32.5°	296	166	0.46	110
Gemini 6	25.3 h	28.9°	311	283	0.25	230
Apollo 7	260.1 h		227.8	283.4	1.60	150
Apollo 8	147 h		Lunar orbital flight		1.60	260
Apollo 9	241 h		190	192	2.00	200
Apollo 10	192 h		Lunar orbital flight		4.80	600
Apollo 11	194 h		Lunar flight		1.80	220
Apollo 12	244.5 h		Lunar flight		5.80	570
Apollo 13	142.9 h		Lunar orbital flight		2.40	400
Apollo 14	216 h		Lunar flight		11.40	1270
Apollo 15	295 h		Lunar flight		3.00	240
Apollo 16	265.8 h		Lunar flight		5.10	460
Apollo 17	301.8 h		Lunar flight		5.50	440
Skylab 2	28 days	50°		Mean alt = 435	15.96	570
Skylab 3	59 days	50°		Mean alt = 435	38.35	650
Skylab 4	90 days	50°		Mean alt = 435	77.40	860
ASTP	216 h	50°		Mean alt = 220	1.06	120

Tab. 1.2.4 Dose and mean dose rates measured using TLDs on early US space missions [2].
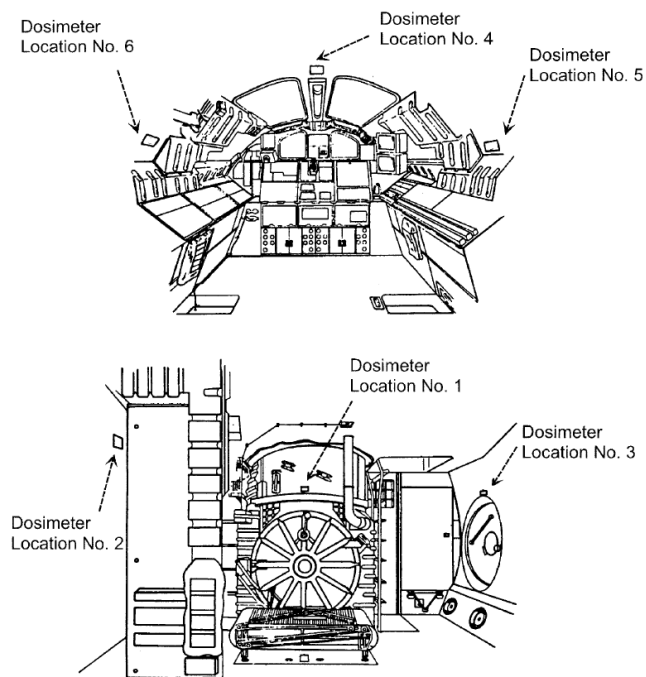
Fig. 1.2.7 The six permanent locations (DLOC) or area TLDs aboard the middeck of the Space Shuttle [2].
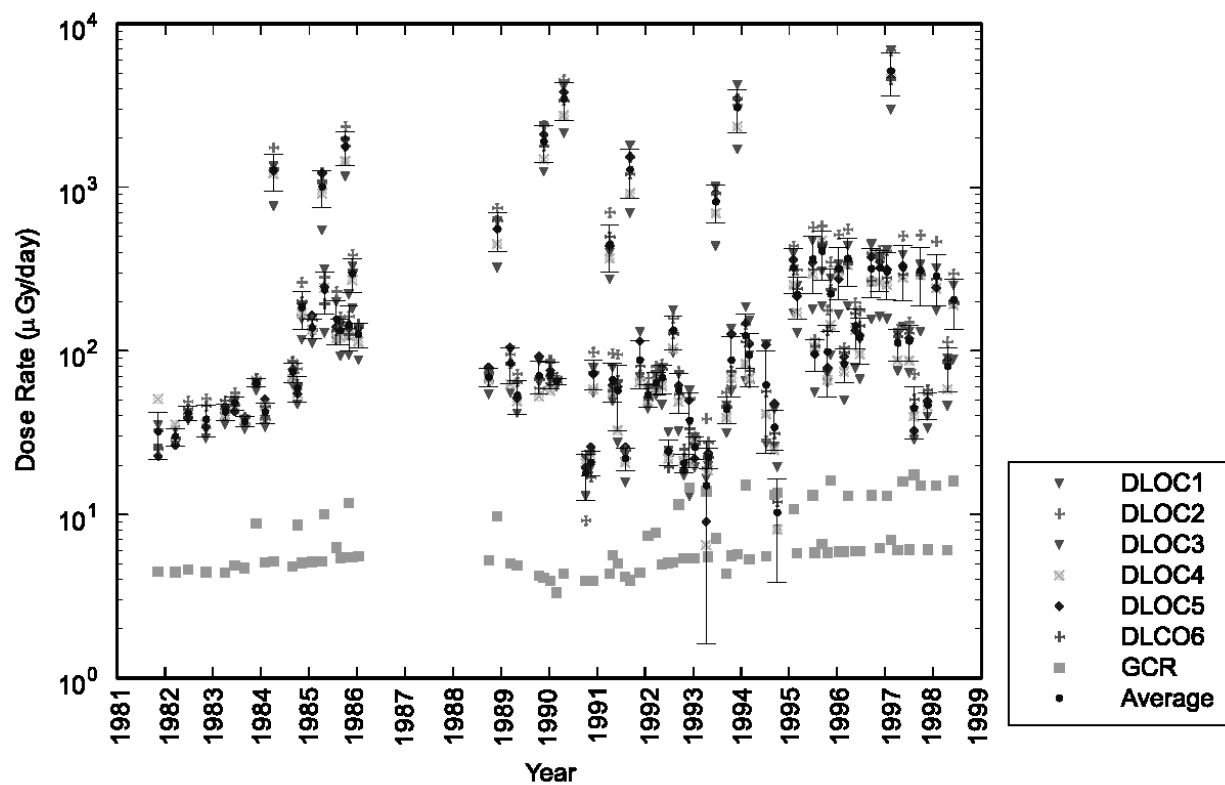

Fig. 1.2.7 Mean dose rates measured by TLDs at the six DLOC locations onboard the Space Shuttle over the history of the STS program [2].

Mission	Launch date	Duration (days)	Altitude (km)	Dose (cGy)	Dose rate (μGy/day)
Mir-01	3/13/86	123	–	2.24	182
Mir-02	2/6/87	217	–	4.67	215
Mir-03	12/26/87	366	–	5.95	162
Mir-04	11/26/88	152	–	2.99	197
Mir-05	9/6/89	225	403.8	6.75	404
Mir-06	2/11/90	179	396.7	3.24	181
Mir-07	8/1/90	131	397.7	2.6	198
Mir-08	12/2/90	176	390.2	4.4	250
Mir-09	5/18/90	145	398	5.44	375
Mir-10	10/2/91	175	402.2	5.05	289
Mir-11	3/17/92	146	405.8	3.97	272
Mir-12	7/27/92	190	414.5	6.85	360
Mir-13	1/26/93	180	405	8.54	474
Mir-14	7/1/93	197	403.7	8.91	452
Mir-15	1/8/94	183	405.6	9.29	508
Mir-16	7/1/94	126	410	–	–
Mir-17	10/4/94	169	406.6	–	–
Mir-18	3/14/95	115	393.7	3.39	295
Mir-20	9/3/95	179	393.9	–	–
Mir-21	2/21/96	195	389.8	6.62	339
Mir-22	8/17/96	198	382.3	7.5	379
Mir-23	2/10/97	187	386.8	6.15	329

Tab. 1.2.5 Mir crew dose and mean dose rates using TLDs [2].

Experiment/institution	Dates	Duration (days)	Dose (mGy)	Dose rate (μGy/day)
Mir-19/ISDA TLD-600	6/27/95–11/20/95	145	61.9 ± 1.4	427 ± 10
Mir-19/ISDA TLD-700	6/27/95–11/20/95	145	59.5 ± 1.1	410 ± 8
NASA-2/JSC	3/22/96–9/26/96	188.2	96.8 ± 0.9	514 ± 5
NASA-3/JSC	9/16/96–1/22/97	127.2	53.9 ± 0.7	421 ± 4

Tab. 1.2.6 Doses and mean dose rates measured in Mir commander's cabin, outer wall, shielding = 18.6 g/cm^2 [2].

Experiment/institution	Dates	Duration (days)	Dose (mGy)	Dose rate (μGy/day)
DosiMir 1/ISDA	5/91–10/91	145	34.8±1.2	240 ± 8
DosiMir 2/ISDA	10/91	8	1.6±0.2	201 ± 3
DosiMir 2/IMBP	10/91	8	1.7±0.1	218 ± 10
Mir 92/DLR	1992			205 ± 6
				208 ± 5
				229 ± 13
				294 ± 13
ADLET-1/ISDA	1/94–7/94	182	55.0±1.8	302 ± 10
ADLET-1/IMBP	1/94–7/94	182	59.2±4.9	325 ± 27
EuroMir 94/DLR	1994			380 ± 7
				322 ± 4
ADLET-2/ISDA	1/94–11/94	300	90.3±3.0	301 ± 10
ADLET-2/IMBP	1/94–11/94	300	83.4±5.1	278 ± 17
ADLET-3/ISDA	1/94–3/95	437	125.9±4.4	288 ± 10
ADLET-3/IMBP	1/94–3/95	437	130.7±9.2	299 ± 21
EuroMir 95/DLR	1995			483 ± 8
				371 ± 3
NASA-2/JSC	3/22/96–9/26/96	188.2	73.5±0.8	391 ± 4
Mir-19/ISDA TLD-600	6/27/95–11/20/95	145	65.6±2.9	452 ± 20
Mir-19/ISDA TLD-700	6/27/95–11/20/95	145	6408±4.7	447 ± 32
Pille 95/KFKI	1995			247 ± 10
Mir 97/DLR	1997			461 ± 4
				370 ± 3
NASA-3/JSC	9/16/96–1/22/97	127.2	43.6±0.7	341 ± 4
NASA-4/KFKI	1/12/97–5/22/97	130.1	57.1±5.3	439 ± 41
			59.1±5.6	454 ± 43

Tab. 1.2.7 Doses and mean dose rates measured in Mir engineer's cabin, outer wall, mean estimated shielding = 22 g/cm^2 and forward wall of engineer's cabin, mean shielding = 25.9 g/cm^2 [2].
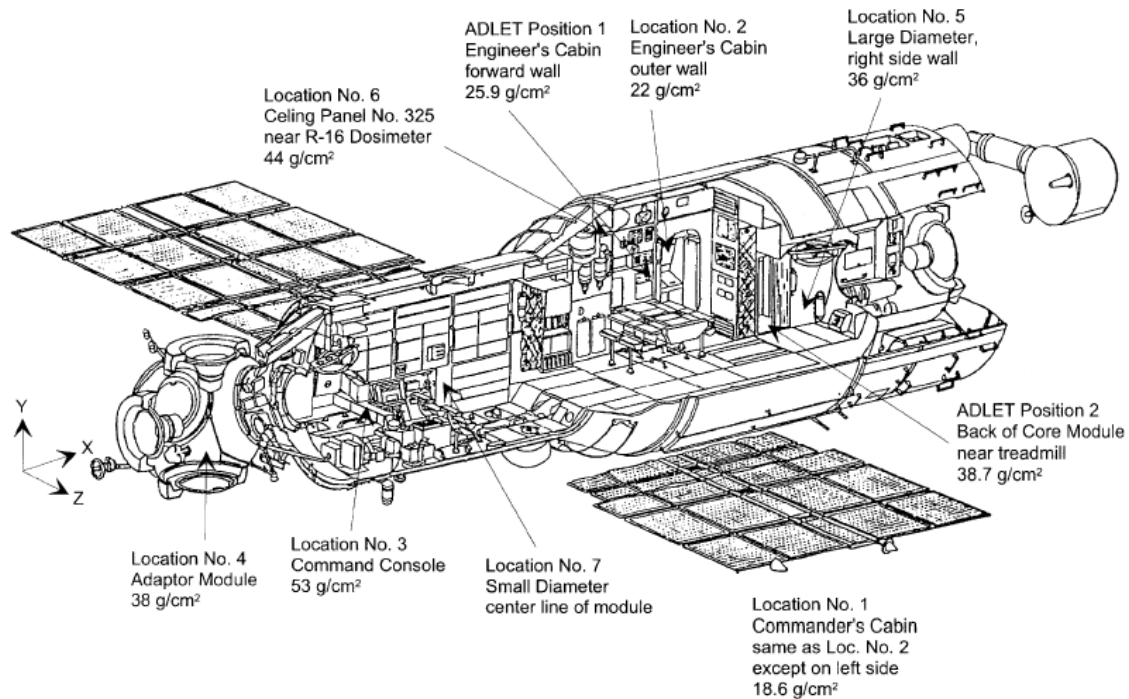
Fig. 1.2.8 Locations and shielding of passive detectors within the Base Block of the Mir Orbital Station [2].

Table 1.2.8 gives an overview of phantom experiments flown on the Space Shuttle program, MIR and the ISS. Doses measured with TLDs in a NASA phantom head can be seen as an example in fig. 1.2.9.

Experiment		Date	Location
Phantom Head	[1]	1989 - 1990	Space Shuttle
Spherical Phantom	[2]	1997 - 1999	Space Station MIR
Anthropomorphic Phantom	[3]	1998	Space Shuttle
Anthropomorphic Phantom	[4]	2001	International Space Station
Spherical Phantom MATROSHKA-R	[5]	2004 -	International Space Station
Anthropomorphic Phantom MATROSHKA	[6a] MTR-1 [6b] MTR-2A [6c] MTR-2B	2004 -	International Space Station

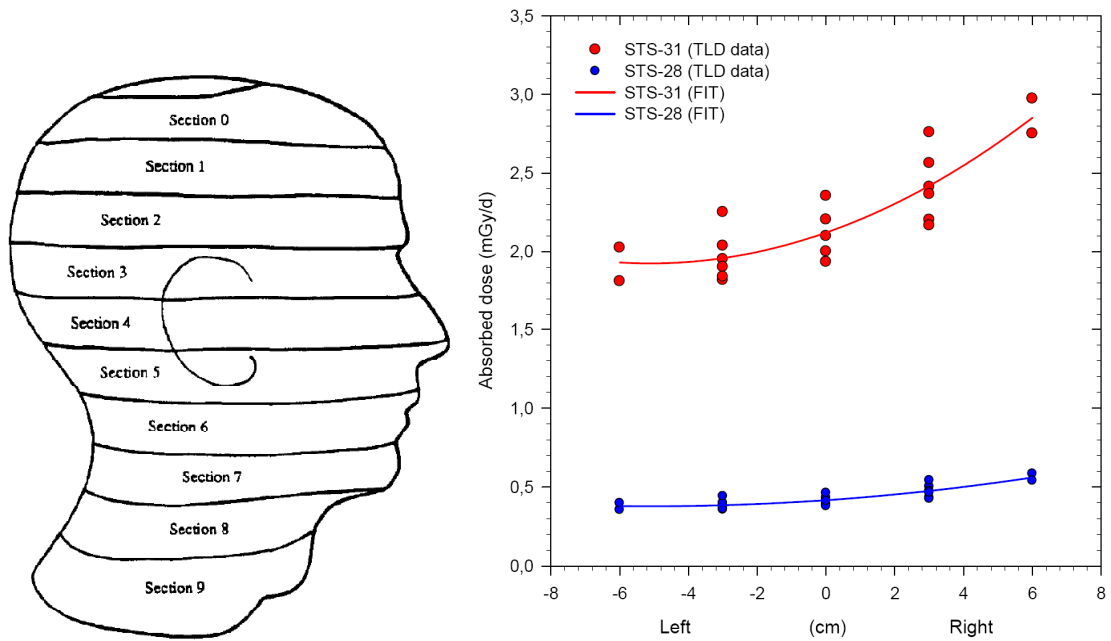**Tab. 1.2.8** Phantom experiments in space [28].

Fig. 1.2.9 Left: Lateral view of the phantom head (sections 1-8 contained TLDs). **Right:** Dose for the STS-31 mission (dominated by SAA) and the STS-28 mission (dominated by GCR) for Slice 3 as plotted as a function of position from the symmetry plane [28].

Onboard the ISS active and passive instrumentation is used for three purposes: area monitoring, personal monitoring and science driven experiments.

Passive instruments include: luminescence (optical, thermal) detectors, nuclear track detectors, combined instruments as well as super heated emulsion detectors [29].

Active instrumentation include: ion chamber-based proportional counters (NASA TEPC - tissue equivalent proportional counter, Russian R-16 - argon filled ionization chamber) [30].

The above presented data clearly indicates that radiation exposure in LEO is highly dependent upon the altitude, especially the altitude at which it traverses the SAA, and the solar cycle [2], [28]-[30].

1.3 RADIATION PROTECTION IN SPACE

Spaceflight unavoidably increases the exposure of astronauts to natural ionizing radiation. The absorbed doses encountered in LEO are roughly 100 fold higher than the natural background levels on the ground [5]. Radiation protection is the most outstanding challenge for missions in LEO and beyond. Therefore special consideration is needed to safeguard any human mission. Shielding is necessary to minimise the hazards to crews and payloads but as we have seen in section 1.1.2 this comes with further complications taking shape in the form of secondary particles and (secondary) electromagnetic radiation.

1.3.1 SPACECRAFT SHIELDING

Due to the manifold characteristics of the complex radiation environment in space shielding of payloads and crew is a most challenging task. Materials suited for construction of spacecraft due to their qualities as a light and robust building material such as aluminium may not be ideal for shielding purposes. Although most particle and electromagnetic radiation can be stopped or attenuated sufficiently with sufficient thickness of aluminium shielding (see Fig. 1.3.1 for electron and proton ranges in Al) it is not very effective for the protection against GCR – which are practically unstoppable- as can be seen in Fig. 1.3.2 and [7]. Following the elaborations in section 1.1.2 and having understood the physical processes in section 1.2 it is apparent that a single shielding material will never be sufficient for the task of the most reasonably achievable shielding.
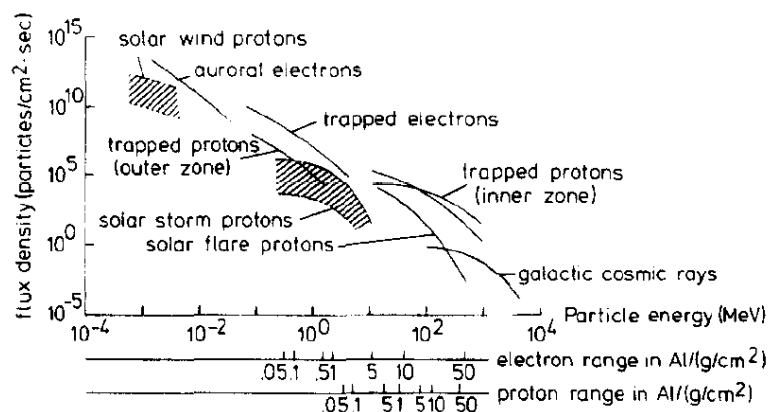

Fig. 1.3.1 Radiation environment in LEO with underlying ranges of electrons and protons in aluminium [7].
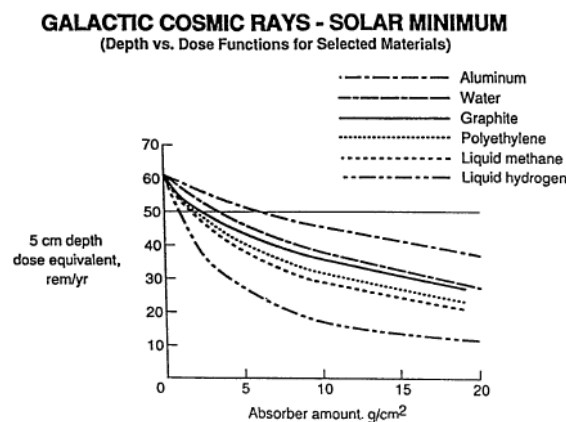

Fig. 1.3.2 Different shielding properties for selected materials for GCR exposure. Note that aluminium is the worst shielding material [8].

Due to their interaction properties shielding against GCR is best done with materials of low atomic number. Polyethylene is a good choice (abundance of hydrogen atoms) and with the same reasoning water supplies can be distributed so that they serve as life sustaining resource and as shielding.

A careful trade-off must be made in the use of shielding material, since an increase in weight affects construction and launch costs and subsequent mission accomplishment. A doubling of the presently used wall thickness (between 2 and 30 g cm^{-2} Al depending on type and placement of equipment) would decrease the dose by a factor of 1.2, but would increase both weight and cost by more than 30-50% [7].

Installation of an onboard 'storm shelter' represents another mean for reducing total body dose particularly in the event of large SPEs. This has been done for the ISS and it will be an integral part of any mission beyond LEO and in interplanetary space [7].

All these considerations apply to the concept of passive shielding measures. Research in the field of active shielding in the form of electrostatic, magnetic and plasma shields as well as chemical radioprotectants is underway since the 1960ies [9] but has not yet led to a major breakthrough. Technical difficulties in the installation of such systems for example the enormous amounts of energy needed for deflecting charged particles make them yet unavailable for spaceflight. Chemical radioprotectants have even been clinically tested [7] but have all proven to have unwanted side effects. Furthermore intravenous injection is necessary to get those chemical agents to work in an astronaut's body. This can not be seen as a desired and simple measure.

In summary it becomes clear that passive shielding is the most effective mean for radiation protection. Its implementation will be required for any type of human mission [7].

1.3.2 DOSE LIMITATION GUIDELINES FOR ASTRONAUTS

For implementing safety standards for occupational exposure to ionizing radiation the International Commission on Radiological Protection (ICRP) has set limits to safeguard individuals from the hazardous short-term and long-term effects of radiation. It has set its recommendations to no more than 20 mSv per year averaged over a 5 year period (max. 50 mSv in one year) effective dose, whole-body exposure. These precautions lead to a maximum excess lifetime risk of fatal cancer of between 3 and 4 percent under the currently agreed assumption of a nominal risk coefficient for an adult population of 4×10^{-2} / Sv and will prevent any short-term effects [2]. In the last decades it was possible to gain new insight into exposure levels in LEO due to increasing scientific data and improved experimental techniques and methods. Furthermore it is reasonable to consider radiation limits for space workers in relation to limits for workers on the ground. The NCRP findings [2] state that general workplace safety has increased significantly in highly developed countries in the past decades. Risk of accidental death in the general workforce does not exceed 3 percent and does not exceed 10 percent for dangerous occupations (i.e. activities in deep sea, test pilots etc.).

Taking this into consideration the National Council on Radiation Protection and Measurements (NCRP) has issued its recommendations for missions in LEO based on a 3 percent excess lifetime risk of fatal cancer [2].

Table 1.3.1 displays the recommended organ dose limits for deterministic effects for all ages for the bone marrow (=blood forming organs) the eye and the skin. Doses for deterministic effects are given in gray-equivalents (Gy-Eq) as to multiply organ doses in gray by the corresponding RBE [2].

	Bone Marrow (Gy-Eq)	Eye (Gy-Eq)	Skin (Gy-Eq)
Career	-	4.0	6.0
1 y	0.50	2.0	3.0
30 d	0.25	1.0	1.5

Tab. 1.3.1 Recommended organ dose limits for deterministic effects (all ages) [2].

Table 1.3.2 displays the effective dose ten-year career limits for certain age groups and gender.

	Effective Dose E (Sv)	
Age at Exposure (y)	Female	Male
25	0.4	0.7
35	0.6	1.0
45	0.9	1.5
55	1.7	3.0

Tab. 1.3.2 Ten-year career limits based on three percent excess lifetime risk of fatal cancer [2].

Hereditary effects have been thoroughly studied but remain insignificant for dose limit recommendations and such concerns continue to be an individual issue [2].

The underlying philosophy of these recommendations are not shared by all space authorities worldwide e.g. the Russian Federal Space Agency Roscosmos allows an annual limit of 500 mSv, and - in agreement with the Canadian Space Agency (CSA) - a career limit of 1 Sv, both independent of age and gender, since Russian studies yielded an increasing probability of non-cancer radiation effects with age that compensates the decreasing cancer risk [31].

1.3.3 THE INTERNATIONAL SPACE STATION

The International Space Station (ISS) is an internationally developed research facility that is being assembled in LEO. On-orbit construction of the station began in 1998 and is scheduled for completion by 2011. The station is expected to remain in operation until at least 2015, and likely 2020. With a greater mass (344,378 kg) than that of any previous space station, the ISS can be seen from the earth with the naked eye, and as of 2010 is the largest artificial satellite orbiting the earth. The ISS serves as a research laboratory that has a microgravity environment in which crews conduct experiments in biology, medicine, physics, astronomy and meteorology. The station has a unique environment for the testing of the spacecraft systems that will be required for missions to the Moon and Mars [10].

The ISS is operated by Expedition crews, and has been continuously staffed since November 2nd, 2000, meaning the ISS program has maintained an uninterrupted human presence in space for the past 12 years and 133 days (as of March 29th, 2011), which has surpassed the long standing record, set aboard the Russian space station *Mir*, of 9 years and 257 days [10]. The station is operated by six astronauts at a time. In March 2011 Expedition 27 is in progress [11].

The ISS is a synthesis of several space station projects that includes the American *Freedom*, the Soviet/Russian *Mir*-2, the European *Columbus* and the Japanese *Kibō*. Budget constraints led to the merger of these projects into a single multi-national program. The ISS project began in 1994 with the Shuttle-*Mir* program, and the first module of the station, *Zarya*, was launched in 1998 by Russia. Assembly continues, as pressurized modules, external trusses and other components are launched by American Space Shuttles, Russian Proton rockets and Russian Soyuz rockets. As of January 2010 the station consisted of 12 pressurized modules and an extensive integrated truss structure. Power is provided by 16 solar arrays mounted on the external truss, in addition to four smaller arrays on the Russian modules. The station is maintained at an orbit between 278 km (minimum) and 460 km (maximum) altitude and 51.56° inclination (thus making its orbit traverse the SAA), and travels at an average speed of 27,724 km/h , completing 15.7 orbits per day [10].

Fig. 1.3.3 The ISS from Space Shuttle Endeavour early 2010.

As the ISS constantly loses altitude because of a slight atmospheric drag, it needs to be boosted to a higher altitude several times each year. This boost can be performed by either the station's two main engines on the

Zvezda service module, a docked Space Shuttle, a Progress resupply vessel, or by ESA's Automated Transfer Vehicle (ATV). It takes approximately two orbits (three hours) for the boost to a higher altitude to be completed. Fig 1.3.4 shows the changing altitude over the first seven years of operation. One can clearly note the constant deorbiting after the Space Shuttle Columbia disaster (STS-107) on February 1st, 2003 after which NASA's Space Shuttle program came to a halt for 29 months.   STS-114 performed the next reboost in August 2005 lifting the ISS orbit to 357 km[12].
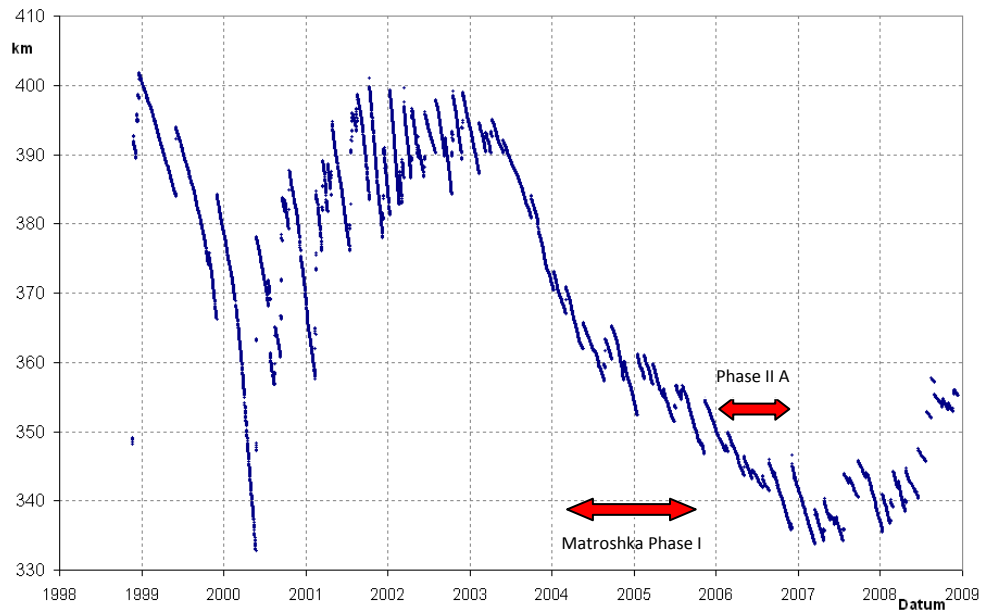

Fig. 1.3.4 Changing altitude of the ISS orbit plus Matroshka experiment phase I/ II A.

1.3.3.1 THE RUSSIAN PIRS MODULE

The 4.9 m long, 4,350 kg-pound Pirs (Russian: pier) Docking Compartment is attached to the bottom, earth-facing port of the Zvezda Service Module (see 1.3.3.2). It docked to the International Space Station on Sept. 16th, 2001, and was configured during three spacewalks by the Expedition Three crew. Pirs, also known as DC-1, launched Sept. 14th, 2001, as ISS Assembly Mission 4R on a Russian Soyuz rocket. The Docking Compartment has two primary functions. It serves as a docking port for the docking of transport and cargo vehicles to the Space Station and as an airlock for the performance of spacewalks by two Station crewmembers using Russian Orlan spacesuits. In addition, the Docking Compartment can transport fuel from the fuel tanks of a docked Progress resupply vehicle to either the Zvezda Service Module Integrated Propulsion System or the Zarya Functional Cargo Block. It can also transfer propellant from the Zvezda and Zarya to the propulsion system of docked vehicles -- Soyuz and Progress [13].
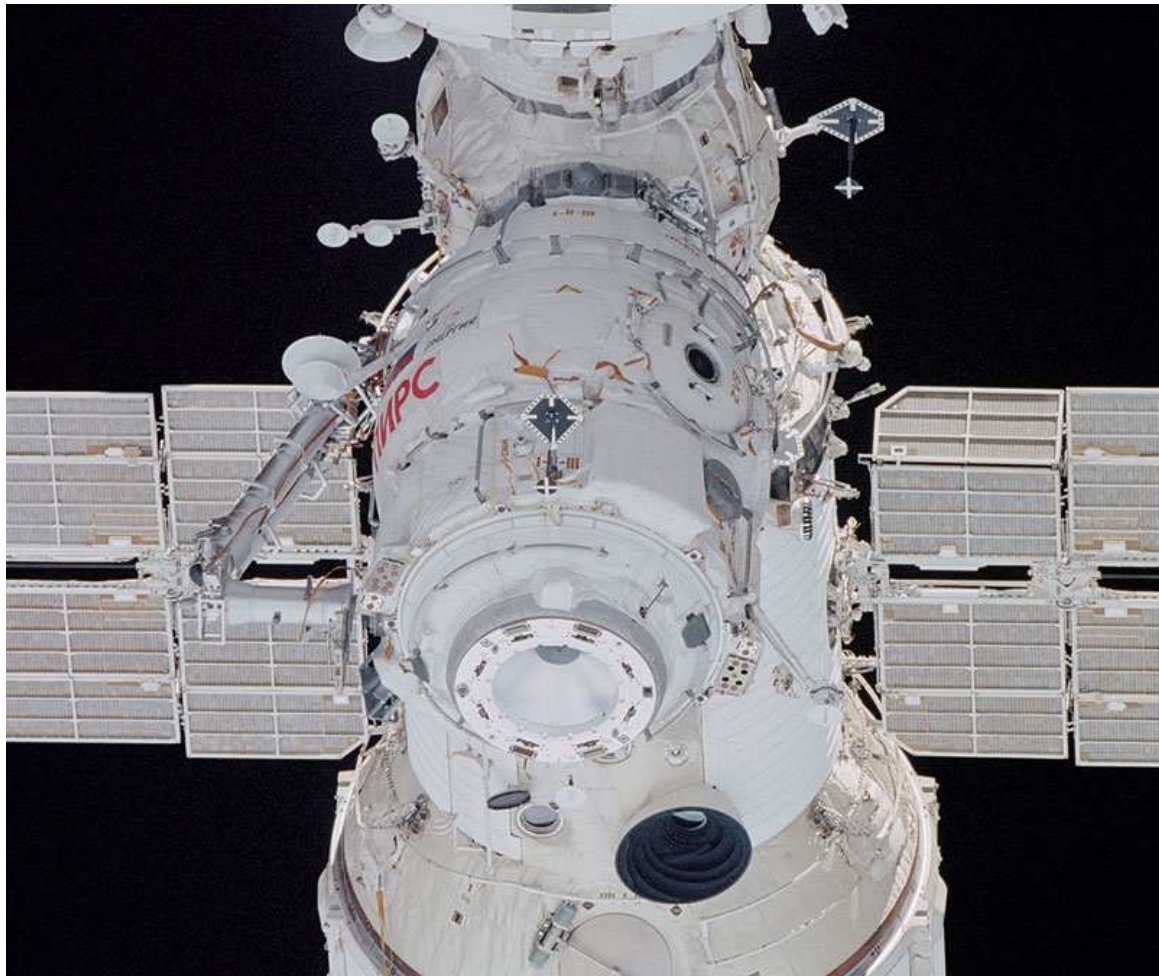

Fig. 1.3.5 The Russian Pirs Module as seen from STS-108.

The Matroshka Experiment Phase II A was set up in Pirs though initially a setup in the Zvezda module was planned. The results from Phase II A -which are the main focus of this work- shine light on the radiation hazards for on long term missions in LEO. A brief comparison to the exposure in the designated living quarters of the ISS (Matroshka Phase II B) hosted in the Zvezda module, which will be given at the end of section three, give insight to the varying conditions due to differences in the design of the spacecraft.

1.3.3.2 THE RUSSIAN ZVEZDA SERVICE MODULE

Zvezda (lit: Star) consists of a cylindrical "Work Compartment" where the crews work and live, a cylindrical "Transfer Chamber" which has one docking port, an unpressurized "Assembly Compartment" surrounding the Transfer Chamber, and a spherical "Transfer Compartment" with three docking ports. The component weights 18,051kg and had a length of 13.1 meters. The solar panels extend 29.7 meters. Its design was initially developed to serve as "Mir II" [13].

Zvezda provides the main living quarters for resident crews, environmental systems and attitude & orbit control. The module also provides docking locations for Russian Soyuz and Progress spacecraft and the European ATV, and its addition rendered the ISS permanently habitable for the first time [13].

Since Space Station Mir has represented the longest human presence in LEO, Russian engineering contributes essentially to the success of the ISS for its seasoned experience with long term human presence in space.

The Matroshka Experiment Phase II B was set up in Zvezda as to monitor radiation levels in the main living quarters of the ISS.

Fig. 1.3.6 The Russian Zvezda Service Module .

1.4 THE MATROSHKA EXPERIMENT

Matroshka is an ESA experiment unit for studies of the depth dose distribution of the different components of the radiation environment in LEO. It was designed to provide accurate information on the radiation doses in human organs during an extravehicular activity (EVA) as well as intravehicular activity (IVA). The objective of the Matroshka experiment is to determine the empirical relations between measurable absorbed doses and the tissue and organ absorbed doses in a realistic human phantom.

Considering the case of EVAs such measurements have the highest priority due to the fact that they make up a considerable amount of work schedule. Matroshka is the first external long term maintenance free payload ever installed on the ISS.

IVAs represent the greatest fraction of time for crew members spent in space and as we have seen in the previous sections the radiation field inside a spacecraft varies from that experienced in LEO [15].

The ultimate goal is to minimize hazards posed by radiation to crews and to be able to assess risks more accurately in the frame of space exploration.

Matroshka is the most significant international cooperation in space dosimetry ever conducted. Sixteen international research organizations (tab. 1.4.1), space agencies and universities participate in the science team with active and passive dosimetry systems.

Principal investigators	
Günther Reitz (ESA PI)	German Aerospace Center, Radiation Biology Division, Köln, Germany
Vladislaw Petrov (Russian PI)	Institute for Biomedical Problems, IMBP, Moscow, Russia
Co-investigators	
Rudolf Beaujean	Christian-Albrechts-Universität Kiel, Kiel, Germany
M. Luszik-Bhadra	Physikalisch-Technische Bundesanstalt, PTB, Braunschweig, Germany
V. Shurshakov, Y. Akatov	Institute for Biomedical Problems, IMBP, Moscow, Russia
P. Olko, P. Bilski	Institute for Nuclear Physics, INP, Krakow, Poland
J. Palfalvi	Nuclear Energy Research Institute, AERI, Budapest, Hungary
D. ÓSullivan	DIAS, Dublin, Ireland
D. Bartlett	National Radiological Protection Board, NRPB, Chilton, UK
N. Vana	Nuclear Institute of the Austrian Universities, ATI, Vienna, Austria
Y. Uchihori	NIRS, Chiba, Japan
S. Yoshitomi, A. Nagamatsu	JAXA, Japan
F. Cucinotta, M.Golightly	NASA JSC, Houston, TX, USA
B. Atwell	Space Systems Division, Boeing, Houston, TX, USA
E. Benton	Eril Research Inc., Richmond, CA , USA
S. McKeever	Oklahoma State University, Stillwater, OK, USA
J. Miller and C. Zeitlin	Lawrence Berkeley Laboratory, Berkeley, CA, USA

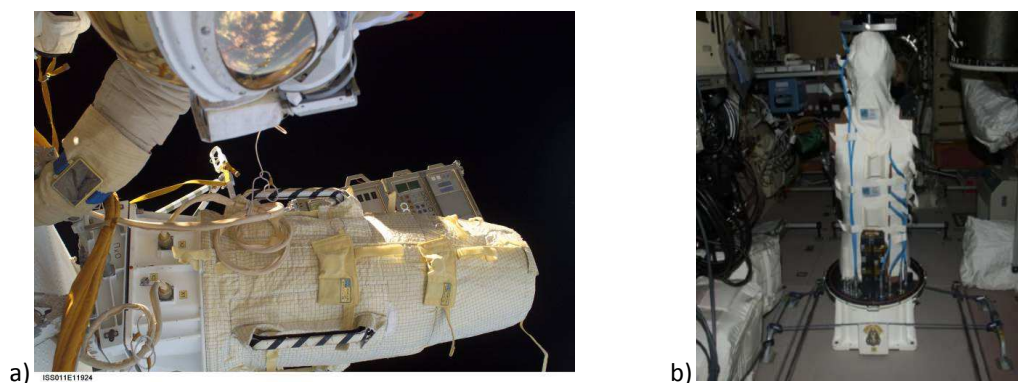**Tab. 1.4.1** Science team of Matroshka [15].

Fig. 1.4.1 The Matroshka phantom mounted a) outside and b) inside the ISS .

1.4.1 THE MATROSHKA FACILITY

The Matroshka facility basically consists of an Alderson-type human phantom torso attached to a base platform and covered by a protective carbon-fibre container, acting as a spacesuit model (Figure 1.4.1). The phantom consists of 33 nearly tissue-equivalent, polyurethane-based slices of specific density for tissue and organs, aligned along a mandrel (fig. 1.4.2). Natural bones are embedded. It weighs 68 kg and has a height of 1100 mm. 356 channels and cut-outs enable accommodation of 7 active and more than 4800 passive radiation sensors. Active devices included different types of silicon scintillation detectors, a dosimetry telescope and a tissue-equivalent proportional counter. Passive detectors comprise of thermo-luminescence (TLDs) and optically stimulated luminescence dosemeters as well as plastic nuclear track detector sheets. Additional detectors were implemented in 5 boxes at the sites of radiosensitive organs (eye, lung, stomach, kidney and intestine). A sixth box was mounted on top of the head. To simulate the skin, the phantom was dressed by a hood (figure 1.4.3) and a poncho (fig 1.4.4) including polyethylene stripes with sewed in TLDs. Skin doses were also measured on the anterior, posterior and lateral sides of the torso with the detectors housed in polyethylene boxes sued to the phantom surface (mid thorax, upper abdomen, lateral right and left sides, mid dorsal and lumbar). For outside exposure it was coated with a protective multilayer insulation (MLI) to which detector boxes had been attached (fig. 1.4.5) [15].
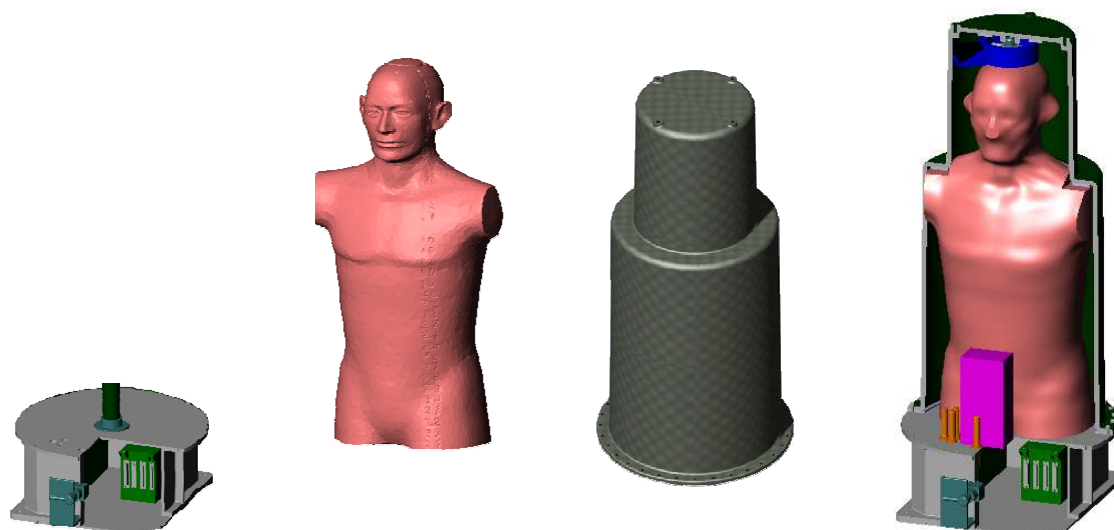

Fig. 1.4.1 Schematic drawing illustrating the design of the Matroshka facility.
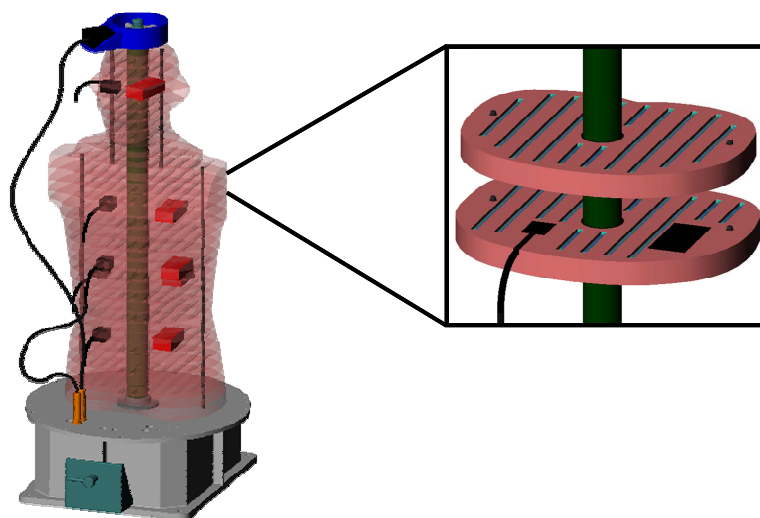

Fig. 1.4.2 The Matroshka torso is cut into 33 slices for dosemeter integration.
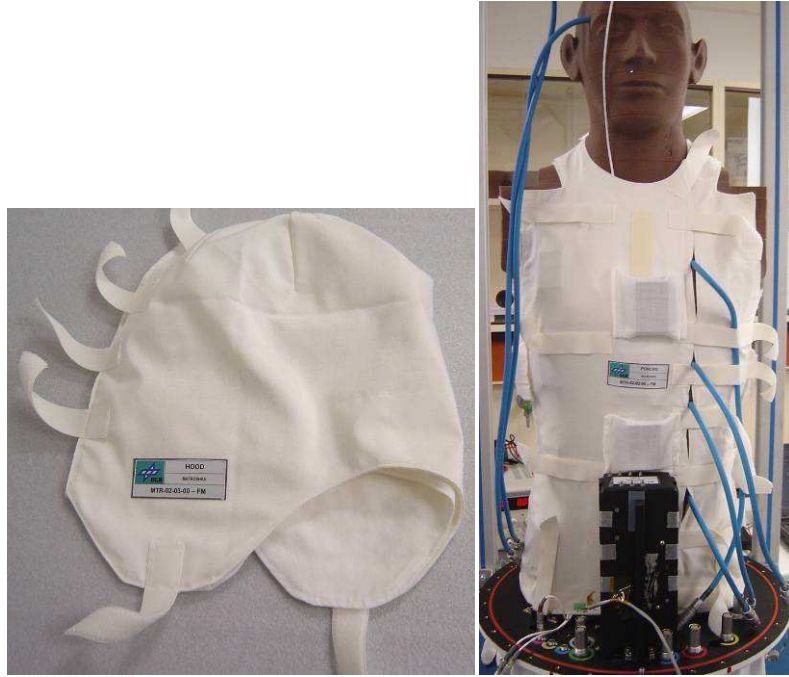
Fig. 1.4.3 The phantom wears a hood to simulate the skin.

Fig. 1.4.4 from left to right: the phantom torso divided into 33 slices, the hood, the containment and the MLI.

Fig. 1.4.4 shows ground pictures taken from the different stages of assembling Matroshka.

The TLDs (3.2 x 3.2 x 0.89 mm chips, section 2.3) mounted in the 356 channels are organised in polyethylene tubes. To identify them properly they are labeled with a code composed of the slice number and the lateral position of the tube within the slice (fig. 1.4.5). For the detection of the neutron component (see section 2.7) two TLDs – TLD-600 /TLD-700 (see section 2.3) – were stacked at one position.

Fig. 1.4.5 a) The channels hosting the TLD tubes [15] **b)** labelling system of individual tubes.

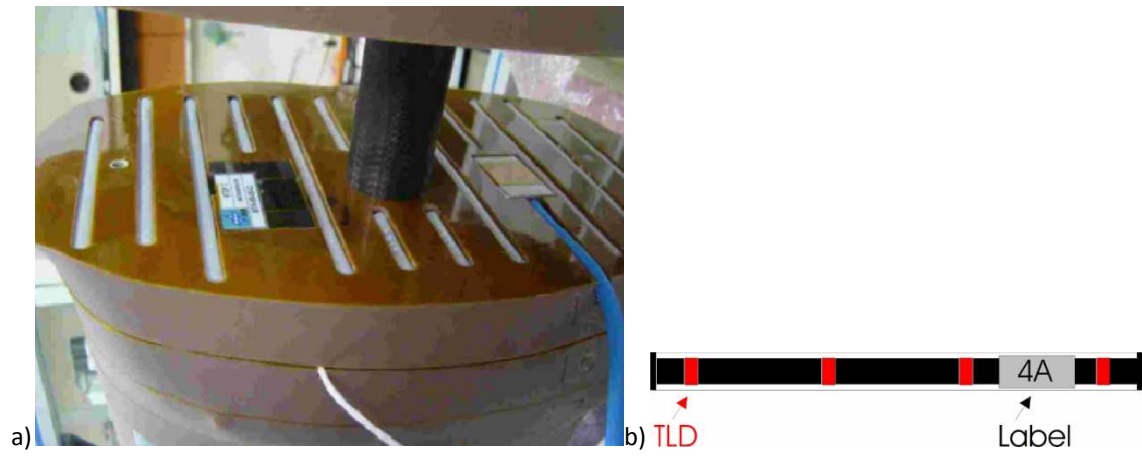## 1.4.2 PHASE I - OUTSIDE EXPOSURE

The Institute of Atomic and Subatomic Physics provided 942 thermoluminescence dosemeter (TLD) chips for insertion into 89 detector tubes in 14 different slices of the Matroshka phantom torso. A few more hundred TLD chips and single crystals were used for dose measurements in the organ and poncho detector boxes as well as the MLI and the sued in stripes. A total number of slightly more than 1100 detectors from ATI accounted for about one fifth of the passive radiation detector set used in the Matroshka experiment. A detailed illustration of the dosemeter distribution within the 14 relevant slices can be found in Appendix A. In the Figures, the detector chips of the participating laboratories are represented by different colours, with dark blue referring to dosemeters from ATI.

The Matroshka experiment was launched to the ISS from the Kazakh Cosmodrome Baikonur on January 29 2004, 12:58 CET on board an unmanned Russian Progress M1-11 freighter (mission 13P) carried by a Soyuz-U rocket. The cargo ship docked to the Zvezda Service Module aft port two days later at 12:13 CET. The entire process of fully automated rendezvous, closure, final approach and capture, followed by closing of hooks and latches, went smoothly and without issues. During a 3-hour 55-minute EVA in the night of February 26/27 2004 Expedition 8 crew members—Commander C. Michael Foale (EV1) and Flight Engineer Alexander Y. Kaleri (EV2)—attached the phantom torso to the outer hull of the Zvezda Module. This was the 52nd spacewalk devoted to Space Station assembly, operations and maintenance, and the first two-person spacewalk at the ISS. Matroshka was removed and brought back inside the Station during an EVA in the night of August 18/19 2005. Total time for this spacewalk performed by the Expedition 11 crew—Commander Sergei K. Krikalev (EV1) and Flight Engineer John L. Phillips (EV2)—was 4 hours and 58 minutes. Remarkably enough, it was the eighth spacewalk for Krikalev who also set the time-in-space record by completing six spaceflights, logging to a total of 803 days, 9 hours and 39 minutes in space. After disintegration on board the Zevzda Module, the passive detectors were downloaded to earth together with the Expedition 11 crew and space tourist Gregory Olsen. The Soyuz TMA-6 spacecraft carrying crew and payload undocked from the Zarya Module nadir port on October 10 2005 at 22:49 CET and landed on the following day at 02:09 CET 58 km northeast of the Kazakh town of Arkalyk. Table 1.4.2 gives the timetable for Matroshka Phase I [22].

Date	Event	Crew	Expedition
Jan. 29 2004	Launch of Matroshka with Progress 13P freighter		ISS-8
Jan. 31 2004	Docking of Progress 13P cargo ship to ISS		
Feb. 26 2004	EVA to attach Matroshka to the Zvezda outer hull	C. M. Foale, A. Y. Kaleri	
Aug. 18 2005	EVA to retrieve Matroshka into ISS	S. K. Krikalev, J. L. Phillips	ISS-11
Oct. 10 2005	Undocking of Soyuz TMA-6 from ISS		
Oct. 11 2005	Return of Soyuz TMA-6 with passive radiation sensors		

Tab. 1.4.2 Timetable of Matroshka Phase I [22].

Figure 1.4.6 shows the phantom mounted on the Russian Zvezda Service Module.

Results of phase I are depicted in figures 1.4.7 and table 1.4.3 [15]. It becomes clear that the skin receives the highest dose with a steep decline up to a factor of 20 to the deep organs. This decrease due to body self-shielding and a concomitant increase in radiation quality factor of 1.7 shows the complexity of the issue [15]. It has to be noted that no massive SPE occurred during exposure which would have lead to different results. The complex interplay of the space radiation environment with the spacecraft structure –albedo for example - and ultimately the astronaut's personal 'shielding' – the space suit and his own body gives us the notion that

radiation transport codes and sufficiently accurate knowledge of the radiation field in LEO as well as the mass distribution surrounding an astronaut cannot be overestimated [15].
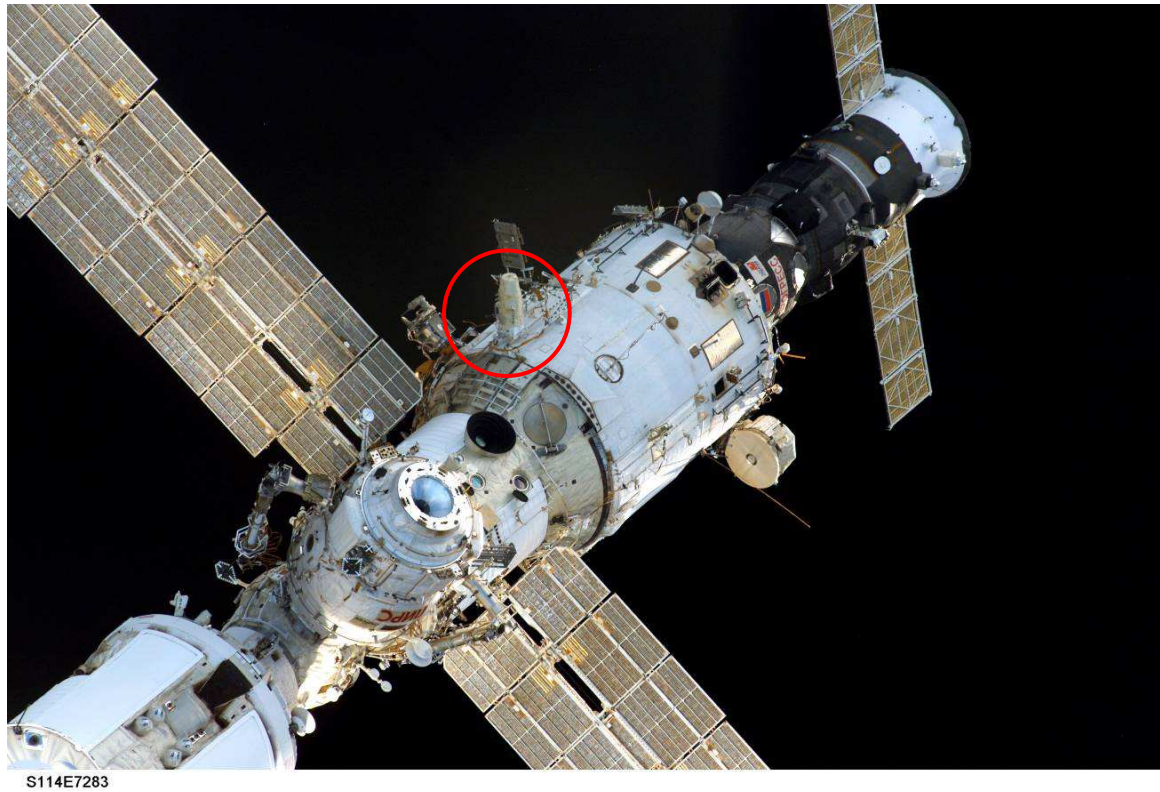

Fig. 1.4.6 The phantom mounted on the Russian Zvezda Service Module.
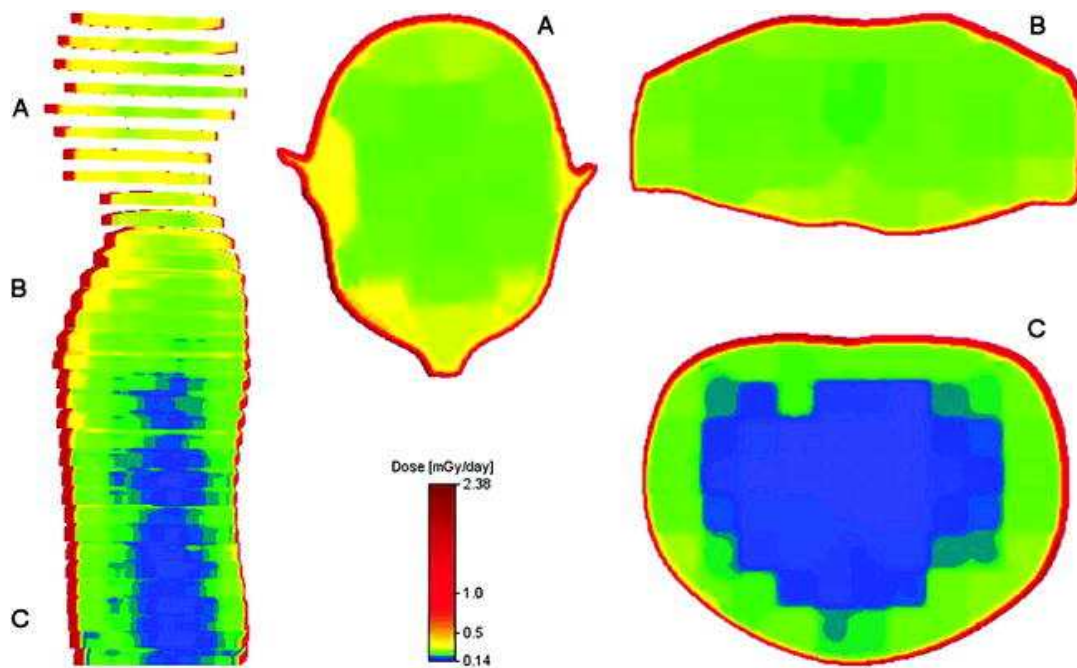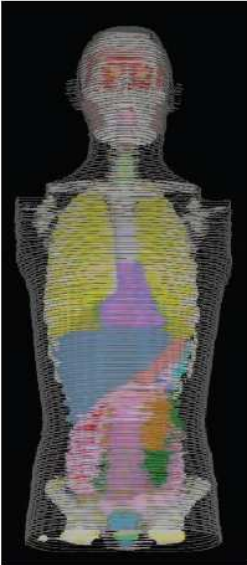
Fig. 1.4.7 Median-sagittal plane of the 3D model of the phantom including 'skin dose' distribution. 2D dose distribution for the head (A), the shoulder region (B), and the lower torso (C) [16].

Organ	Dose rate (mGy/day)
Skin	0.94 (8)
Eyeball, lens	0.54 (8), 0.58 (12)
Salivary glands, breast	0.33 (7), 0.39 (10)
Thymus, thyroid, trachea, brain	0.28–0.30 (6)
Lungs, bones	0.26 (6), 0.28 (6)
Esophagus, testes	0.24 (6), 0.26 (7)
Colon, stomach, liver, red bone marrow, heart	0.22–0.24 (6)
Kidneys, gall bladder, small intestine, spleen, pancreas, prostate	0.20–0.22 (6)

Note. Inset shows the organs of the Zubal phantom mapped and scaled into the voxel representation of MA-TROSHKA obtained from the CT slices. Values in parentheses specify measurement precision in percent.

Tab. 1.4.3 Organ dose rates calculated from TLD depth-dose distribution [16].

1.4.3 PHASE II A/B - INSIDE EXPOSURE

The detector upload for the Matroshka-II phase A experiment was launched to the ISS from the Kazakh Cosmodrome Baikonur on December 21, 2005, 19:38 CET on board an unmanned Russian Progress M-55 freighter (mission 20P) carried by a Soyuz-U rocket. The cargo ship docked to the station's Pirs Docking Compartment two days later at 20:46 CET. The entire process of fully automated rendezvous, closure, final approach and capture, followed by closing of hooks and latches, went smoothly and without issues. The integration of the passive detectors on board the Russian Zarya module were performed by Flight Engineer One Valery Tokarev and Commander William McArthur from 09:30 to 13:30 CET on January 5, 2006 during ISS expedition 12. Disintegration of the passive detectors took place on December 7, 2006 carried out by Flight Engineer Two Thomas Reiter from 22:20 to 23:20 CET during ISS expedition 14. They were downloaded to Earth onboard STS-116 on December 22, 2006. The Space Shuttle arrived safely at the Kennedy Space Center at 10:32. Tab. 1.4.4 gives the timetable. Fig. 1.4.8 and 1.4.9 show the phantom inside Zarya. The detailed results of Matroshka-II Phase A will be given in sections 3.1. -3.7.

Date	Event	Crew	Expedition
Dec. 21 2005	New detector upload – Start of Matroshka-II Phase A – with Progress 20P freighter		
Dec. 23 2005	Docking of Progress 20P cargo ship to ISS		ISS-12
Jan. 05 2006	Integration of the passive detector sets	W. McArthur, V. Tokarev	
Dec. 07 2006	Disintegration of the passive detector sets	T. Reiter	
Dec. 19 2006	Undocking of STS -116 from ISS		ISS-14
Dec. 22 2006	Return of STS-116 with passive detectors		

Tab. 1.4.4 Timetable of Matroshka-II Phase A [21].

Setup of TLDs was identical with the exception for LiF: Mg,Cu,P (TLD 700-H) which were not used. 996 TLDs from ATI type TLD-300, TLD-600 and TLD-700 were employed (see section 2.3 for details). Active detectors were not used since they did not pass the required acceptance test in time and use was therefore not cleared. These active instruments were used in Matroshka-II Phase B (hosted in Zvezda). It has to be noted that no major SPE occurred during that period (fig. 1.4.9).

While this thesis was written data from Phase II B became available. A short discussion is given in 3.7.
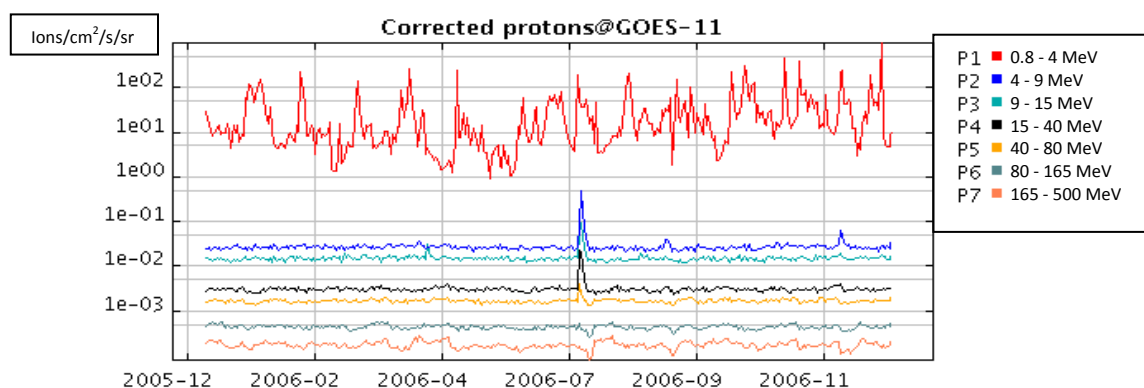

Fig. 1.4.9 Proton Flux during exposure period [source: SEC/NOAA 2007].

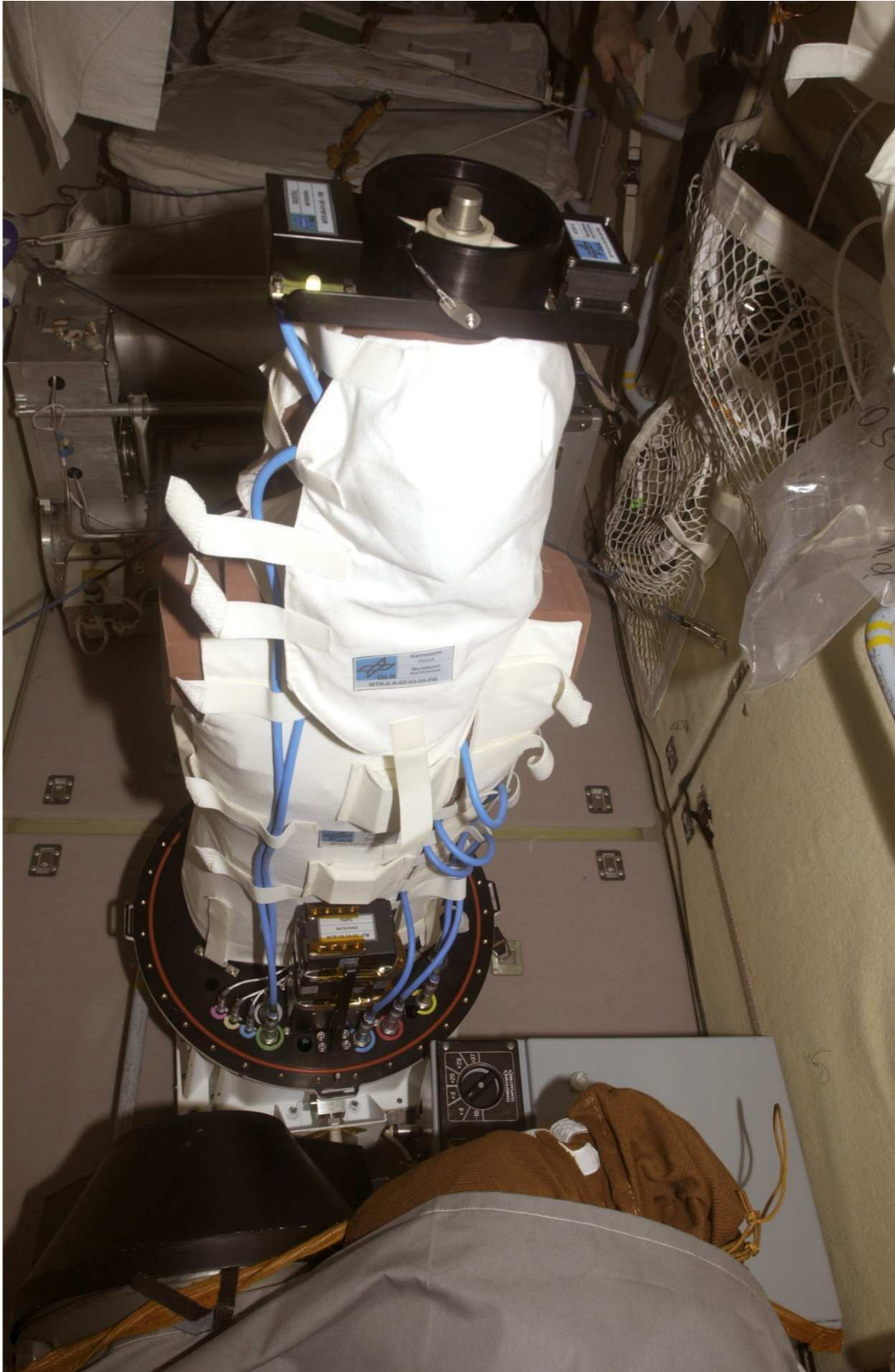**Fig. 1.4.9** Flight Engineer One Valery Tokarev handling Matroshka.

Fig. 1.4.10 Matroshka with Poncho attached.

2. INSTRUMENTATION AND METHODS

2.1 THERMOLUMINESCENCE

Thermoluminescence (TL) is a luminescence phenomenon of an insulator (or semiconductor) which can be observed when the solid is thermally stimulated. This should not be confused with thermal or black body radiation, which occurs in any material at any temperature. TL is the thermally stimulated emission of light following the previous absorption of energy from radiation. This leads to three fundamental characteristics as the basis for any TL emission. Firstly, the material needs to be an insulator or semiconductor for metals do not show luminescent properties. Secondly, the material must have absorbed some form of ionizing radiation at some point in time and thirdly heating must be applied in order to trigger TL emission [18]. Importantly, TL radiation follows a thermal stimulation after the material has been excited by means of ionizing radiation. This means that TL materials store the 'information' of radiation until it gets released. A second triggering is not possible but reuse after a new excitation is possible - keeping in mind certain steps that have to be taken to establish reproducibility. Such steps take the form of determined annealing procedures which we will discuss in this section. The storage capacity of TL materials makes them best suited for dosimetric applications. Since this is an intrinsic solid state matter feature TL materials serve as passive instruments to record radiation [19].

The underlying principle of TL is found in the energy band theory of solids. In an ideal crystalline semiconductor or insulator electrons reside in the valence band in the ground state. The next possible band an electron can occupy is the conduction band, separated from the valence band by the so-called forbidden region. The energy difference between the allowed bands is E_g. In the case of crystal defects or impurities within the lattice, however, there exists the possibility for electrons to have energies in the forbidden region. In a simple TL model two such levels are assumed, one below the conduction band and one above the valence band (fig. 2.1.1). The highest level indicated by T is above the equilibrium Fermi level (E_f) and empty before the exposure to radiation which creates electrons and consequently holes. It is therefore a potential electron trap. The other level (R) is a potential hole trap and is able to serve as a recombination centre. The absorption of energy above E_g results in ionization of valence electrons, producing an electron-hole pair that will either be trapped or recombine if they are free charge carriers. In semiconductors a certain fraction is trapped: the electrons at T and the holes at R. The probability p per unit time of release of an electron from the trap is described by the Arrhenius equation.

$$p = s \exp\left(-\frac{E}{kT}\right)$$

k...Boltzmann constant, =8.617 10^{-5} eV/K

T...absolute temperature (K)

The term s is called the frequency factor or attempt –to-escape factor. In a simple model s is a constant and not dependent on temperature. E is called the trap depth or activation energy, i.e. the energy needed to release the electron into the conduction band. The relaxation rate to equilibrium - i.e. all traps are emptied and no holes are left - determined from the Arrhenius equation is low. That means the metastable condition of trapped electrons and holes exist infinitely unless the temperature is raised above the initial temperature at irradiation (T_0). So 'information' about radiation can be stored infinitely in theory. In reality fading mechanisms have to be taken into consideration as we will see in the next section.

Raising the temperature above T_0 increases the probability for detrapping and thus recombination. Again in a simple model, the recombination centre is a luminescent centre that gets excited and relaxes to its ground state by emitting a light quanta i.e. thermoluminescence. The intensity of the TL signal will be determined by the number of excited luminescent centres per time [18].
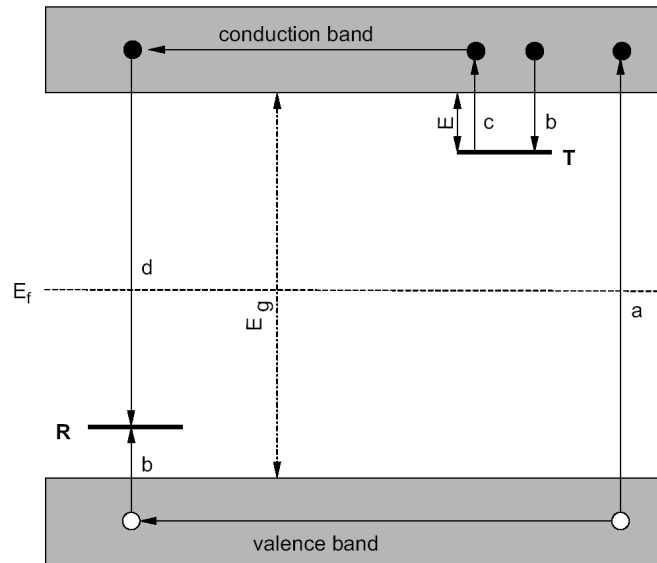
Fig. 2.2.1 Energy band model showing the electronic transitions in a TL material according to a simple two-level model: (a) generation of electrons and holes; (b) electron and hole trapping; (c) electron release due to thermal stimulation; (d) recombination. Solid circles are electrons, open circles are holes. Level T is an electron trap, level R is a recombination centre /luminescent centre, E_f is the Fermi level, E_g is the energy band gap i.e. the depth of the trap [18].

2.2 APPLICATION TO DOSIMETRY

Due to its long-term storage capacity TL materials seem well suited for dosimetric purposes. TLDs are small in dimension and weight, easy to handle and do not need any form of external energy to operate them. These qualities make them widely used for monitoring radiation levels of occupationally exposed workers on the ground as well as in space. A predominantly desired property of a TLD, however, is a linear relationship between TL intensity and dose. This is unfortunately not the case as many if not most TL materials show dose ranges of linear, sublinear and supralinear dose response (fig. 2.2.1). In the case of sublinearity saturation effects are observed, i.e. all traps full of appreciable radiation damage. Careful calibrations and corrections are therefore required. Supralinearity and saturation can both be affected by previous exposure and by thermal treatments. So re-use of a dosemeter may present problems. The TLD may exhibit a different dose response. Additionally the three response regions can get shifted by different LET values. To be able to use a TLD repeatedly annealing procedures have to be defined in order to 'reset' the original properties of the TLD.
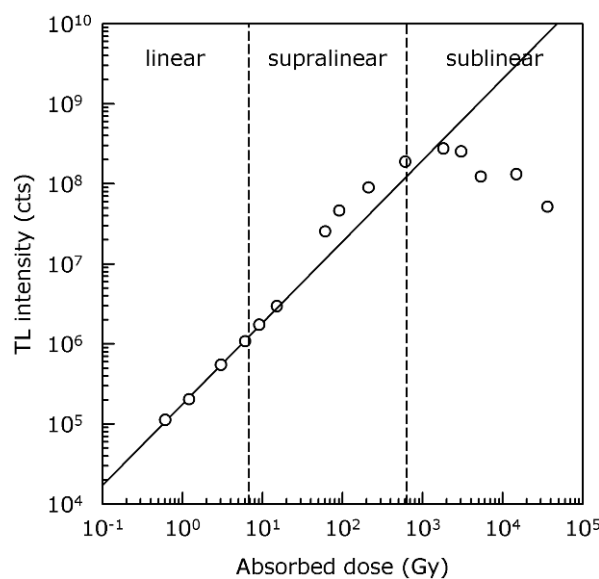

Fig. 2.2.1 Dose response for LiF:Mg,Ti detectors measured after exposure to a [90]Sr–[90]Y beta source [21].

A further demand made upon a TLD is that its response is independent of dose rate. Several detector materials have been tested with high dose rates using X-ray pulses. Dose rate independent responses have been found between 5 Gy/s and $1.5 \cdot 10^8$ Gy/s. At very high doses (> 500Gy at > $1.5 \cdot 10^8$ Gy/s) loss of sensitivity is observed. Dose rate dependence has not been identified as a problem to TLDs [19].

Fading and stability of signals are important concerns in the choice of a TLD material. If the energy trap depth E is small fading will occur both during irradiation and between irradiation and readout. That is why temperature ranges around 200-250 °C are used to guarantee stable signals. Temper-cycles are used to eliminate less stable peaks and to improve the reproducibility and reliability of results.

The typical readout of a TLD is a curve of TL intensity over temperature. This is called a glow curve (fig.2.2.2). Several peaks occur that can be used for dosimetric purposes. Basically the TLD is thermally heated at a specific well defined heating rate and its signal is amplified by a photo multiplier and the converted electronic signal corresponds to a count rate. Calibration with a well defined dose makes it possible to define a **calibration factor** [**counts/mGy**] to determine the measured dose. Peak counts are used for that purpose.
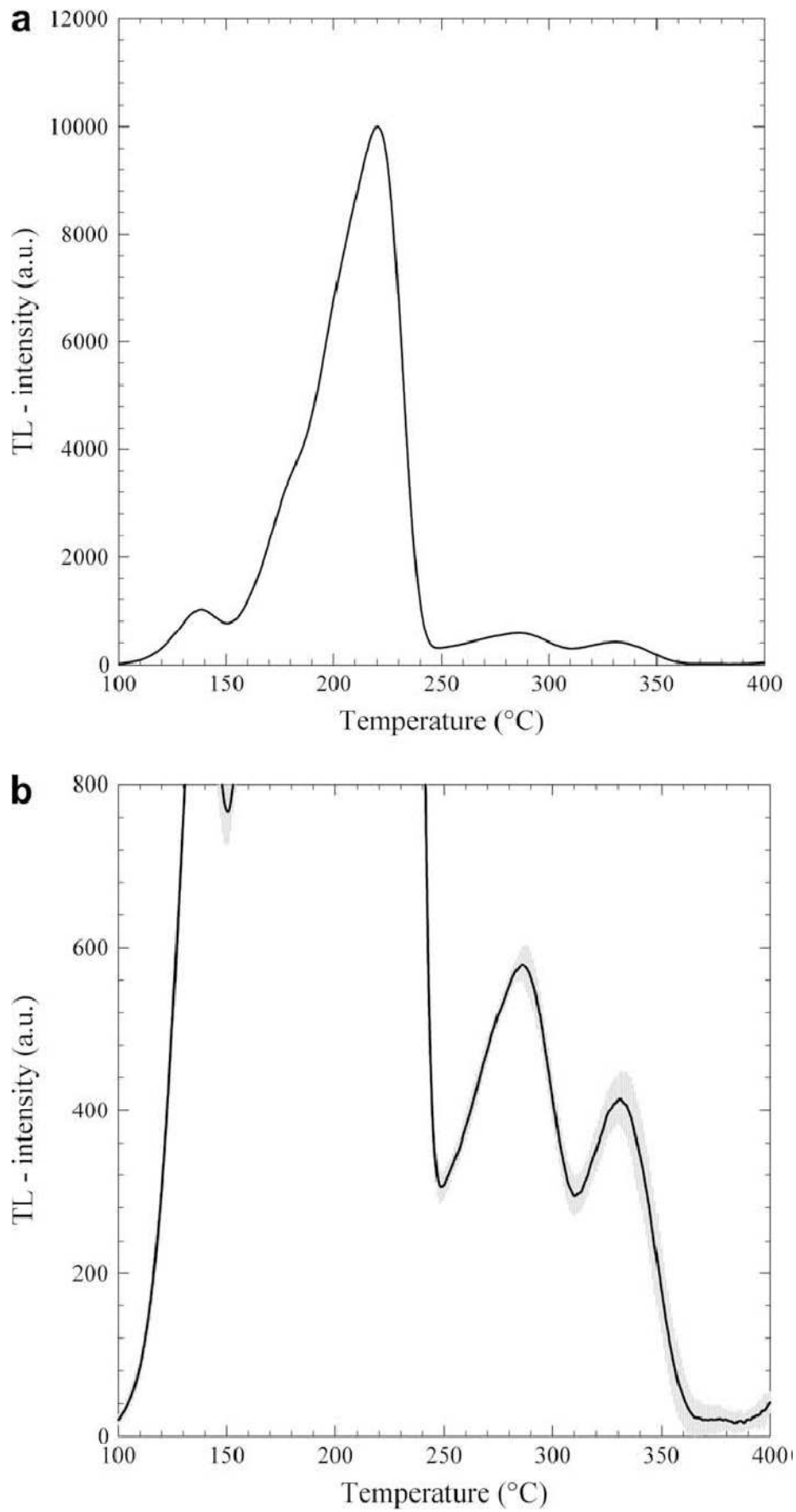
Fig. 2.2.2 A typical TL glow curve a) entire temperature range b) enlarged high-temperature structure [23].

TLD preparation and analysis procedures used for Matroshka II Phase A:

Annealing:

To prepare TLDs for exposure an annealing protocol was applied. It consisted of heating to 400°C for   1 hour for TLD-600 and TLD-700 and for 1.5 hours for TLD-300 in air in a Heraeus KM 170 (Heraeus Instruments GmbH, Hanau, Germany) oven and exponential cooling over a period of ~24 hours to room temperature.

Readout:

TLDs were pre-annealed at 120°C for 30 min and taken out at 42°C. Heating/passive-cooling control was software-guided and went according to a predefined protocol that had been developed internally.

The glow curves were readout by contact heating on a Nikrothal 80 austentitic alloy planchet from room temperature to a maximum temperature of 480°C (TLD-600, TLD-700) or 400°C (TLD-300) at a linear heating rate of 5°C/s. To minimize spurious chemoluminescence and triboluminescence the measurement chamber was first evacuated to ~2.7 Pa and flooded with ultra-pure (5.0) dry N_2 gas during readout. The reader TL-DAT. II (developed at the ATI [20]) employed the photon counting technique using a Thorn EMI 9635 QB photomultiplier (Thorn EMMI Gencom Inc., Fairfield, NJ, USA) with a bialkali photocathode [23]. In order to attenuate the light incident on the photomultiplier tube, a neutral optical filter (NG3, Schott AG, Mainz, Germany) was used for TLD-300 and an infrared filter was used for TLD-600 and TLD-700 to decrease the high temperature black body radiation. After readout the chamber had to cool down to at least 60°C in order to remove the TLD chip.

Analysis:

For the analysis the corresponding main dosimetry peaks – peak 5 for TLD-600 and TLD-700, peak 3 for TLD-300 – were electronically correlated at 220°C (peak 5) and 164°C (peak 3). For all glow curves an exponential fit was applied to subtract black body radiation and an offset from 20-80°C was used to eliminate electronic noise [23]. Glow curves were smoothed by 21 points and peak 5 / peak 3 counts were identified.

For TLD-300 peak 3 shows observable fading even for room temperature, therefore peak 5 counts were used.

2.3 THERMOLUMINESCENT PHOSPHORS

2.3.1 ^{6}LiF:Mg,Ti (TLD-600)

Composition	^{6}LiF – 95.62% , ^{7}LiF – 4.38%
Chip dimensions	3.2 x 3.2 x 0.89 mm
Dosimetric glow peak	220°C (peak 5)
Annealing	400°, 1 hour
Commercial source	Thermo Fisher Scientific, Inc.

Thermal neutron irradiation of ^{6}LiF produces a triton and an alpha particle by the reaction ^{6}Li(n,α)^{3}H. Thus TLD-600 exhibits a sensitive thermal neutron response. An almost tissue equivalent behaviour can be seen for photons.

2.3.2 ^{7}LiF:Mg,Ti (TLD-700)

Composition	^{6}LiF – 0.001% , ^{7}LiF – 99.999%
Chip dimensions	3.2 x 3.2 x 0.89 mm
Dosimetric glow peak	220°C (peak 5)
Annealing	400°, 1 hour
Commercial source	Thermo Fisher Scientific, Inc.

There is virtually no neutron sensitivity. An almost tissue equivalent behaviour can be seen for photons.

2.3.3 CaF$_2$:Tm (TLD-300)

Composition	CaF$_2$
Chip dimensions	3.2 x 3.2 x 0.89 mm
Dosimetric glow peaks	164°C (peak 3) and 243°C (peak 5)
Annealing	400°, 1.5 hour
Commercial source	Thermo Fisher Scientific, Inc.

There is a much higher response for low energy photon radiation. Peak 5 TL efficiency with respect to gamma rays stays close to unity even for high-LET radiation (see section 2.5).

2.4 ENERGY RESPONSE

Interpretation of the measured doses should also take into account the energy dependence of TL response for the phosphors employed. Whereas LiF detectors behave almost tissue-equivalent for a broad range of photon energies, CaF_2 shows a significant over-response to low-energy photons. This fact is particularly important whenever significant bremsstrahlung components are generated. The situation is illustrated by figure 2.4.1 showing the ratio of the mass energy absorption coefficients, μ_{en}/ρ, for the respective phosphor and tissue.
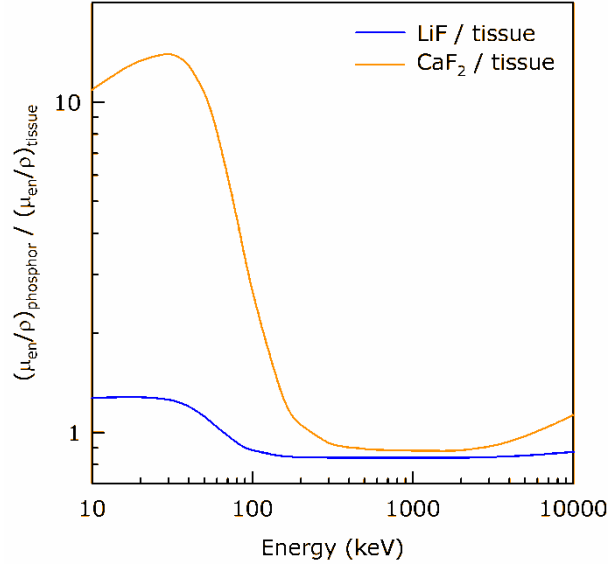
Fig .2.4.1 Calculated energy dependence of the TL response for LiF and CaF_2 phosphors relative to tissue [21]

2.5 NEUTRON DETECTION, PAIR METHOD

As stated in section 2.3 thermal neutron irradiation of TLD-600 produces a triton and an alpha particle by the reaction $^6Li(n,\alpha)^3H$. Thus TLD-600 exhibits a sensitive thermal neutron response. Considering the fact that TLD-700 does not show any significant response to neutrons a comparison between doses measured by both types results in the determination of a (thermal) neutron component. Furthermore, TLD-600 and TLD-700 do not show the exact same response R to gamma radiation and this has thus to be taken into consideration. The following expression for the neutron dose D_n is found:

$$D_n = \frac{R_{600} - \dfrac{R_{700}}{CF_{700}/CF_{600}}}{CF_{600}}$$

Where R_{600} and R_{700} denote the response of the corresponding TLD type and CF_{600} and CF_{700} the corresponding calibration factors.

2.6 HEAVY-ION RESPONSE

When TL detectors are used in radiation fields of high ionization density, it is essential for correct interpretation of the measured data to consider their dose response characteristics. The dose response function for LiF:Mg,Ti phosphors (TLD-600, TLD-700) is linear up to ~10 Gy. For higher doses it starts to become supralinear, followed by a sublinear, saturation-like behaviour in the kGy region (figure 2.6.1). In penetrating the TLD, heavy charged particles deposit extremely high doses in microscopic volumes around the particle track. This causes the registration efficiency of the dosemeter for heavy ions to be different from that for gamma-rays.
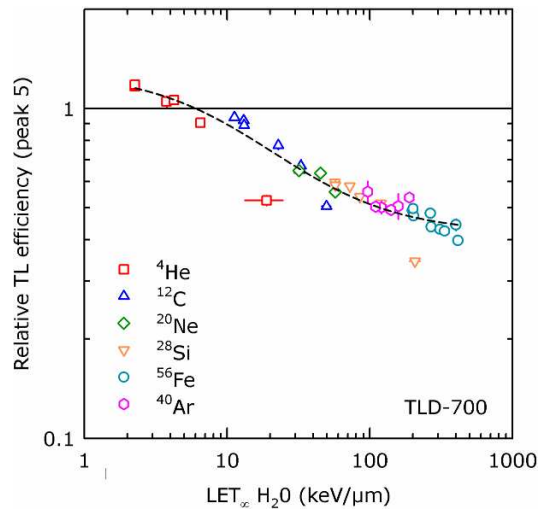
Fig. 2.6.1 Relative TL efficiency of ^{7}LiF:Mg,Ti (TLD-700) for different particle types and LET [21].

Figure 2.6.1 shows that TL efficiency of ^{7}LiF:Mg,Ti (TLD-700) depends on both particle species and LET. An over-response of a few percent is observed for protons and alpha particles, whereas the relative TL efficiency decreases significantly for heavier ions. For mixed radiation fields, it is possible to determine a curve fit as a function of LET and calculate from it the effective TL efficiency which is needed to correct the measured doses. The picture is different for CaF_2:Tm (TLD-300): relative TL efficiency of peak 5 is comparably close to unity, implying that there is no need for correction of measured dose values (figure 2.6.2).
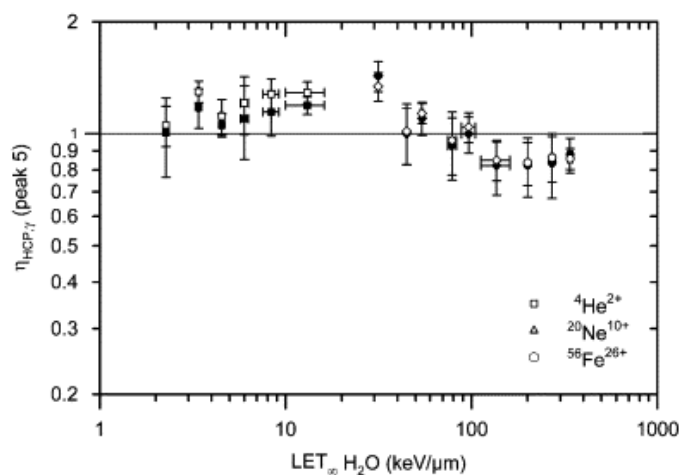
Fig. 2.6.2 TL efficiency with respect to 60Co for glow peak 5 in CaF_2:Tm (TLD-300) for several HCPs (solid symbols: computerized glow curve deconvolution analysis; open symbols: manual analysis) [24].

2.7 HIGH-TEMPERATURE RATIO METHOD

To permit correction of the measured doses for effective TL efficiency in mixed radiation fields of mostly unknown composition it is essential to determine at first the effective LET. For this purpose, the high-temperature ratio (HTR) method was developed at ATI. By analysis of the well-investigated LET-dependent high-temperature TL emission in LiF:Mg,Ti phosphors information about the ionization density—expressed by the effective LET—can be extracted (Figure 2.7.1). The HTR is defined as the ratio of the high-temperature intensities for the radiation under study, ξ_χ and a reference radiation (^{60}Co gamma-rays), ξ_γ.
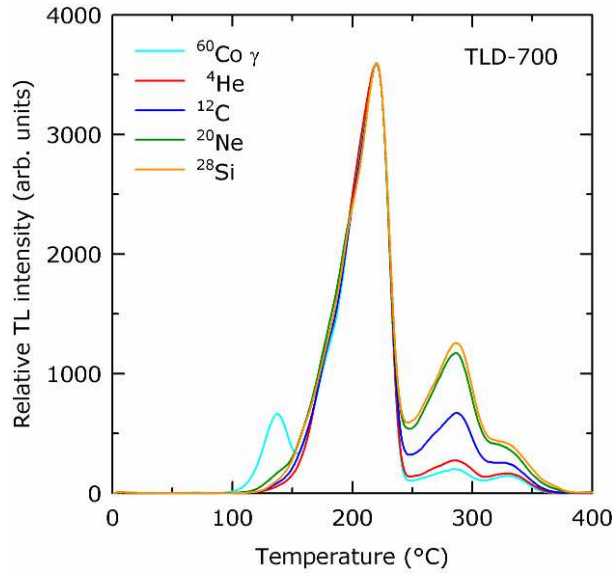
Fig. 2.7.1 LET-dependence of the high-temperature emission in TLD-700 (normalized to peak 5) [21].

$$HTR \equiv \frac{\delta_\gamma}{\delta_\chi} \frac{\xi_\chi}{\xi_\gamma}$$

where δ_χ and δ_γ are the corresponding intensities of the main dosimetry peak 5. For our experimental setup, ξ_χ and ξ_γ are determined by the integral TL emission in the temperature range from 248 to 310 C. Calibrations with HCPs available from the Heavy Ion Medical Accelerator (HIMAC) of the National Institute of Radiological Sciences (NIRS) in Chiba, Japan established a functional relationship of HTR in dependence on LET (fig. 2.7.2). Linearity of the HTR with absorbed dose was verified up to 100 mGy (fig. 2.7.3) and more recently up to 200 mGy [23]. Once the effective LET (L_{eff}) is known, the effective efficiency, η_{eff}, can be derived by applying the curve fit shown in figure 2.6.3:

$$\eta_{eff} = \frac{1 + aL_{eff}}{b + cL_{eff}}$$

where *a*, *b* and *c* are empirical constants. Correction of measured dose values for TL efficiency can now be achieved in two steps: (i) the effective LET is assessed from the HTR, and (ii) is further utilized to determine effective TL efficiency η_{eff} . A plot of TL efficiency over HTR shall further illustrate the correlation (fig. 2.7.4).
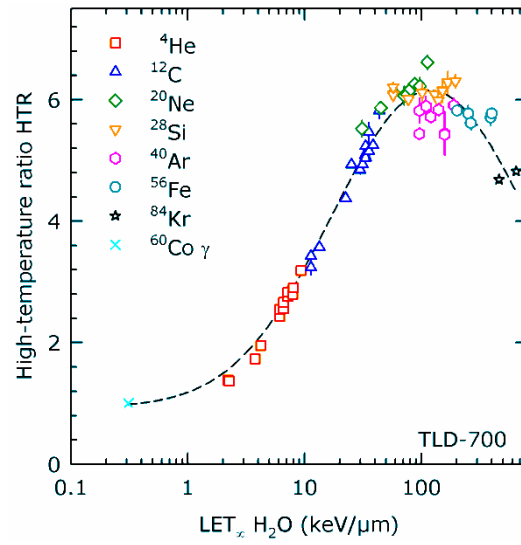
Fig. 2.7.2 LET-dependence of the high-temperature ratio [21].
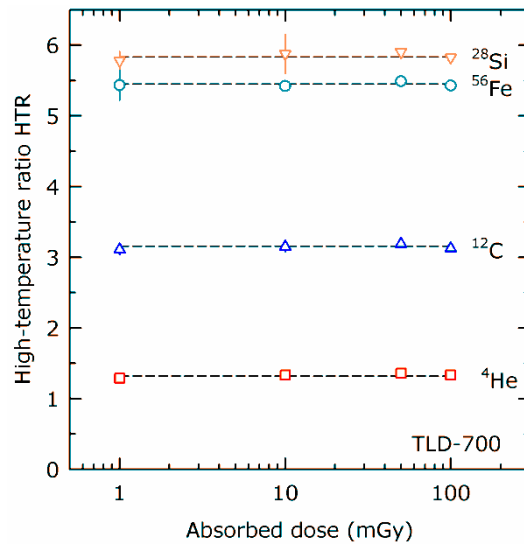
Fig. 2.7.3 Linearity of the high-temperature ratio with absorbed dose [21].
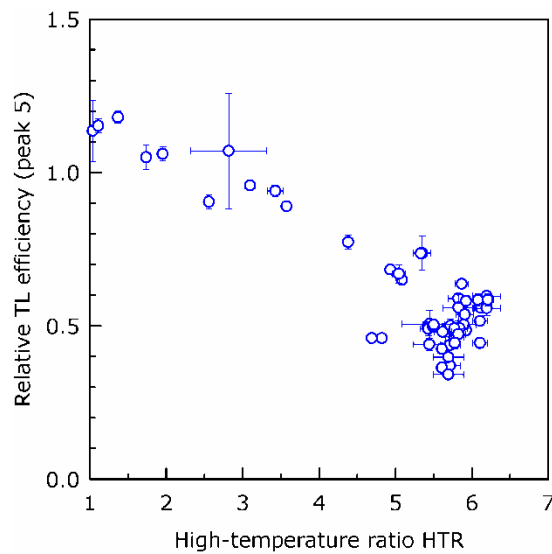
Fig. 2.7.4 Relative TL efficiency of TLD-700 as a function of HTR [21].

3 EXPERIMENTAL RESULTS

3.1 TLD CALIBRATION AND ANALYSIS OF STATISTICAL UNCERTAINTIES

All relevant calibrations took place using a therapeutic ^{60}Co source with pneumatic shutter (Philips Theratron) of the Department of Radiotherapy and Radiobiology, Medical University of Vienna, Austria. The detectors were sealed in polystyrene holders (1 mm thickness). Illustrations are given in figures 3.1.1 and 3.1.2 . A farmer-type high-precision ionization chamber calibrated by the Federal Office of Meteorology and Surveying (BEV), Vienna, Austria, was employed for determining dose to water, using correction factors for temperature and air pressure.

Fig. 3.1.1 ^{60}Co source with pneumatic shutter (Philips Theratron) [source: ATI].
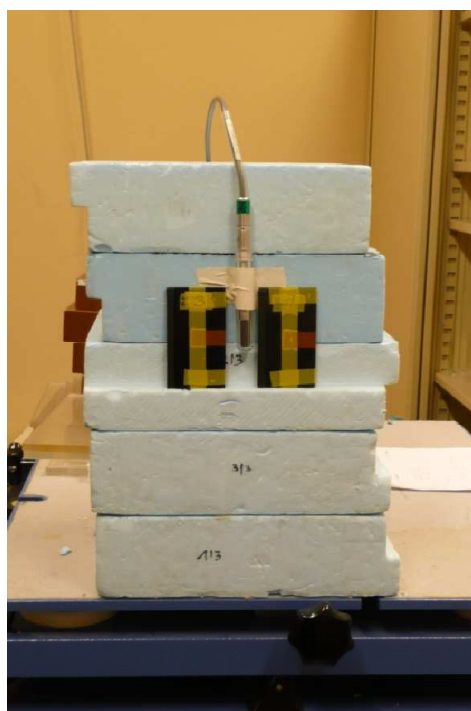
Fig. 3.1.2 Exposure setup: ionization chamber mounted between the polystyrene TLD holders [source:ATI].

Pre-flight calibration was done initially to group the TLDs according to calibration factor to minimise batch variations. TLDs with close calibration factors were chosen for the different slices and boxes i.e. spatial proximity. Three post-flight calibrations for all TLDs were done due to investigate reproducibility in the TLD responses. Further ATI and AKH calibrations (^{137}Cs source at the ATI and ^{60}Co source at the Medical University of Vienna) were conducted with a batch of 2x32 chips to clarify these variations (figs. 3.1.3 and 3.1.4)
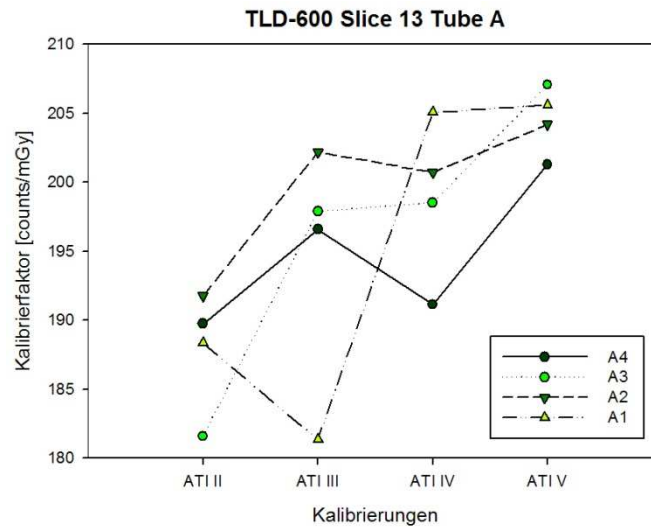
Fig.3.1.3 Example of 4 TLD-600 chips and their variation of calibration factors (^{137}Cs source ATI).
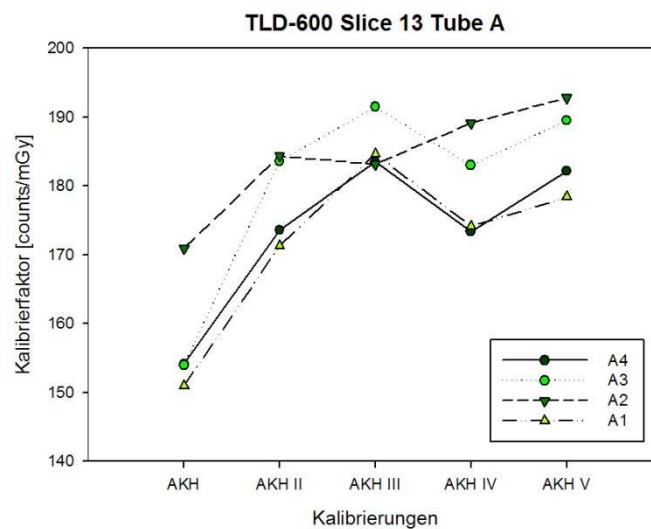
Fig.3.1.4 Example of 4 TLD-600 chips and their variation of calibration factors (^{60}Co source at the Medical University of Vienna = AKH).

The question of long time stability after tempering was addressed due to the fact that out of practical reasons more chips were pre-annealed at once than were measured in one run. A group of eight chips per TLD type (TLD-600 and TLD-700) was irradiated, pre-annealed and readout after 1, 24, 51 and 72 hours time delay. The mean of the gained calibration factors was taken and a double-sigma standard deviation (95 % confidence interval) was applied. Then again the mean of these values was taken and yet another double-sigma standard deviation was applied. After more than 800 hours each group was checked again for discrepancies. The analysis showed no significant tendency towards an altered TL signal (fig. 3.1.5).
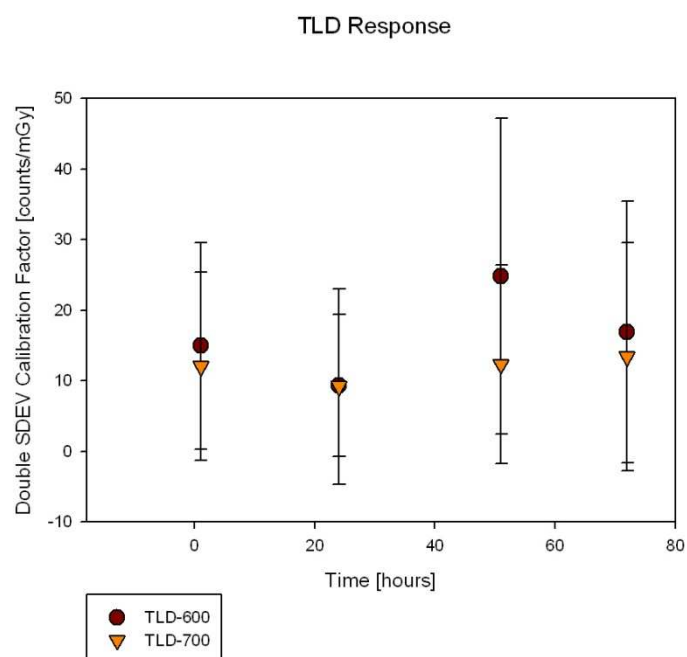
Fig.3.1.5 TLD Response after tempering. Error bars are double-sigma standard deviation (95% confidence interval).

The overall **mean reproducibility** was determined to be **7.7 % for all TLDs** as the upper bounder with a double-sigma standard deviation. The reproducibility of a single TLD was determined firstly by five consecutive calibrations(batch of 2x32 chips, TLD-600 and TLD-700) which resulted in a mean value and a double sigma standard deviation. This is equal to a mean reproducibility, i.e. reliability of a single chip measurement.

3.2 BACKGROUND DOSE ASSESSMENT MATROSHKA II A

A reference detector set was added to the TLDs integrated in Matroshka. During a 30 day period all TLDs were onboard the ISS but were not yet integrated into the phantom. The reference set remained outside for monitoring for the entire exposure period. 367 days of exposure were recorded of which 30 days remain to be subtracted from the integrated TLDs in order to account for that accumulated dose outside the phantom. To gain dose rates all accumulated doses had to be divided by **337 days**.

	TLD-700	TLD-600	TLD-300
Reference dose (mGy)	86.2	104.6	91.9
Daily dose rate (mGy/d)	0.23	0.29	0.25
Total dose for 30 days (mGy)	**7.0**	**8.6**	**7.5**

Tab. 3.2.1 Reference dosemeters accumulated dose and dose rate.

The issue of storage on the ground and transport times on ground and into space (and back to earth, respectively) has been addressed and accounted for.

3.3 DEPTH DOSE DISTRIBUTION MATROSHKA II A

The following 3D graphs (fig. 3.3.2 – 3.3.15) depict the accumulated depth dose distribution for each individual slice. TLD-700 data -background corrected- were used. Figure 3.3.1 shows the coordinate system that was used.
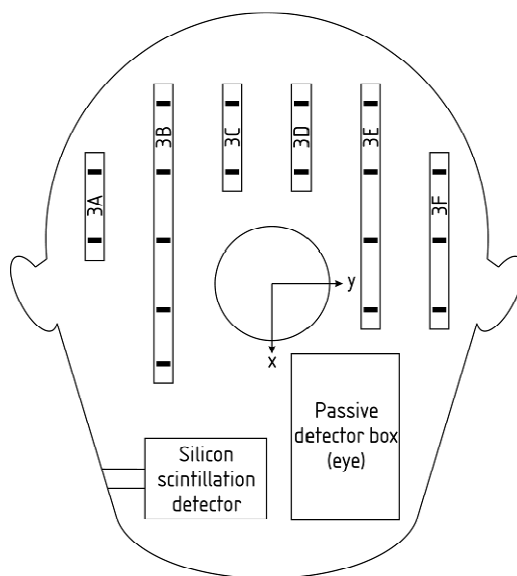
Fig. 3.3.1 Illustration of the Matroshka coordinate system used in the three-dimensional dose plots.
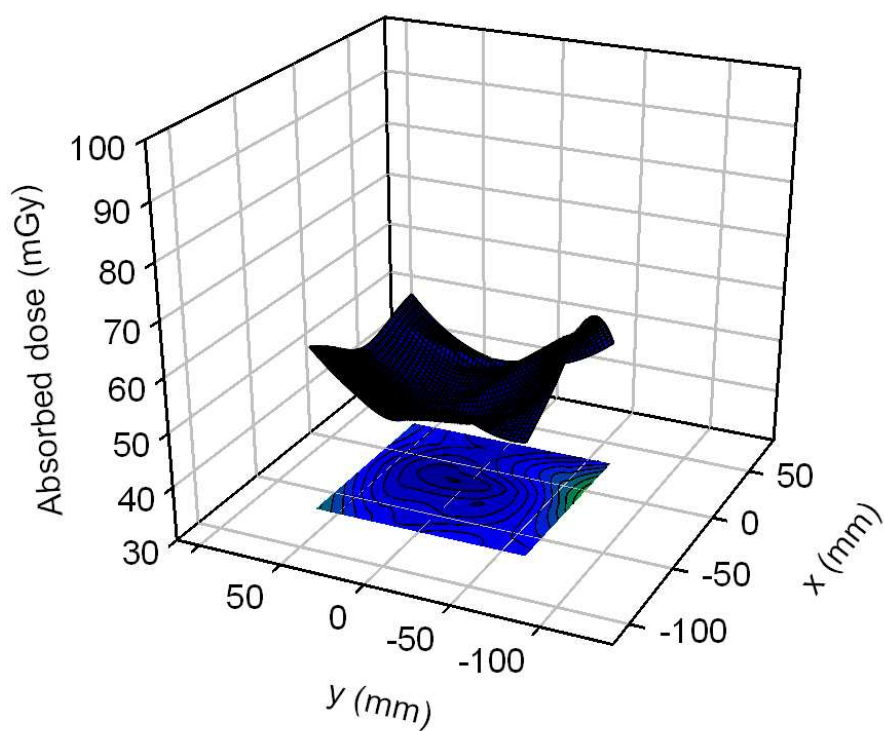
Fig. 3.3.2 Slice 3
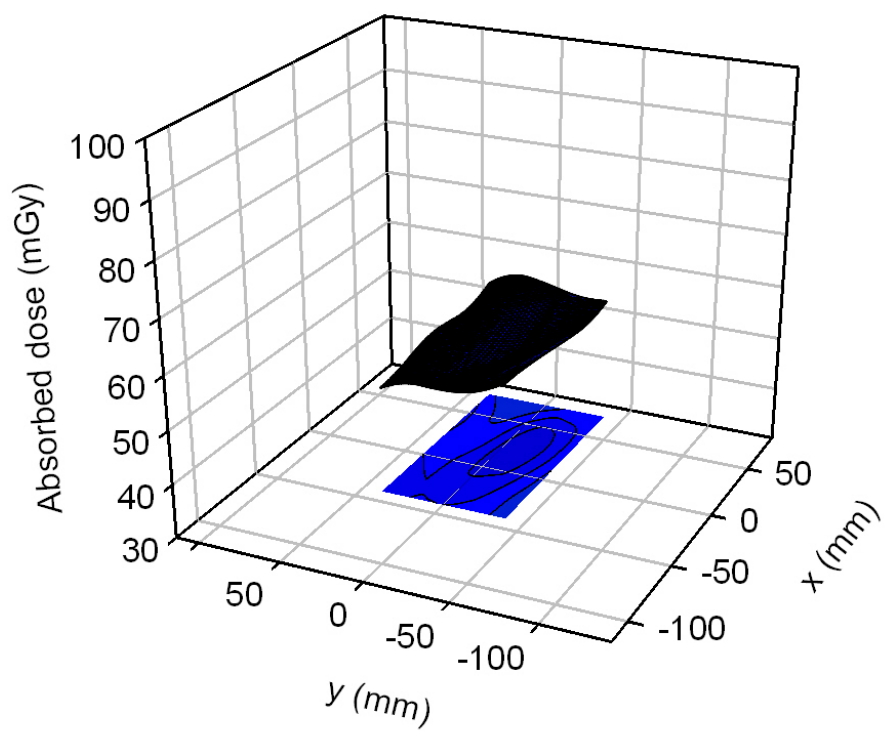
Fig. 3.3.3 Slice 7
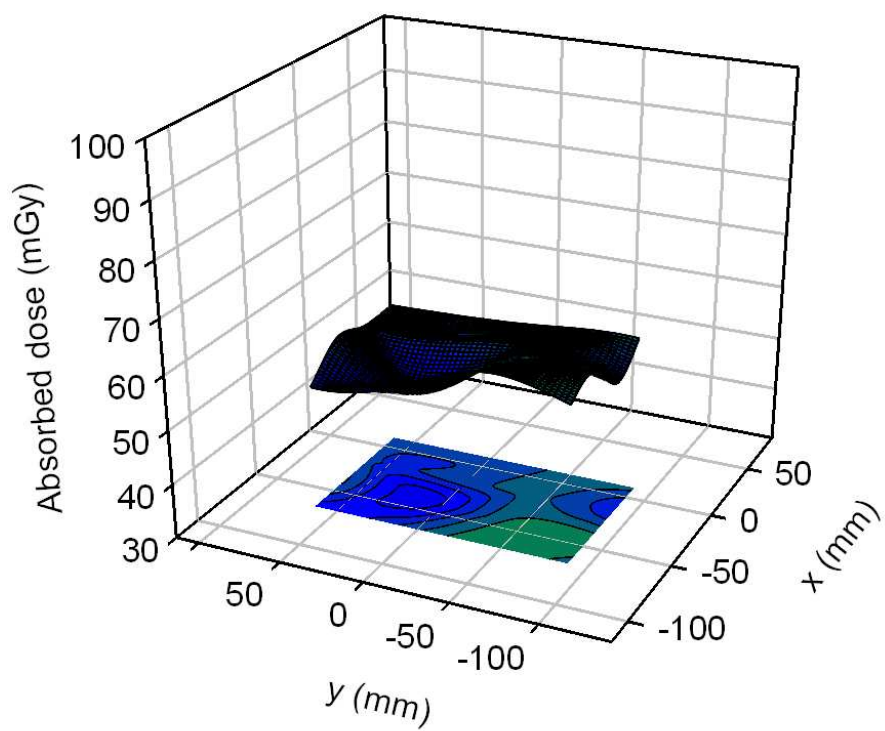
Fig. 3.3.4 Slice 11
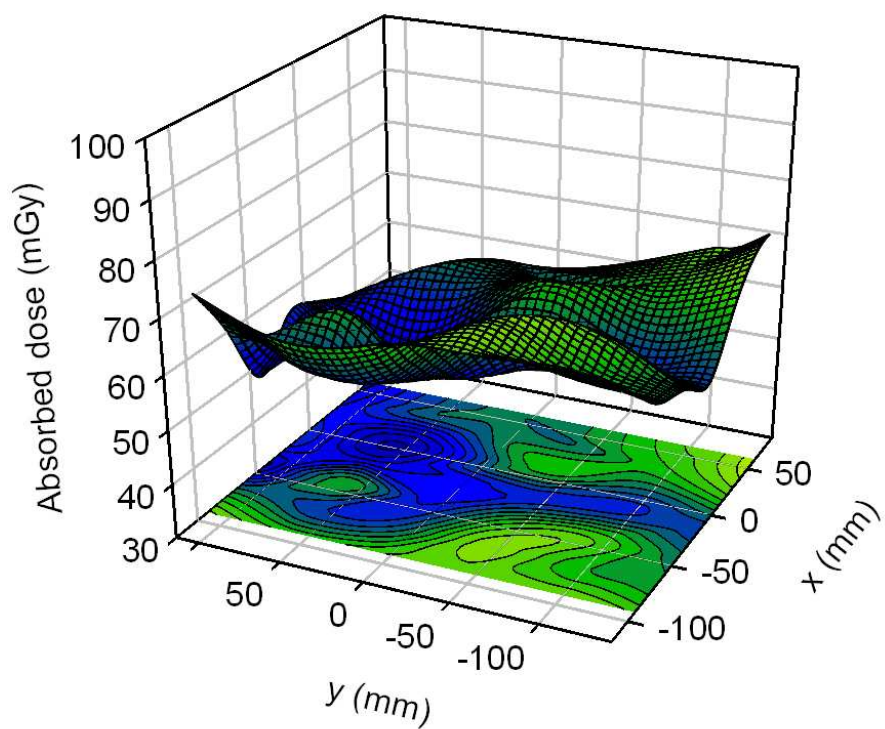
Fig. 3.3.5 Slice13
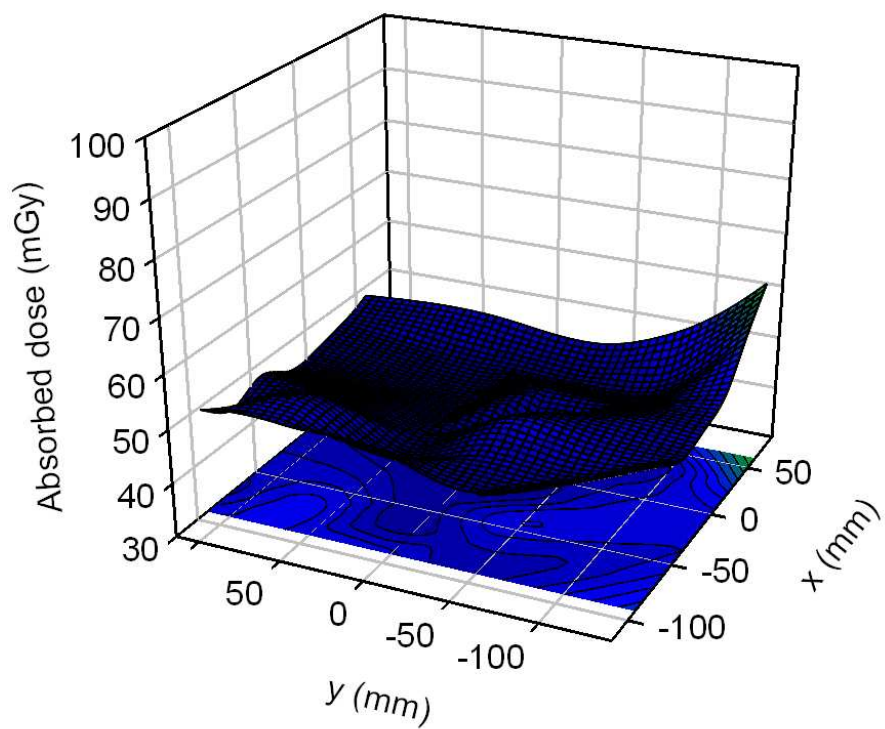
Fig. 3.3.6 Slice 15
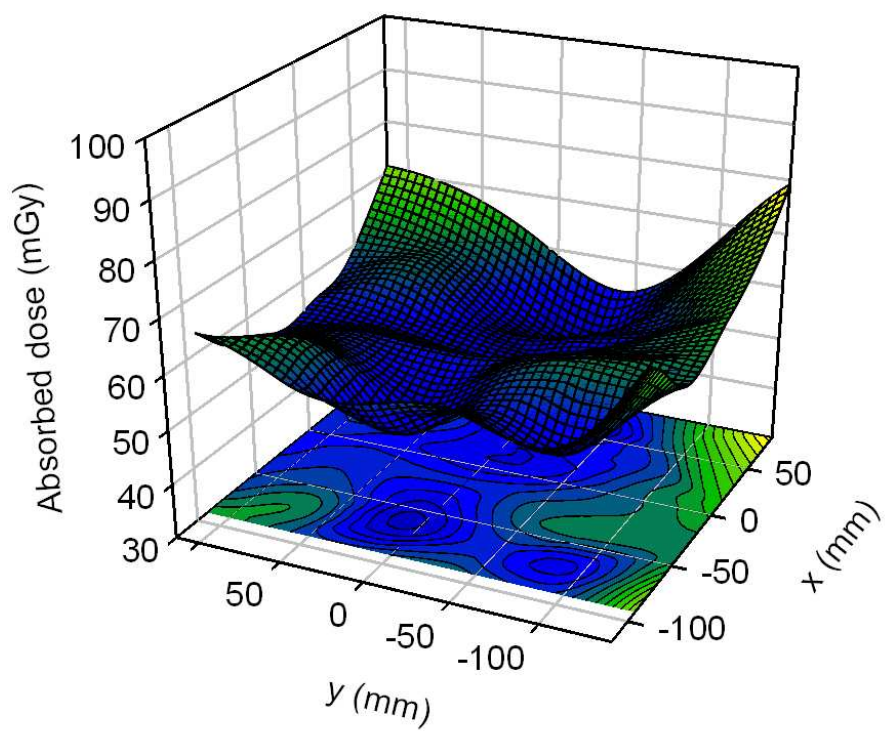
Fig. 3.3.7 Slice 17
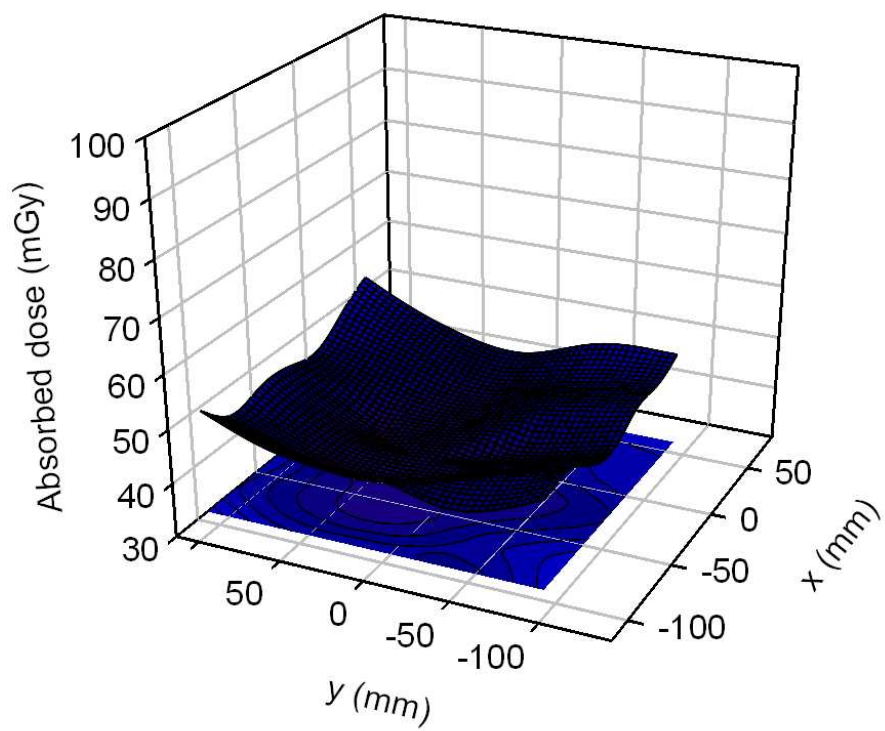
Fig. 3.3.8 Slice 19
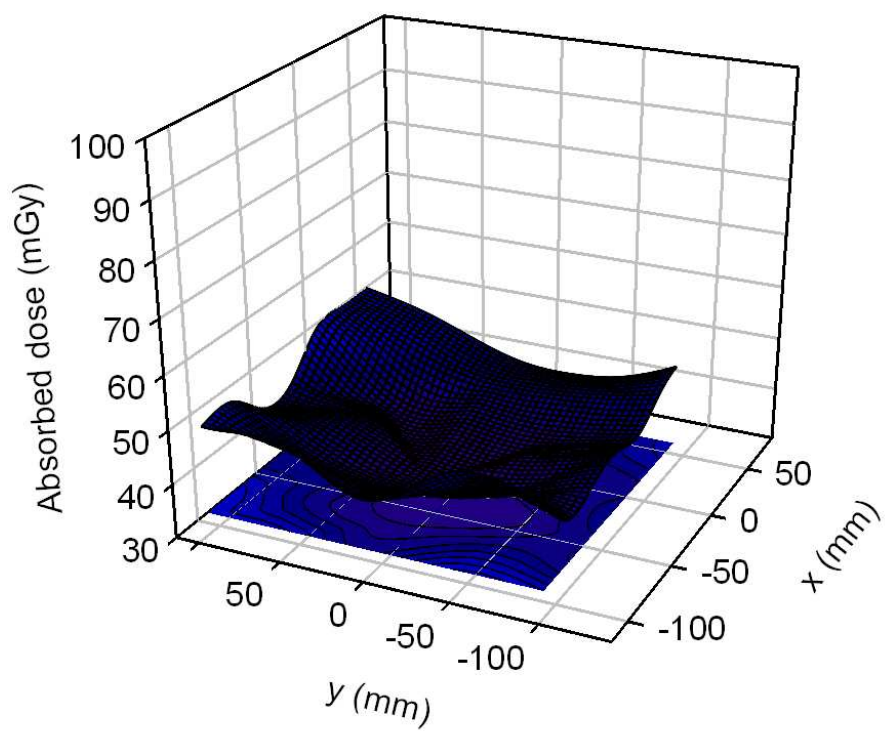
Fig .3.3.9 Slice 21
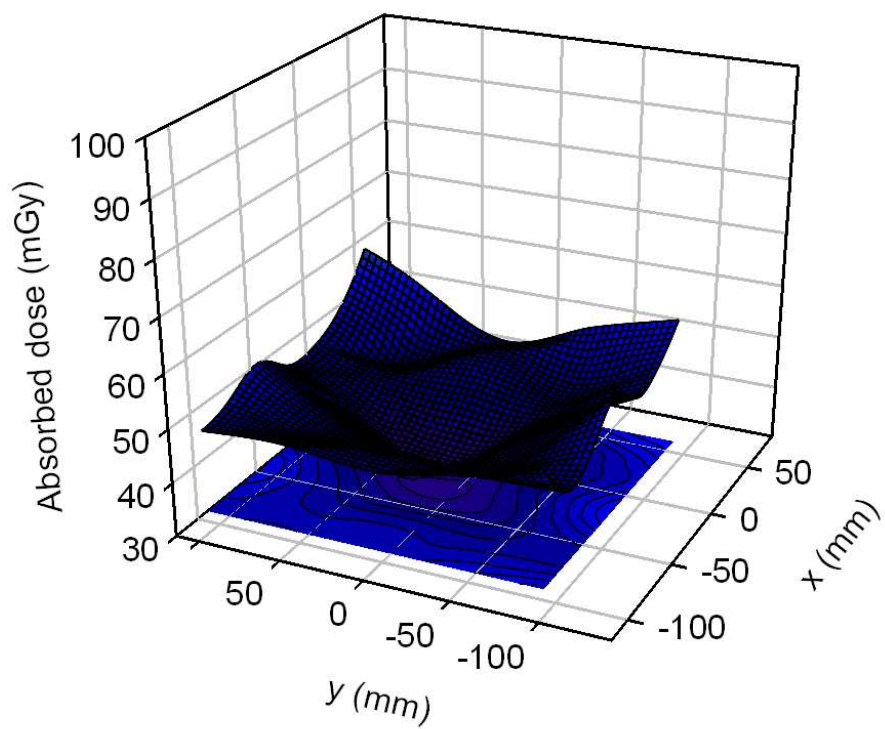
Fig. 3.3.10 Slice 23
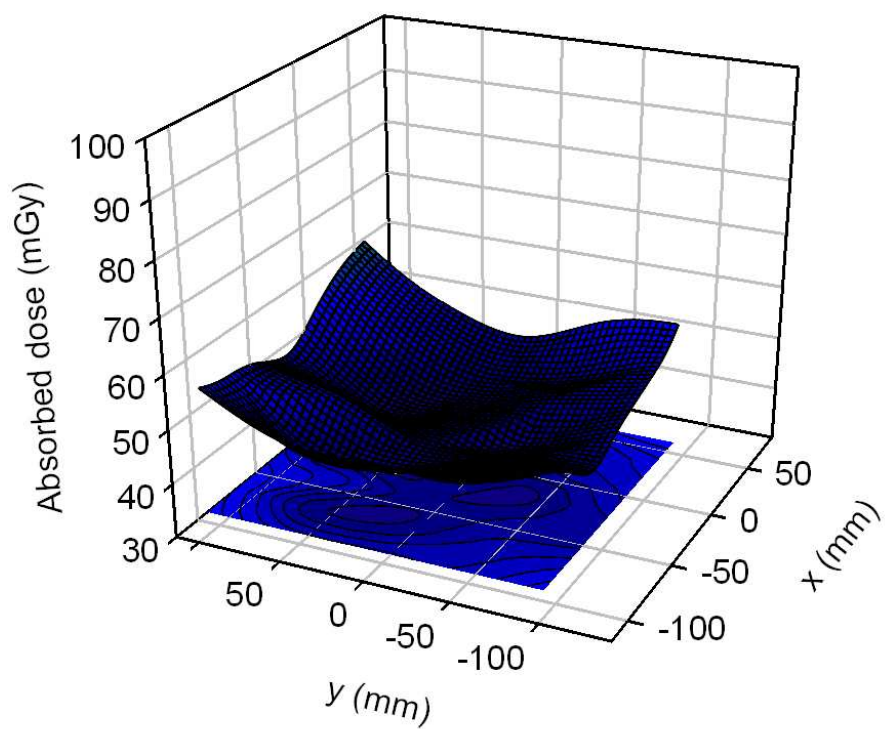
Fig. 3.3.11 Slice 25
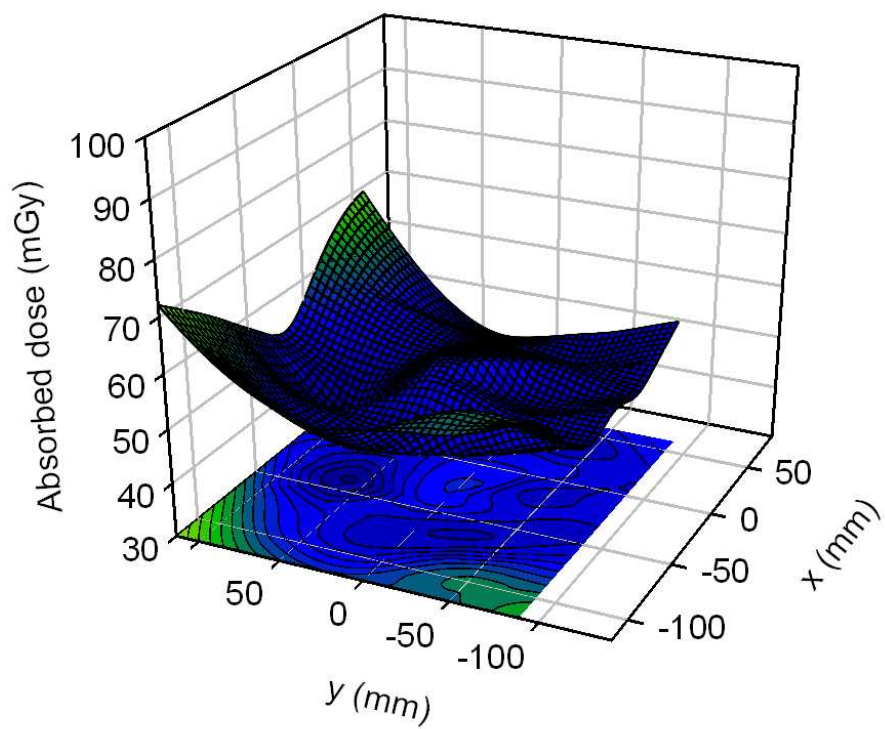
Fig .3.3.12 Slice 27
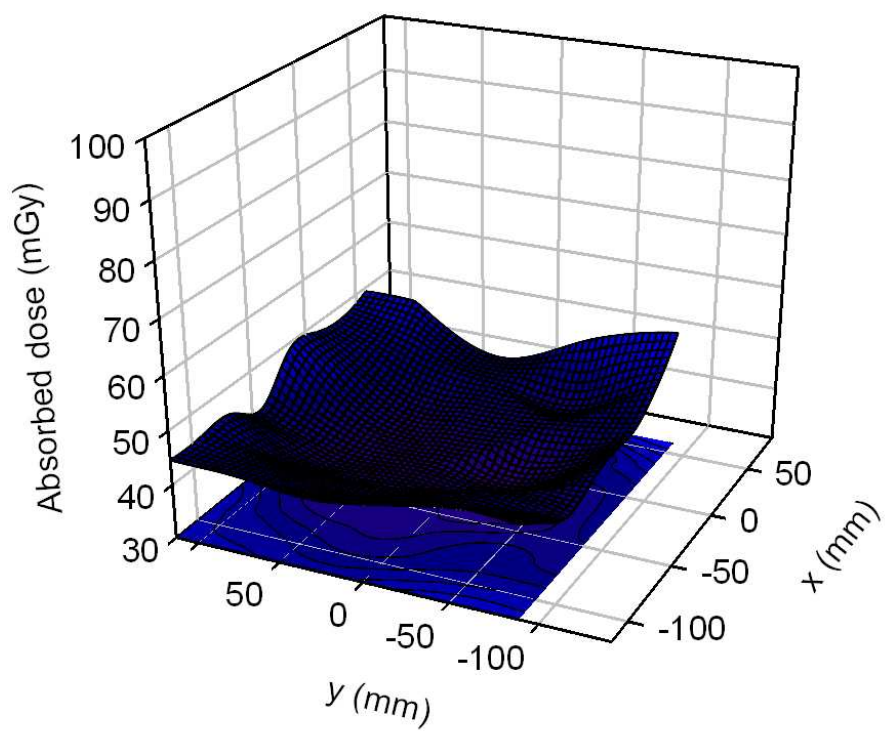
Fig. 3.3.13 Slice 29
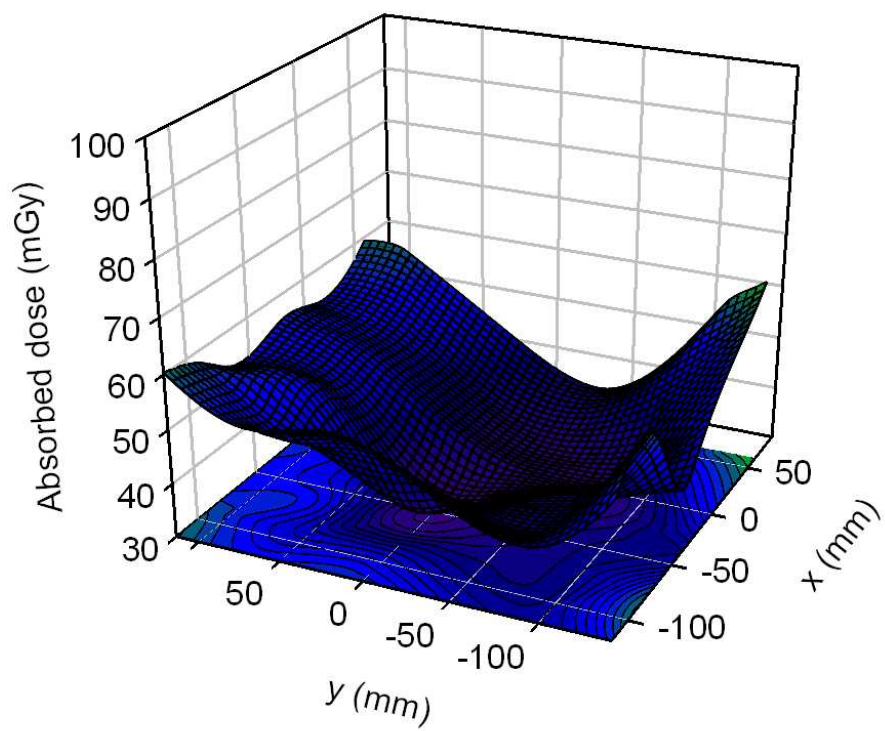
Fig. 3.3.14 Slice 31
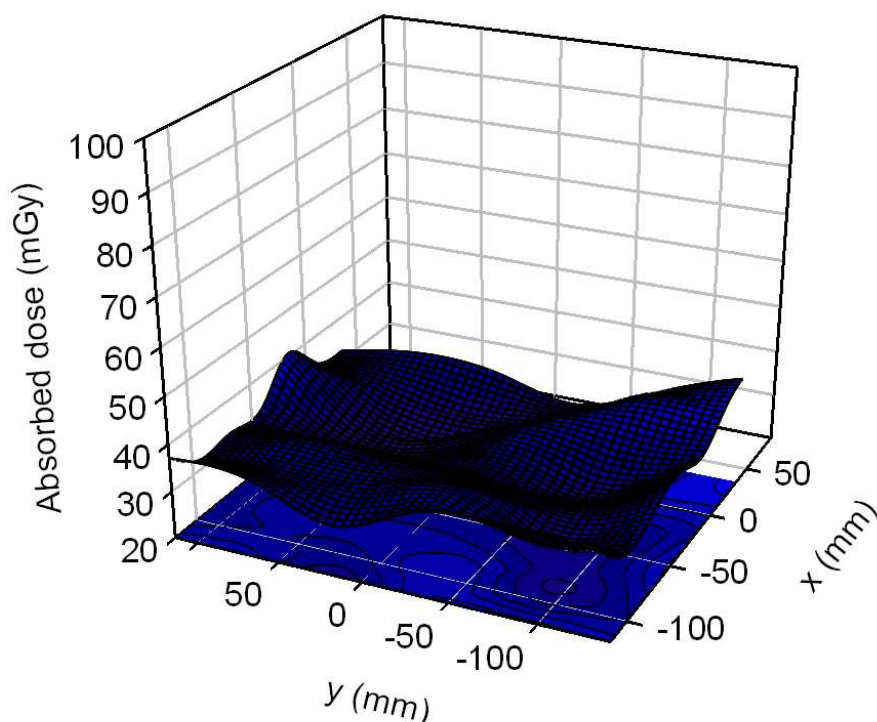
Fig .3.3.15 Slice 33

An apparent dose gradient from head to bottom can be seen as well as a 'cushion' form for most slices, i.e. a dose gradient from the outer parts of the phantom declining inside. Slice 7 shows the opposite behaviour. This might be linked to the structure of the phantom itself since this could be seen for the outside exposure as well (different batch of TLDs).

Figures 3.3.16 – 3.3.19 show the HTR values for both TLD-600 and TLD-700 for different cross sections of the phantom. Clearly the TLD-600 HTR value is biased by the neutron contribution and thus much higher than for TLD-700. As expected a significant built-up inside the phantom can be observed corresponding to a higher LET. This behaviour is not observed for TLD-700. Clearly a thermalization of neutrons can be seen as the cause of this.

Tables 3.3.1 – 3.3.14 show the dose rates obtained for each individual chip as well as the HTR values for both TLD-600 and TLD-700 numerically. Background dose corrections for each type of TLD according to section 3.2 have been applied. No statistical uncertainty could be given for each individual chip (i.e. position) but a mean reproducibility according to section 3.2
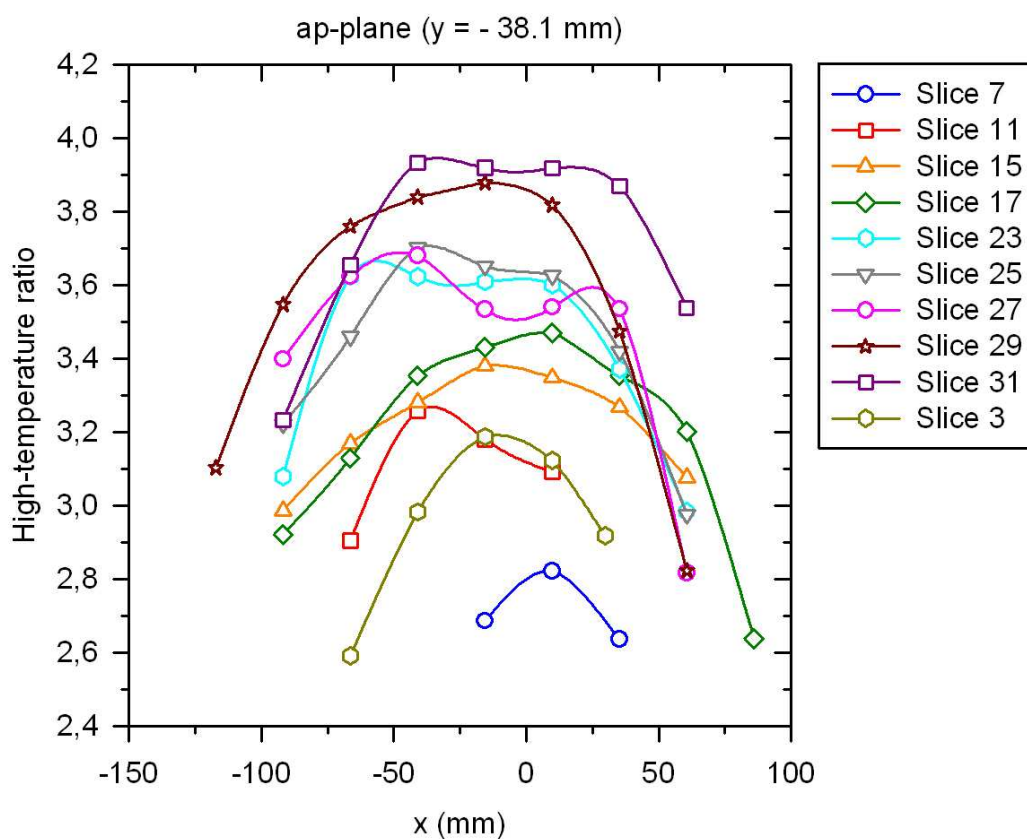
Fig. 3.3.16 HTR values for TLD-600 (y=-38.1mm)
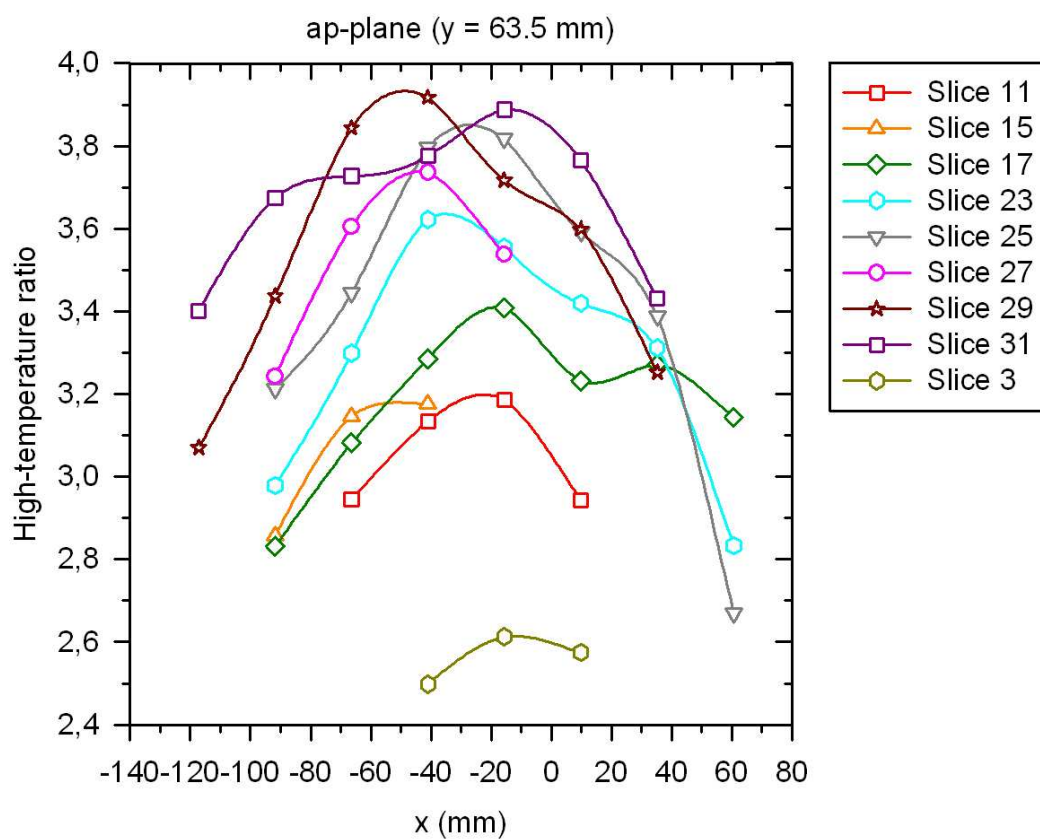
Fig. 3.3.17 HTR values for TLD-600 (y= 63.5mm)
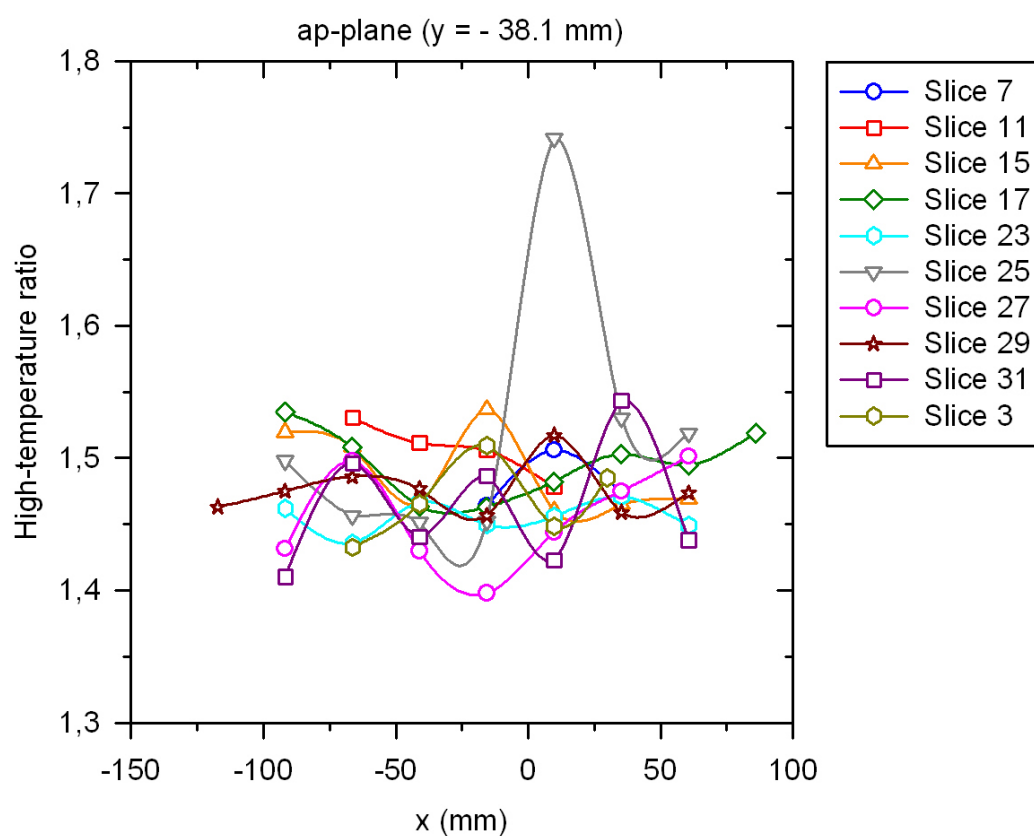
Fig. 3.3.18 HTR values for TLD-700 (y= -38.1mm)
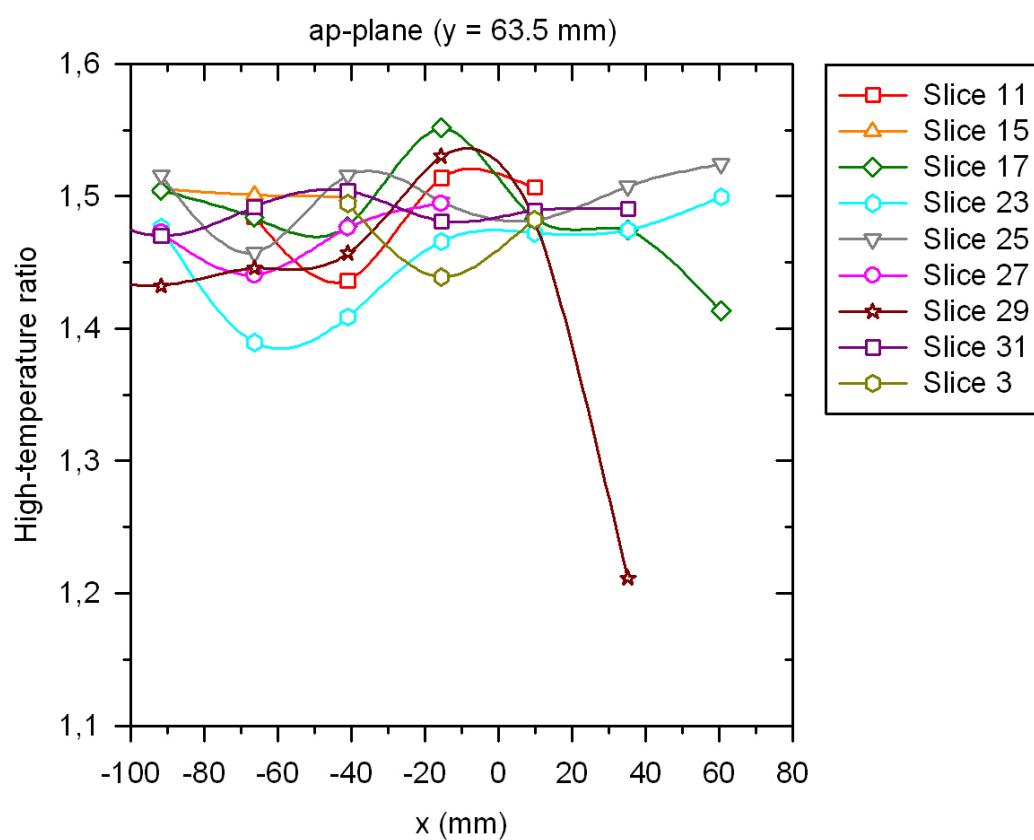
Fig. 3.3.19 HTR values for TLD-700 (Y= 63.5 mm)

Slice 3 (Eye)	TLD-600		TLD-700	
Chip ID	Dose Rate [mGy/d]	HTR	Dose Rate [mGy/d]	HTR
A2	0.24	2.463	0.168	1.50
A1	0.25	2.323	0.186	1.45
B5	0.23	2.578	0.157	1.48
B4	0.23	3.158	0.152	1.47
B3	0.22	3.176	0.153	1.49
B2	0.23	3.235	0.168	1.44
B1	0.24	3.002	0.148	1.49
C2	0.23	3.098	0.162	1.45
C1	0.23	3.432	0.142	1.49
D2	0.24	2.898	0.152	1.46
D1	0.24	3.382	0.145	1.46
E4	0.23	2.720	0.163	1.46
E3	0.23	3.246	0.146	1.43
E2	0.23	3.405	0.137	1.46
E1	0.23	3.442	0.146	1.48
F3	0.21	2.544	0.170	1.44
F2	0.23	2.683	0.160	1.45
F1	0.23	2.597	0.165	1.46

Tab. 3.3.1 Slice 3 dose rates and HTR values TLD-600 and TLD-700

Slice 7	TLD-600		TLD-700	
Chip ID	Dose Rate [mGy/d]	HTR	Dose Rate [mGy/d]	HTR
A3	0.23	2.767	0.17	1.463
A2	0.21	2.931	0.16	1.485
A1	0.245	2.673	0.16	1.451
B2	0.24	2.646	0.16	1.479
B1	0.23	2.615	0.17	1.489
C2	0.24	2.874	0.16	1.519
C1	0.24	2.758	0.16	1.509
D2	0.23	3.090	0.15	1.481
D1	0.23	3.039	0.16	1.482
E3	0.23	3.058	0.15	1.494
E2	0.23	3.005	0.16	1.482
E1	0.22	2.889	0.16	1.486

Tab. 3.3.2 Slice 7 dose rates and HTR values TLD-600 and TLD-700

Slice 11	TLD-600		TLD-700	
Chip ID	Dose Rate [mGy/d]	HTR	Dose Rate [mGy/d]	HTR
A4	0.26	2.878	0.18	1.478
A3	0.25	2.982	0.18	1.469
A2	0.23	2.959	0.16	1.506
A1	0.23	2.716	0.18	1.463
C4	0.28	3.000	0.19	1.513
C3	0.28	3.156	0.18	1.459
C2	0.28	3.282	0.18	1.448
C1	0.26	3.153	0.18	1.453
E4	0.26	2.566	0.21	1.446
E2	0.27	2.547	0.19	1.464
F2	0.28	3.284	0.17	1.502
F1	0.26	3.380	0.15	1.484
H4	0.22	2.990	0.16	1.418
H3	0.27	3.112	0.18	1.479
H2	0.27	3.138	0.17	1.515
H1	0.27	2.998	0.17	1.477

Tab. 3.3.3 Slice 11 dose rates and HTR values TLD-600 and TLD-700

Slice 13	TLD-600		TLD-700	
Chip ID	Dose Rate [mGy/d]	HTR	Dose Rate [mGy/d]	HTR
A4	0.27	2.767	0.19	1.445
A3	0.26	3.027	0.18	1.444
A2	0.26	3.087	0.17	1.449
A1	0.28	2.967	0.19	1.458
C6	0.27	2.839	0.21	1.442
C5	0.26	3.112	0.20	1.470
C4	0.26	3.217	0.20	1.448
C3	0.26	3.195	0.17	1.481
C2	0.27	3.233	0.18	1.447
C1	0.25	2.997	0.20	1.438
E6	0.30	2.935	0.21	1.465
E5	0.28	3.121	0.21	1.423
E4	0.28	3.218	0.19	1.447
E3	0.29	3.317	0.17	1.474
E2	0.27	3.241	0.20	1.450
E1	0.27	3.130	0.18	1.463
F1	0.27	2.639	0.18	1.470
H1	0.27	3.178	0.18	1.446
I3	0.26	2.961	0.20	1.426
I2	0.26	3.360	0.17	1.463
I1	0.26	3.499	0.16	1.546
L6	0.22	2.878	0.20	1.430
L5	0.26	3.122	0.17	1.456
L4	0.29	3.206	0.19	1.462
L3	0.25	3.286	0.15	1.524
L2	0.24	3.162	0.14	1.478
L1	0.27	3.097	0.17	1.441
N5	0.27	3.123	0.18	1.497
N4	0.28	3.261	0.14	1.535
N3	0.27	3.290	0.17	1.477
N2	0.27	3.314	0.16	1.484
N1	0.30	2.962	0.16	1.480

Tab. 3.3.4 Slice 13 dose rates and HTR values TLD-600 and TLD-700

Slice 15 (Lung)	TLD-600		TLD-700	
Chip ID	Dose Rate [mGy/d]	HTR	Dose Rate [mGy/d]	HTR
A5	0.21	2.884	0.16	1.523
A4	0.22	3.092	0.15	1.526
A3	0.21	3.214	0.15	1.505
A2	0.22	3.013	0.15	1.554
A1	0.22	2.528	0.17	1.543
C7	0.22	2.915	0.15	1.526
C6	0.22	3.089	0.14	1.540
C5	0.21	3.232	0.15	1.512
C4	0.21	3.208	0.15	1.539
C3	0.20	3.269	0.14	1.536
C2	0.21	3.233	0.13	1.482
C1	0.22	2.669	0.16	1.499
E7	0.21	3.074	0.14	1.507
E6	0.23	3.263	0.14	1.499
E5	0.22	3.324	0.15	1.506
E4	0.21	3.522	0.13	1.515
E3	0.23	3.472	0.14	1.477
E2	0.22	3.327	0.13	1.494
E1	0.22	3.234	0.14	1.480
H2	0.20	3.578	0.13	1.541
H1	0.21	3.323	0.15	1.502
I3	0.22	3.219	0.15	1.514
I2	0.21	3.505	0.13	1.490
I1	0.21	3.686	0.13	1.481
L3	0.22	3.035	0.15	1.504
L2	0.21	3.248	0.15	1.540
L1	0.21	3.353	0.14	1.486
N6	0.21	2.825	0.15	1.529
N5	0.21	3.250	0.14	1.526
N4	0.22	3.317	0.14	1.514
N3	0.20	3.360	0.14	1.539
N2	0.22	3.508	0.14	1.516
N1	0.22	3.230	0.14	1.495

Tab. 3.3.5 Slice 15 dose rates and HTR values TLD-600 and TLD-700

Slice 17	TLD-600		TLD-700	
Chip ID	Dose Rate [mGy/d]	HTR	Dose Rate [mGy/d]	HTR
A4	0.27	2.516	0.20	1.524
A3	0.25	2.652	0.18	1.443
A2	0.25	2,644	0.19	1.482
A1	0.27	2.388	0.20	1.472
C7	0.27	2.881	0.17	1.459
C6	0.25	3.121	0.16	1.485
C5	0.23	3.103	0.18	1.492
C4	0.27	3.264	0.18	1.464
C3	0.25	3.203	0.18	1.473
C2	0.24	3.216	0.17	1.502
C1	0.26	2.930	0.18	1.498
E8	0.25	3.027	0.18	1.540
E7	0.24	3.269	0.17	1.509
E6	0.25	3.474	0.17	1.545
E5	0.28	3.564	0.17	1.530
E4	0.26	3.588	0.15	1.484
E3	0.25	3.432	0.16	1.483
E2	0.22	3.374	0.14	1.519
E1	0.22	2.658	0.16	1.521
H3	0.26	3.568	0.15	1.474
H2	0.26	3.496	0.16	1.475
H1	0.27	2.921	0.18	1.500
I3	0.26	3.258	0.17	1.497
I2	0.25	3.534	0.14	1.529
I1	0.24	3.755	0.15	1.486
L7	0.25	3.005	0.18	1.523
L6	0.24	3.279	0.18	1.494
L5	0.25	3.418	0.17	1.475
L4	0.28	3.402	0.17	1.506
L3	0.26	3.370	0.16	1.493
L2	0.23	3.344	0.18	1.498
L1	0.25	3.248	0.18	1.425
N7	0.25	2.878	0.19	1.398
N6	0.27	3.155	0.17	1.516
N5	0.26	3.214	0.17	1.440
N4	0.28	3.296	0.16	1.510
N3	0.26	3.327	0.17	1.498
N2	0.26	3.206	0.17	1.488
N1	0.26	2.851	0.19	1.514

Tab. 3.3.6 Slice 17 dose rates and HTR values TLD-600 and TLD-700

Slice 19	TLD-600		TLD-700	
Chip ID	Dose Rate [mGy/d]	HTR	Dose Rate [mGy/d]	HTR
B7	0.22	3.051	0.14	1.501
B6	0.20	3.253	0.14	1.544
B5	0.21	3.358	0.13	1.494
B4	0.20	3.325	0.13	1.480
B3	0.20	3.321	0.14	1.479
B2	0.21	3.057	0.14	1.486
B1	0.24	2.617	0.14	1.509
D7	0,21	3.132	0.12	1.530
D6	0.19	3.628	0.13	1.497
D5	0.21	3.727	0.12	1.462
D4	0.20	3.736	0.12	1.503
D3	0.20	3.692	0.13	1.477
D2	0.22	3.540	0.13	1.492
D1	0.22	3.219	0.14	1.493
G2	0.21	3.678	0.12	1.484
G1	0.20	3.492	0.13	1.501
H3	0.20	3.217	0.13	1.466
H2	0.19	3.422	0.12	1.470
H1	0.20	3.756	0.12	1.439
K7	0.20	3.125	0.13	1.540
K6	0.20	3.382	0.12	1.555
K5	0.22	3.499	0.12	1.436
K4	0.20	3.586	0.11	1.489
K3	0.20	3.541	0.12	1.525
K2	0.20	3.298	0.13	1.453
K1	0.21	3.132	0.14	1.480
M6	0.22	2.877	0.15	1.519
M5	0.21	3.236	0.13	1.507
M4	0.22	3.197	0.14	1.486
M3	0.22	3.199	0.14	1.526
M2	0.21	3.217	0.13	1.514
M1	0.21	3.084	0.15	1.463

Tab. 3.3.7 Slice 19 dose rates and HTR values TLD-600 and TLD-700

Slice 21	TLD-600		TLD-700	
Chip ID	Dose Rate [mGy/d]	HTR	Dose Rate [mGy/d]	HTR
B6	0.22	2.992	0.14	1.409
B5	0.20	3.381	0.13	1.318
B4	0.20	3.451	0.12	1.365
B3	0.19	3.562	0.13	1.307
B2	0.20	3.424	0.12	1.411
B1	0.20	3.044	0.13	1.229
D7	0.22	3.252	0.15	1.318
D6	0.20	3.689	0.12	1.598
D5	0.21	3.592	0.11	1.403
D4	0.20	3.694	0.11	1.294
D3	0.21	3.743	0.11	1.283
D2	0.20	3.544	0.12	1.210
D1	0.21	2.929	0.12	1.275
G2	0.22	3.668	0.12	1.391
G1	0.22	3.296	0.12	1.371
H3	0.20	3.360	0.12	1.320
H2	0.21	3.609	0.11	1.352
H1	0.19	3.850	0.11	1.280
K7	0.18	3.265	0.14	1.310
K6	0.21	3.633	0.12	1.429
K5	0.20	3.694	0.12	1.378
K4	0.22	3.717	0.12	1.181
K3	0.20	3.610	0.11	1.282
K2	0.20	3.212	0.13	1.311
K1	0.20	2.894	0.14	1.120
M6	0.22	2.772	0.14	1.421
M5	0.21	3.242	0.14	1.336
M4	0.22	3.362	0.13	1.357
M3	0.23	3.415	0.13	1.485
M2	0.21	3.202	0.15	1.274
M1	0.20	2.800	0.15	1.321

Tab. 3.3.8 Slice 21 dose rates and HTR values TLD-600 and TLD-700

Slice 23	TLD-600		TLD-700	
Chip ID	Dose Rate [mGy/d]	HTR	Dose Rate [mGy/d]	HTR
B6	0.23	2.784	0.15	1.409
B5	0.23	3.263	0.13	1.471
B4	0.23	3.387	0.14	1.524
B3	0.21	3.542	0.16	1.493
B2	0.24	3.181	0.14	1.470
B1	0.21	3.008	0.15	1.518
D7	0.22	3.252	0.14	1.482
D6	0.20	3.551	0.13	1.409
D5	0.22	3.718	0.12	1.497
D4	0.21	3.802	0.12	1.470
D3	0.21	3.774	0.13	1.492
D2	0.20	3.495	0.13	1.504
D1	0.22	3.021	0.15	1.468
G2	0.23	3.638	0.14	1.510
G1	0.21	3.265	0.13	1.467
H3	0.21	3.265	0,14	1.518
H2	0.21	3.688	0,13	1.468
H1	0.22	3.718	0.11	1.459
K7	0.20	3.135	0.14	1.459
K6	0.20	3.450	0.13	1.400
K5	0.19	3.712	0.13	1.453
K4	0.20	3.797	0.12	1.479
K3	0.20	3.615	0.13	1.492
K2	0.20	3.448	0.13	1.489
K1	0.21	3.006	0.15	1.554
M4	0.22	3.042	0.14	1.506
M3	0.22	3.172	0.15	1.525
M2	0.21	3.277	0.14	1.497
M1	0.22	3.104	0.14	1.501

Tab. 3.3.9 Slice 23 dose rates and HTR values TLD-600 and TLD-700

Slice 25	TLD-600		TLD-700	
Chip ID	Dose Rate [mGy/d]	HTR	Dose Rate [mGy/d]	HTR
B6	0.23	2.980	0.16	1.500
B5	0.22	3.397	0.14	1.474
B4	0.21	3.427	0.13	1.485
B3	0.23	3.380	0.14	1.523
B2	0.21	3.228	0.14	1.444
B1	0.23	2.806	0.15	1.580
D7	0.23	3.324	0.14	1.524
D6	0.21	3.657	0.13	1.447
D5	0.22	3.826	0.13	1.454
D4	0.21	3.826	0.12	1.505
D3	0.21	3.739	0.13	1.492
D2	0.22	3.550	0.13	1.541
D1	0.21	3.102	0.15	1.554
G2	0.23	3.788	0.13	1.513
G1	0.22	3.313	0.14	1.487
H3	0.22	3.224	0.14	1.505
H2	0.22	3.688	0.12	1.490
H1	0.21	3.837	0.12	1.516
K7	0.24	3.368	0.14	1.509
K6	0.23	3.617	0.12	1.478
K5	0.21	3.945	0.14	1.534
K4	0.20	3.918	0.12	1.538
K3	0.21	3.808	0.13	1.554
K2	0.22	3.522	0.14	1.531
K1	0.23	2.838	0.15	1.496
M4	0.23	2.981	0.16	1.475
M3	0.21	3.050	0.15	1.522
M2	0.22	3.075	0.15	1.474
M1	0.22	2.924	0.16	1.495

Tab. 3.3.10 Slice 25 dose rates and HTR values TLD-600 and TLD-700

Slice 27 (Intestine)	TLD-600		TLD-700	
Chip ID	Dose Rate [mGy/d]	HTR	Dose Rate [mGy/d]	HTR
B6	0.25	3.172	0.18	1.499
B5	0.24	3.497	0.16	1.469
B4	0.26	3.679	0.14	1.496
B3	0.19	3.463	0.15	1.526
B2	0.20	3.176	0.15	1.532
B1	0.23	2.632	0.15	1.540
D7	0.24	3.575	0.18	1.474
D6	0.21	3.912	0.14	1.565
D5	0.24	3.948	0.15	1.505
D4	0.26	3.756	0.14	1.451
D3	0.26	3.695	0.15	1.494
D2	0.26	3.753	0.14	1.533
D1	0.25	3.080	0.15	1.530
F6	0.26	2.770	0.18	1.471
F4	0.24	2.905	0.17	1.529
F2	0.26	2.926	0.18	1.504
H2	0.28	3.798	0.15	1.474
H1	0.22	3.283	0.14	1.486
I3	0.24	3.518	0.15	1.468
I2	0.23	3.966	0.14	1.517
I1	0.24	4.061	0.16	1.498
L4	0.25	3.538	0.16	1.490
L3	0.25	3.824	0.15	1.461
L2	0.20	3.863	0.13	1.503
L1	0.26	3.770	0.14	1.540
N4	0.28	3.114	0.19	1.512
N3	0.23	3.305	0.17	1.502
N2	0.26	3.038	0.16	1.517
N1	0.23	2.809	0.18	1.511

Tab. 3.3.11 Slice 27 dose rates and HTR values TLD-600 and TLD-700

Slice 29	TLD-600		TLD-700	
Chip ID	Dose Rate [mGy/d]	HTR	Dose Rate [mGy/d]	HTR
B7	0.20	2.945	0.14	1.512
B6	0.21	3.264	0.13	1.485
B5	0.20	3.854	0.12	1.491
B4	0.20	3.620	0.12	1.486
B3	0.20	3.704	0.13	1.496
B2	0.21	3.494	0.13	1.471
B1	0.21	2.893	0.14	1.484
D8	0.20	3.261	0.14	1.519
D7	0.21	3.682	0.13	1.512
D6	0.21	3.851	0.12	1.456
D5	0.19	4.005	0.11	1.493
D4	0.20	3.975	0.11	1.493
D3	0.21	3.955	0.12	1.486
D2	0.20	3.588	0.12	1.498
D1	0.21	2.46	0.15	1.503
G2	0.20	3.860	0.12	1.517
G1	0.19	3.112	0.13	1.455
H4	0.18	3.188	0.13	1.499
H3	0.20	3.757	0.12	1.481
H2	0.19	3.817	0.11	1.496
H1	0.19	4.007	0.11	1.487
K7	0.22	3.224	0.13	1.494
K6	0.23	3.618	0.13	1.473
K5	0.20	4.027	0.11	1.473
K4	0.19	4.135	0.11	1.509
K3	0.20	3.870	0.11	1.560
K2	0.21	3.815	0.12	1.486
K1	0.21	3.282	0.13	1.506
M5	0.22	3.073	0.14	1.503
M4	0.22	3.340	0.14	1.521
M3	0.22	3.437	0.13	1.535
M2	0.21	3.432	0.15	1.525
M1	0.21	2.972	0.15	1.502

Tab. 3.3.12 Slice 29 dose rates and HTR values TLD-600 and TLD-700

Slice 31	TLD-600		TLD-700	
Chip ID	Dose Rate [mGy/d]	HTR	Dose Rate [mGy/d]	HTR
A3	0.18	2.967	0.16	1.490
A2	0.17	2.956	0.13	1.537
A1	0.20	2.873	0.15	1.522
C7	0.23	3.418	0.13	1.502
C6	0.24	3.818	0.12	1.500
C5	0.21	3.950	0.12	1.502
C4	0.17	3.989	0.12	1.512
C3	0.18	4.041	0.11	1.488
C2	0.19	3.744	0.11	1.529
C1	0.20	3.215	0.14	1.501
E8	—	—	—	—
E7	0.21	3.607	0.13	1.450
E6	0.19	3.832	0.11	1.568
E5	0.18	4.211	0.11	1.497
E4	0.19	4.158	0.11	1.505
E3	0.19	4.218	0.10	1.457
E2	0.22	4.058	0.11	1.504
E1	0.21	3.713	0.12	1.483
H2	0.20	3.857	0.12	1.532
H1	0.19	3.223	0.14	1.503
I4	0.24	3.325	0.17	1.519
I3	0.14	3.844	0.14	1.526
I2	0.19	4.016	0.10	1.478
I1	0.20	4.268	0.10	1.491
L7	0.25	3.570	0.16	1.543
L6	—	—	0.15	1.526
L5	0.25	3.940	0.16	1.530
L4	0.24	4.083	0.15	1.531
L3	0.28	4.187	0.15	1.521
L2	0.25	4.065	0.15	1.501
L1	0.26	3.656	0.15	1.541
N5	0.25	3.485	0.18	1.526
N4	0.26	3.655	0.16	1.524
N3	0.25	3.695	0.16	1.544
N2	0.29	3.684	0.17	1.520
N1	0.27	3.326	0.16	1.501

Tab. 3.3.13 Slice 31 dose rates and HTR values TLD-600 and TLD-700

Note: data for positions E8 (TLD-600 and TLD-700) and L6 (TLD-600) were unfortunately lost due to an error in the read-out process. Corresponding 3D plots have been interpolated to fill up the gaps.

Slice 33	TLD-600		TLD-700	
Chip ID	Dose Rate [mGy/d]	HTR	Dose Rate [mGy/d]	HTR
A5	0.25	2.609	0.15	1.501
A4	0.23	2.895	0.16	1.489
A3	0.24	2.825	0.17	1.522
A2	0.22	2.805	0.16	1.503
A1	0.26	2.455	0.17	1.505
C7	0.20	3.130	0.17	1.469
C6	0.24	3.309	0.14	1.694
C5	0.25	3.356	0.14	1.501
C4	0.20	3.342	0.14	1.527
C3	0.21	3.213	0.15	1.497
C2	0.25	3.243	0.17	1.512
C1	0.23	2.952	0.16	1.536
E7	0.20	3.152	0.16	1.523
E6	0.25	3.367	0.16	1.485
E5	0.21	3.423	0.15	1.517
E4	0.23	3.350	0.15	1.536
E3	0.21	3.256	0.15	1.489
E2	0.21	3.090	0.14	1.504
E1	0.21	3.125	0.13	1.540
F2	0.22	2.946	0.15	1.533
H4	0.23	3.023	0.14	1.538
H3	0.22	3.447	0.157	1.461
H2	0.23	3.508	0.15	1.452
H1	0.23	3.347	0.13	1.453
K7	0.24	3.117	0.16	1.499
K6	0.24	3.371	0.15	1.480
K5	0.21	3.349	0.15	1.548
K4	0.20	3.437	0.12	1.482
K3	0.23	3.350	0.12	1.503
K2	0.24	3.349	0.13	1.473
K1	0.22	3.176	0.15	1.527
M7	0.25	2.773	0.16	1.517
M6	0.22	3.131	0.14	1.512
M5	0.20	3.317	0.14	1.489
M4	0.24	3.254	0.14	1.511
M3	0.23	3.314	0.17	1.510
M2	0.19	3.117	0.15	1.471
M1	0.23	2.657	0.14	1.536

Tab. 3.3.14 Slice 33 dose rates and HTR values TLD-600 and TLD-700

3.4 NEUTRON DOSES MATROSHKA II A

^{60}Co equivalent absorbed doses from neutrons < 200 keV are given in the tables below. A gradient can be seen corresponding to the one observed in the organ dose boxes.

Slice 3 (Eye)	Neutrons	
Chip ID	Absorbed dose [mGy]	Contribution [%]
A2	17	22.7
A1	10	12.6
B5	17	24.8
B4	18	27.1
B3	16	24.2
B2	11	14.9
B1	23	34.7
C2	14	18.9
C1	24	37.5
D2	21	30.5
D1	24	36.4
E4	13	18.1
E3	19	28.6
E2	24	38.6
E1	19	29.7
F3	6	7.4
F2	14	20.2
F1	13	18.2

Tab. 3.4.1 Slice 3 absorbed neutron dose and relative contribution

Slice 7	Neutrons	
Chip ID	Absorbed dose [mGy]	Contribution [%]
A3	14	19.0
A2	9	12.1
A1	17	23.8
B2	18	25.1
B1	13	17.7
C2	19	27.6
C1	20	29.4
D2	21	31.2
D1	15	21.1
E3	19	27.5
E2	16	22.6
E1	12	18.1

Tab. 3.4.2 Slice 7 absorbed neutron dose and relative contribution

Slice 11	Neutrons	
Chip ID	Absorbed dose [mGy]	Contribution [%]
A4	18	22.7
A3	13	16.7
A2	14	19.5
A1	7	8.8
C4	22	28.0
C3	24	29.9
C2	26	33.7
C1	20	25.6
E4	6	6.3
E2	17	20.8
F2	30	40.4
F1	26	38.9
H4	12	16.5
H3	24	31.2
H2	25	33.9
H1	26	34.8

Tab. 3.4.3 Slice 11 absorbed neutron dose and relative contribution

Slice 13	Neutrons	
Chip ID	Absorbed dose [mGy]	Contribution [%]
A4	16	19.8
A3	18	22.0
A2	21	27.4
A1	20	23.6
C6	9	10.1
C5	10	11.3
C4	8	8.7
C3	23	31.2
C2	21	27.1
C1	8	9.2
E6	18	20.5
E5	10	10.5
E4	20	23.7
E3	32	44.4
E2	13	14.9
E1	20	25.3
F1	21	26.1
H1	19	24.4
I3	9	10.2
I2	20	26.6
I1	25	35.1
L6	0	0.0
L5	22	29.6
L4	23	28.3
L3	26	39.8
L2	26	41.6
L1	23	30.5
N5	21	26.2
N4	41	63.7
N3	28	37.9
N2	28	39.2
N1	40	58.5

Tab. 3.4.4 Slice 13 absorbed neutron dose and relative contribution

Slice 15 (Lung)		Neutrons
Chip ID	Absorbed dose [mGy]	Contribution [%]
A5	11	15.8
A4	19	28.9
A3	13	19.7
A2	14	21.5
A1	8	11.3
C7	17	26.4
C6	21	34.0
C5	14	21.2
C4	14	22.1
C3	14	23.0
C2	20	32.7
C1	15	21.4
E7	19	31.6
E6	22	34.3
E5	16	24.1
E4	19	33.5
E3	23	37.5
E2	22	37.7
E1	18	28.5
H2	17	28.3
H1	15	23.8
I3	16	23.8
I2	21	35.9
I1	20	34.9
L3	16	24.0
L2	12	18.0
L1	14	22.0
N6	14	21.8
N5	19	31.7
N4	19	29.8
N3	18	30.4
N2	22	36.9
N1	21	33.8

Tab. 3.4.5 Slice 15 absorbed neutron dose and relative contribution

Slice 17		Neutrons
Chip ID	Absorbed dose [mGy]	Contribution [%]
A4	12	14.1
A3	13	16.2
A2	11	13.0
A1	15	17.9
C7	25	33.5
C6	24	35.4
C5	8	9.6
C4	21	27.2
C3	15	19.1
C2	16	21.5
C1	19	24.3
E8	16	20.4
E7	18	24.8
E6	19	25.2
E5	27	37.1
E4	27	39.5
E3	24	34.4
E2	19	29.3
E1	10	14.7
H3	28	40.8
H2	26	37.6
H1	19	23.5
I3	20	27.0
I2	29	45.0
I1	23	33.8
L7	16	20.6
L6	10	12.2
L5	18	23.7
L4	31	41.9
L3	24	34.4
L2	9	11.7
L1	13	16.0
N7	9	10.7
N6	23	31.0
N5	23	31.3
N4	32	45.2
N3	24	32.9
N2	24	31.9
N1	14	17.9

Tab. 3.4.6 Slice 17 absorbed neutron dose and relative contribution

Slice 19	Neutrons	
Chip ID	Absorbed dose [mGy]	Contribution [%]
B7	18	28.6
B6	11	17.7
B5	20	33.3
B4	18	31.5
B3	15	24.6
B2	17	27.8
B1	24	38.1
D7	22	38.9
D6	13	21.6
D5	22	40.5
D4	21	38.8
D3	18	30.9
D2	23	39.0
D1	18	28.5
G2	23	42.0
G1	19	32.3
H3	16	26.1
H2	19	35.8
H1	22	42.2
K7	16	27.1
K6	22	41.2
K5	29	54.0
K4	22	42.9
K3	20	36.6
K2	15	25.7
K1	17	27.4
M6	16	24.2
M5	18	29.7
M4	22	34.9
M3	21	34.7
M2	20	32.9
M1	15	23.8

Tab. 3.4.7 Slice 19 absorbed neutron dose and relative contribution

Slice 21		Neutrons
Chip ID	Absorbed dose [mGy]	Contribution [%]
B6	20	31.5
B5	22	40.4
B4	21	36.7
B3	15	25.5
B2	19	34.5
B1	15	24.8
D7	16	23.5
D6	20	37.7
D5	29	58.2
D4	22	41.8
D3	25	46.0
D2	18	30.3
D1	21	36.5
G2	26	46.6
G1	23	40.5
H3	21	37.2
H2	27	52.2
H1	21	41.0
K7	6	8.6
K6	25	44.9
K5	18	32.4
K4	25	43.3
K3	23	43.8
K2	14	22.9
K1	9	13.7
M6	20	31.1
M5	15	23.6
M4	23	39.4
M3	27	47.2
M2	11	16.1
M1	6	9.4

Tab. 3.4.8 Slice 21 absorbed neutron dose and relative contribution

Slice 23	Neutrons	
Chip ID	Absorbed dose [mGy]	Contribution [%]
B6	15	21.8
B5	26	43.6
B4	22	35.1
B3	11	15.7
B2	24	37.6
B1	15	23.5
D7	18	28.8
D6	16	27.2
D5	26	48.0
D4	22	38.3
D3	23	40.2
D2	18	31.1
D1	14	21.5
G2	23	37.0
G1	18	30.5
H3	19	31.9
H2	19	31.8
H1	29	57.2
K7	12	18.6
K6	16	26.7
K5	16	28.0
K4	23	41.9
K3	19	32.8
K2	20	35.0
K1	14	20.9
M4	18	27.4
M3	15	22.2
M2	19	30.8
M1	21	34.5

Tab. 3.4.9 Slice 23 absorbed neutron dose and relative contribution

Slice 25	Neutrons	
Chip ID	Absorbed dose [mGy]	Contribution [%]
B6	18	26.5
B5	19	29.5
B4	22	37.2
B3	24	39.7
B2	16	25.7
B1	22	33.7
D7	24	39.0
D6	17	28.4
D5	25	43.9
D4	26	46.9
D3	21	35.1
D2	23	38.5
D1	13	18.8
G2	28	49.0
G1	19	31.0
H3	18	29.5
H2	27	48.2
H1	23	41.2
K7	25	39.3
K6	29	50.6
K5	17	27.3
K4	21	38.2
K3	24	42.9
K2	20	32.7
K1	19	28.2
M4	15	22.3
M3	11	16.6
M2	18	28.4
M1	11	16.0

Tab. 3.4.10 Slice 25 absorbed neutron dose and relative contribution

Slice 27 (Intestine)		Neutrons
Chip ID	Absorbed dose [mGy]	Contribution [%]
B6	14	18.3
B5	19	28.3
B4	31	49.0
B3	6	9.8
B2	12	18.5
B1	17	26.1
D7	13	17.5
D6	17	26.6
D5	23	35.0
D4	30	47.0
D3	28	41.1
D2	33	53.6
D1	26	40.4
F6	20	25.9
F4	15	20.7
F2	17	21.8
H2	37	57.3
H1	23	36.8
I3	23	34.7
I2	24	37.3
I1	18	26.4
L4	23	32.0
L3	25	37.5
L2	18	30.6
L1	33	52.1
N4	21	26.5
N3	12	16.7
N2	27	38.3
N1	10	12.6

Tab. 3.4.11 Slice 27 absorbed neutron dose and relative contribution

Slice 29	Neutrons	
Chip ID	Absorbed dose [mGy]	Contribution [%]
B7	13	20.6
B6	20	34.6
B5	22	40.7
B4	18	32.4
B3	20	34.8
B2	22	38.0
B1	17	26.7
D8	13	19.9
D7	22	37.4
D6	25	44.6
D5	21	42.6
D4	28	55.6
D3	24	43.1
D2	21	38.9
D1	13	20.3
G2	20	36.2
G1	16	28.3
H4	11	18.3
H3	22	40.5
H2	21	41.4
H1	22	42.9
K7	22	36.7
K6	29	51.1
K5	23	42.9
K4	23	44.9
K3	25	47.5
K2	26	47.2
K1	22	37.0
M5	22	35.7
M4	22	36.9
M3	26	45.6
M2	16	24.0
M1	16	23.9

Tab. 3.4.12 Slice 29 absorbed neutron dose and relative contribution

Slice 31	Neutrons	
Chip ID	Absorbed dose [mGy]	Contribution [%]
A3	N/A	N/A
A2	8	13.7
A1	11	16.4
C7	26	43.3
C6	32	57.5
C5	25	44.9
C4	10	19.3
C3	20	39.2
C2	21	40.3
C1	14	23.2
E8	N/A	N/A
E7	20	34.2
E6	22	42.0
E5	20	40.2
E4	22	45.4
E3	25	50.1
E2	29	56.2
E1	26	49.3
H2	19	34.2
H1	10	16.9
I4	17	23.8
I3	N/A	N/A
I2	23	46.9
I1	26	52.4
L7	24	34.2
L6	N/A	N/A
L5	25	36.3
L4	25	38.6
L3	36	54.7
L2	26	39.2
L1	29	42.9
N5	18	24.0
N4	24	33.8
N3	23	33.4
N2	34	46.6
N1	27	37.4

Tab. 3.4.13 Slice 31 absorbed neutron dose and relative contribution

Note: data for positions E8 (TLD-600 and TLD-700) and L6 (TLD-600) were unfortunately lost due to an error in the read-out process.

Slice 33	Neutrons	
Chip ID	Absorbed dose [mGy]	Contribution [%]
A5	27	40.7
A4	16	23.3
A3	17	23.7
A2	13	19.6
A1	21	27.8
C7	1	1.7
C6	29	49.6
C5	32	52.3
C4	17	29.7
C3	13	19.7
C2	20	27.1
C1	16	22.5
E7	5	7.0
E6	20	28.5
E5	16	24.8
E4	20	31.7
E3	10	14.5
E2	19	31.0
E1	21	35.1
F2	15	23.5
H4	24	39.9
H3	16	23.7
H2	19	28.7
H1	28	49.2
K7	21	31.2
K6	23	34.4
K5	11	16.0
K4	20	35.8
K3	32	59.2
K2	29	48.9
K1	16	24.2
M7	24	33.5
M6	19	30.0
M5	11	17.4
M4	26	40.4
M3	11	14.7
M2	8	12.4
M1	24	37.9

Tab. 3.4.14 Slice 33 absorbed neutron dose and relative contribution

3.5 PONCHO ABSORBED DOSES MATROSHKA II A

The detailed data for the six poncho boxes (mid thorax, upper abdomen, lateral right and left sides, mid dorsal and lumbar) are presented below. The same procedure as in section 3.4 was used. For reference neutron doses are included in the charts below.

Dose	TLD-600 [mGy]	±[σ]	TLD-700 [mGy]	±[σ]	TLD-300 [mGy]	±[σ]	Neutrons [mGy]	[%]
Poncho #1	89.47	3.43	85.10	8.22	87.31	6.31	4.48	5.26
Poncho #2	88.96	6.87	92.73	3.52	86.57	7.12	N/A	N/A
Poncho #3	96.87	7.16	90.28	2.77	88.37	3.57	6.51	7.21
Poncho #4	89.02	2,19	83.98	5.30	88.44	7.55	5.16	6.15
Poncho #5	90.52	4.67	79.89	4.46	87.89	8.24	10.55	13.21
Poncho #6	93.75	4.14	81.63	5.22	79.45	8.18	12.11	14.84

Tab. 3.5.1 Mean absorbed doses (mGy) and standard deviations σ (mGy) (no background correction).

Note: For Poncho #2 TLD-700 chips show a dose equal within statistical uncertainty to TLD-600.

Dose	TLD-600 [mGy/d]	±[σ]	TLD-700 [mGy/d]	±[σ]	TLD-300 [mGy/d]	±[σ]
Poncho #1	0.24	0.01	0.23	0.02	0.24	0.02
Poncho #2	0.24	0.02	0.25	0.01	0.24	0.02
Poncho #3	0.26	0.02	0.24	0.01	0.24	0.01
Poncho #4	0.24	0.01	0.23	0.01	0.24	0.02
Poncho #5	0.24	0.01	0.22	0.01	0.24	0.02
Poncho #6	0.25	0.01	0.22	0.01	0.21	0.02

Tab. 3.5.2 Mean absorbed dose rates (mGy) and standard deviations σ (mGy) (background corrected)

The neutron component is much lower than for the organ dose boxes and the distribution more uniform (considering the standard deviations given). The reason for this can be found in the neutron moderating properties of the water rich tissues of the human body causing an increased detection by TLD-600 and further secondary neutron radiation.

3.6 ORGAN ABSORBED DOSES MATROSHKA II A

Detailed data on the absorbed doses of the five boxes at the sites of radiosensitive organs (eye, lung, stomach, kidney and intestine) and the sixth box on top of the head are presented in this section.

Four TLDs of each type (TLD-300, TLD-600 and TLD-700) were installed in the boxes. For TLD-300 peak 5 was used. Since the positions of the TLDs were different a mean dose value was therefore obtained and taken as the organ absorbed dose. A standard deviation σ is given for each mean. The background dose has not been accounted for in the overall but in the mean dose rates.

The neutron component was extracted using the pair method (see section 2.4). The lowest level (~5%) can be observed for the head box following a steady gradient throughout the lower body parts -with the exception of the kidney - reaching its highest level at the intestine box (~30%). Therefore (secondary) thermal neutron radiation plays an important part in the composition of radiation exposure of organs in the abdominal region.

Tables 3.6.1 – 3.6.2 show the absorbed doses and the mean dose rates

Dose	TLD-600		TLD-700		TLD-300		Neutrons	
	[mGy]	±[σ]	[mGy]	±[σ]	[mGy]	±[σ]	[mGy]	[%]
Eye	80.61	3.22	72.93	7.87	75.20	3.74	7.68	10.53
Lung	75.06	4.37	67.81	8.19	64.04	4.67	7.32	10.80
Stomach	79.70	7.94	64.22	5.71	65.49	2.75	15.50	24.14
Kidney	76.91	7.36	66.05	1.72	62.43	1.62	10.57	16.00
Intestine	81.63	4.46	61.94	7.04	63.34	7.07	19.79	31.96
Head	86.20	4.19	81.76	9.26	79.92	3.61	4.48	5.48

Tab. 3.6.1 Mean absorbed doses (mGy) and standard deviations σ (mGy) (no background correction)

Dose	TLD-600		TLD-700		TLD-300	
	[mGy/d]	±[σ]	[mGy/d]	±[σ]	[mGy/d]	±[σ]
Eye	0.21	0.01	0.20	0.02	0.20	0.01
Lung	0.20	0.01	0.18	0.02	0.17	0.01
Stomach	0.21	0.02	0.17	0.02	0.17	0.01
Kidney	0.20	0.02	0.18	0.01	0.16	0.004
Intestine	0.22	0.01	0.16	0.02	0.17	0.02
Head	0.23	0.01	0.22	0.03	0.22	0.01

Tab. 3.6.2 Mean absorbed dose rates (mGy) and standard deviations σ (mGy) (background corrected)

3.7 DATA INTERCOMPARISON

To provide a clear picture of the different radiation levels for crew members for EVAs and IVAs the following figure (3.7.1) is best used for illustration. As has been mentioned earlier while writing this thesis data from Matroshka Phase II B became available and is therefore included.

To summarize a few main results have to be particularly stressed:

- A factor of roughly two on observed dose rates distingishes the EVA to the IVAs exposures. Since albedo effects and the orientation of Matroshka with respect to the spacecraft are to be taken into account the head received a much higher dose than the rest of the phantom in Phase A [25].

- Thermal and intermediate neutrons play a major role for the TLD-600 signal detected during IVAs. The neutrons generated in the hull of the spacecraft get thermalised inside the phantom and a steep gradient can be found which roughly doubles the neutron dose for the inner tissues and organs [25].

- As for the IVAs the absorbed dose rates are of the same levels. The gradient experienced in Zvezda is flatter than for Pirs indicating an increase in structural shielding mass. This causes a build up of secondary neutrons which compensates for the flatter does gradient found in Zvezda. Furthermore it is apparent that the phantom was stored with the left side facing the hull as a slight gradient can be seen for all slices [25].
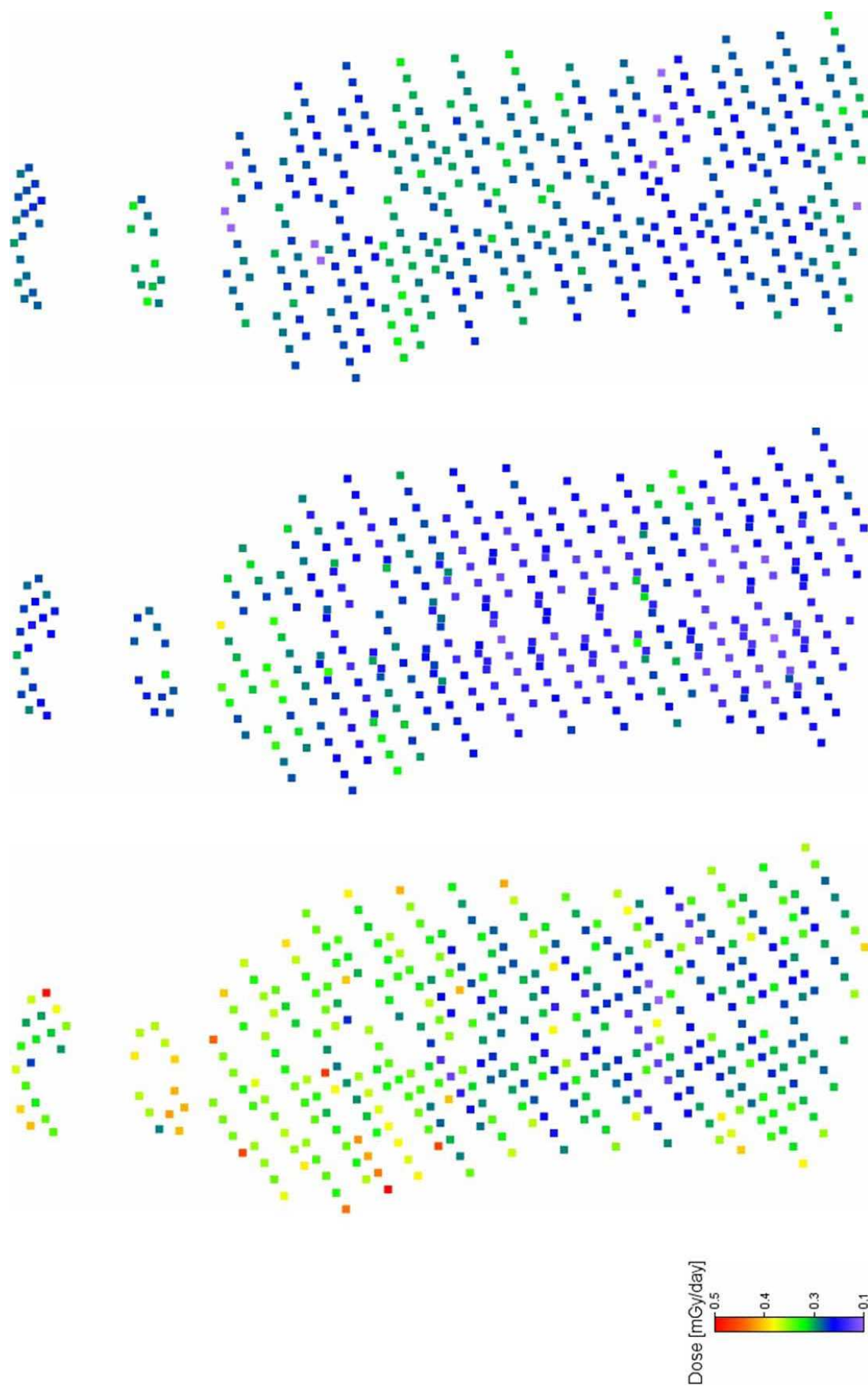
Fig. 3.7.1 Dose rate profiles for Matroshka Phase I (bottom), II A (middle) and Phase II B (top) [25].

The Matroshka Experiment aimed at determining the radiation exposures to astronauts operating inside and outside of space vessels in LEO. For a prolonged and permanent human presence in space risks associated with exposure to ionizing radiation have to be quantified as precisely as possible.

It is therefore paramount to gain widespread data through means of different analytical tools to deepen our knowledge of the radiation environment in LEO (and beyond).

Using the Matroshka phantom a detailed picture of dose profiles for EVAs and IVAs over an extended period of time in LEO could be gained. A few distinctive conclusions can be drawn from the data presented in the previous sections.

- The **dose rates** are well below the recommended dose limitation guidelines (see section 1.3.2) in the frame of current mission planning i.e. for a typical 6 month stay onboard the ISS.
  If the presence of a single individual is to be lengthened in time significantly, however, new ideas in spacecraft design and radiation protection have to emerge to make a prolonged (several years without interruption) stay feasible. This applies to missions not only in LEO but beyond and presents a substantial challenge for any mission to Mars or a permanent lunar habitat.

- The **skin dose** can be taken as conservative estimate for the total body exposure. Although thermal and intermediate neutrons play a significant part for IVAs and LET naturally increases as particles traverse human tissue, no hotspots could be found.

- **EVAs** account for roughly double dose rates than IVAs; higher deviations are observed for the skin dose (2.5 – 3 times higher) and lower ones for the organs with the exception of the eyes. Neutrons play a very small role since no significant shielding mass is present for a spacewalk.

- As for **IVAs** the exact location of the crew is relevant especially for the neutron component. This has to be considered for the allocation of sleeping quarters. Any outer hull shielding attempt results in a cascade of secondaries that create a highly complex radiation environment inside a spacecraft. Additionally equipment and further installations represent additional interaction mass and cause albedo effects.

- **Thermal and intermediate neutrons** (<200 keV) which can be detected by TLDs using the pair method are produced as secondary particles. The dose contribution builds up inside a human body and makes up to a third of total measured organ doses.

The strength of the Matroshka experiment lies in its complimentary approach regarding participating groups from all over the world and different analytical methods applied to a highly developed human phantom torso. Thermoluminescence and nuclear track dosimetry were the only methods applied for Matroshka Phase II A but it has been shown [21] that the results converged to give a yet unprecedented model of radiation exposure to crews on long term missions in LEO.
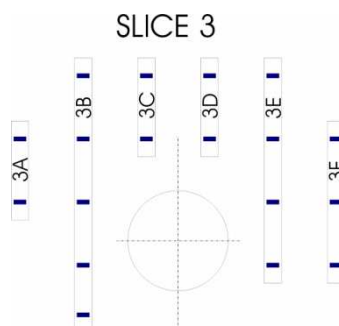
Fig. A.1. Distribution of detector tubes within the Matroshka phantom slice 3; cut-outs for integration of the eye organ box and a SSD.

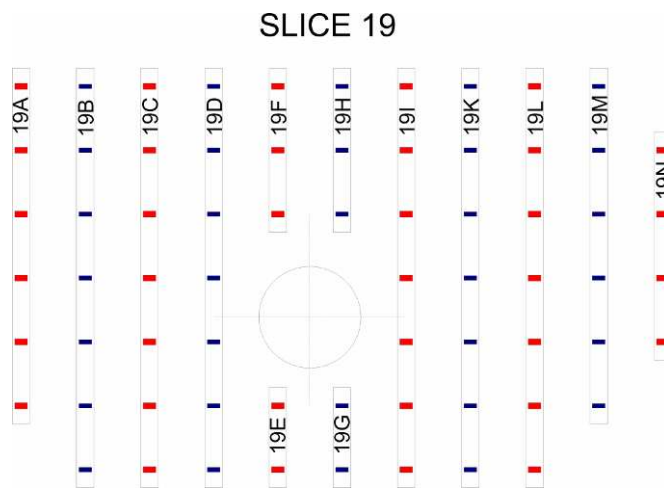**Fig. A.2.** Distribution of detector tubes within the Matroshka phantom slice 7 .

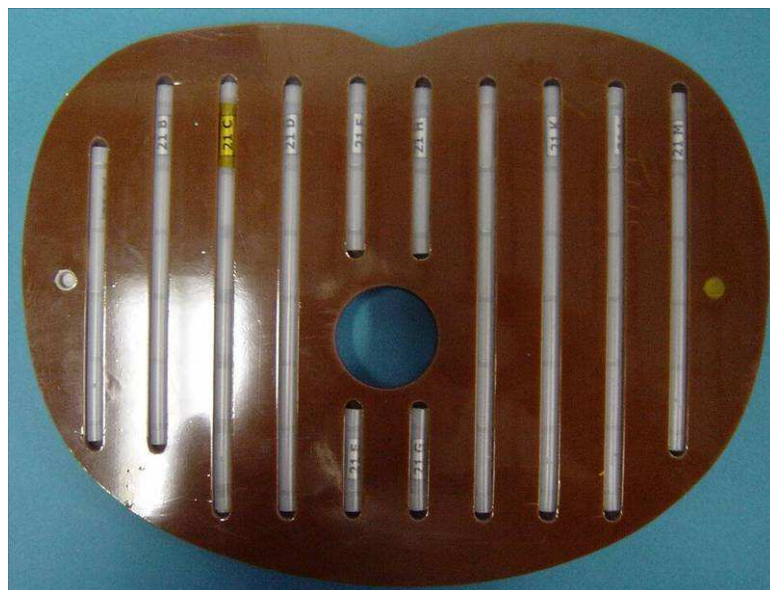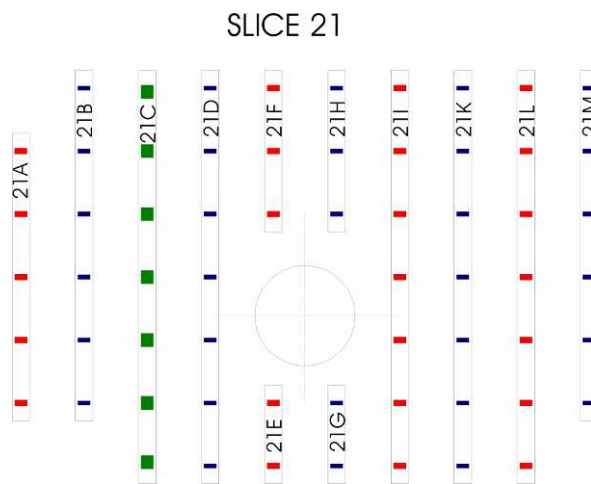**Fig. A.3.** Distribution of detector tubes within the Matroshka phantom slice 11.
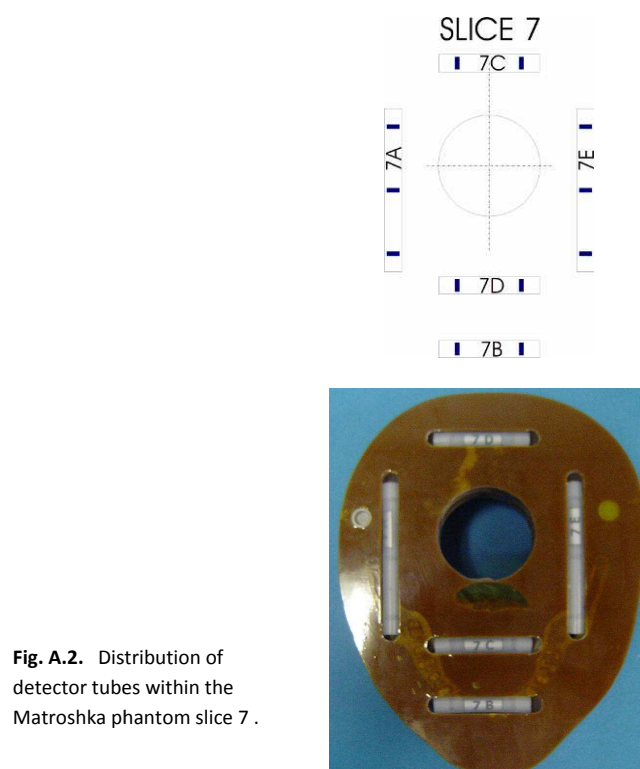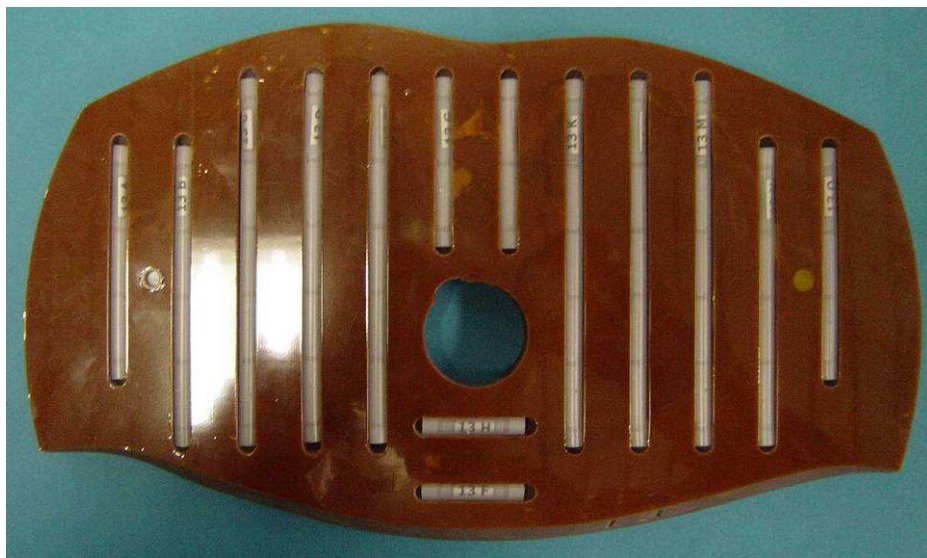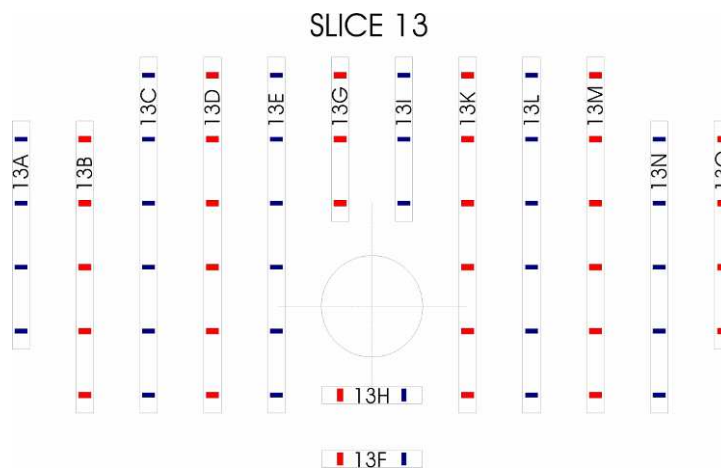
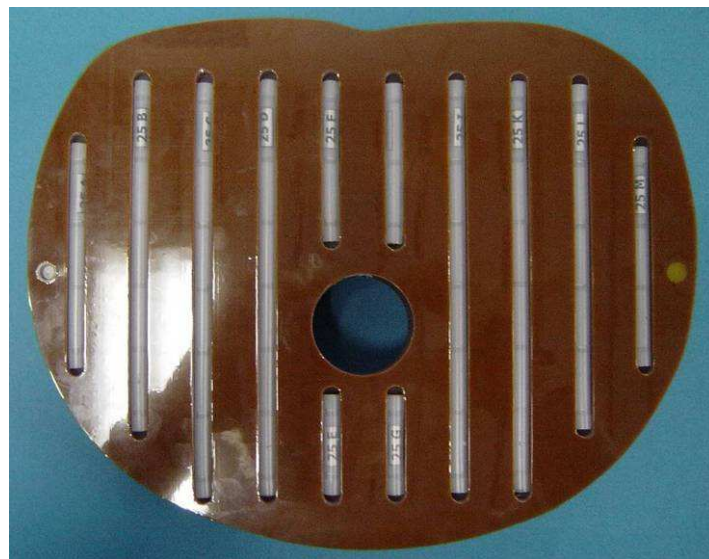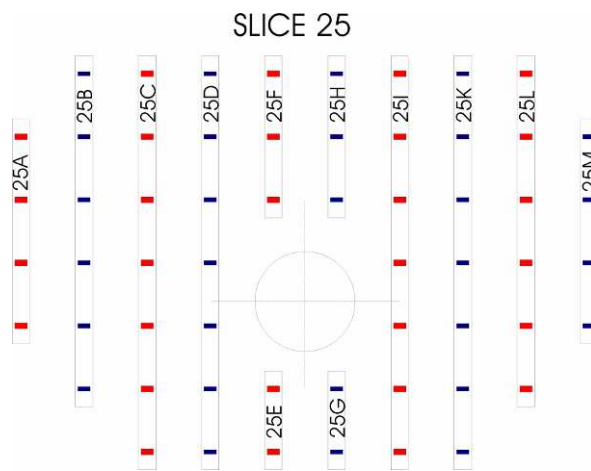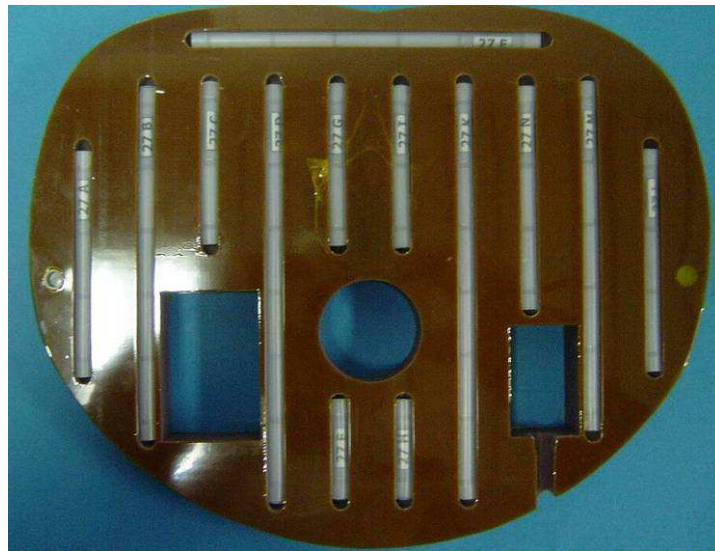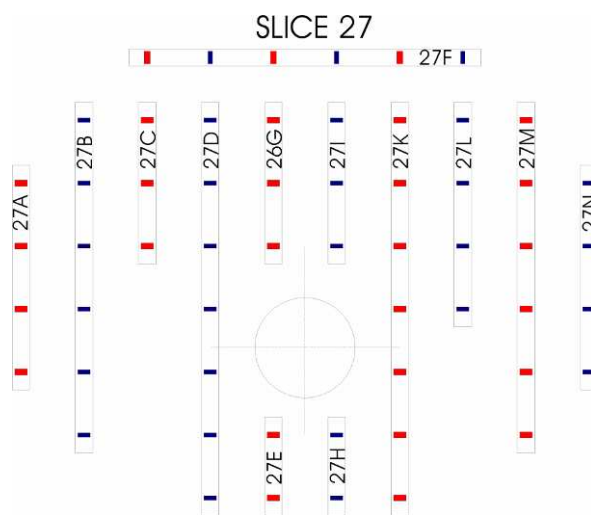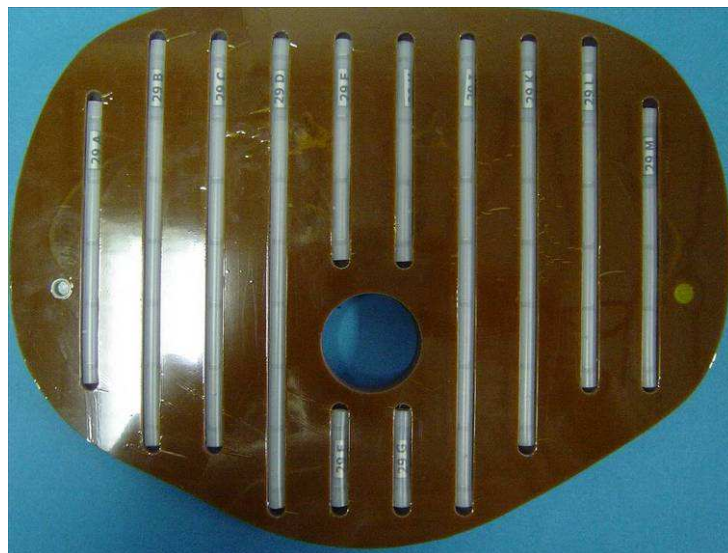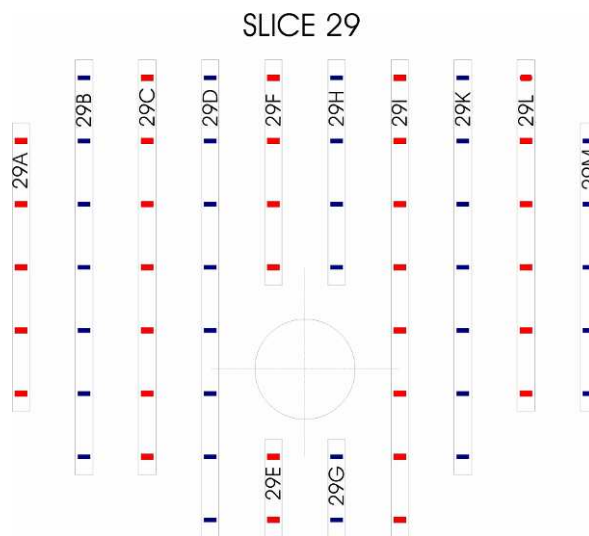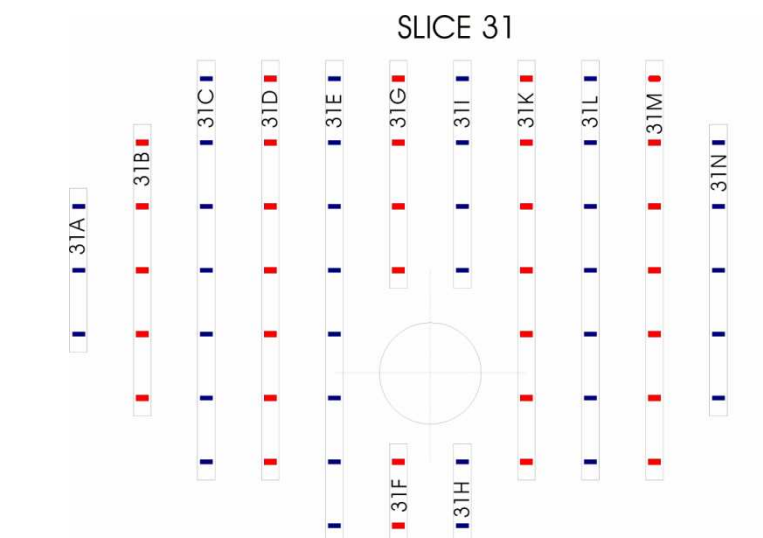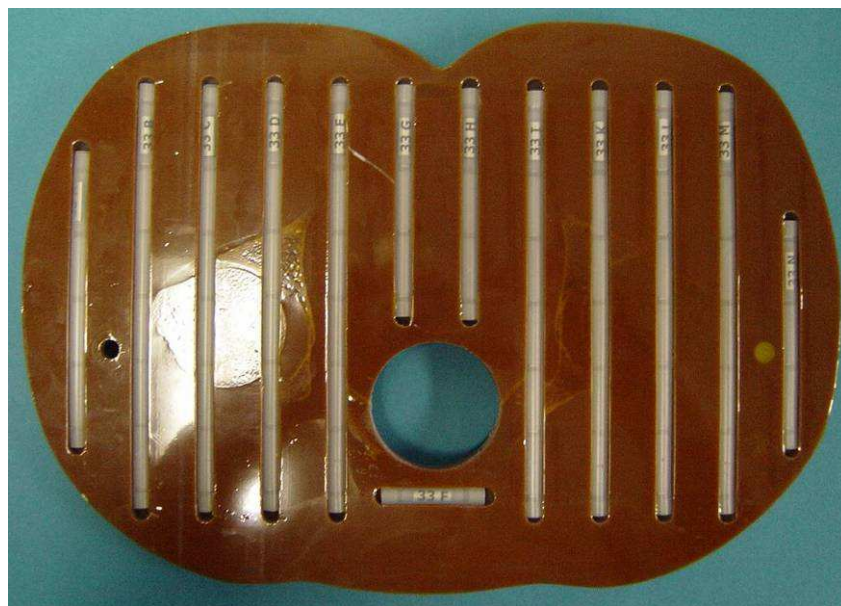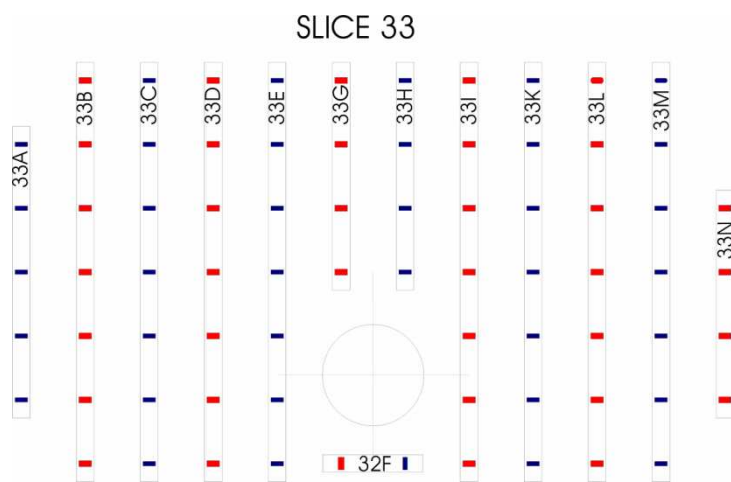**Fig. A.4.** Distribution of detector tubes within the Matroshka phantom slice 13.
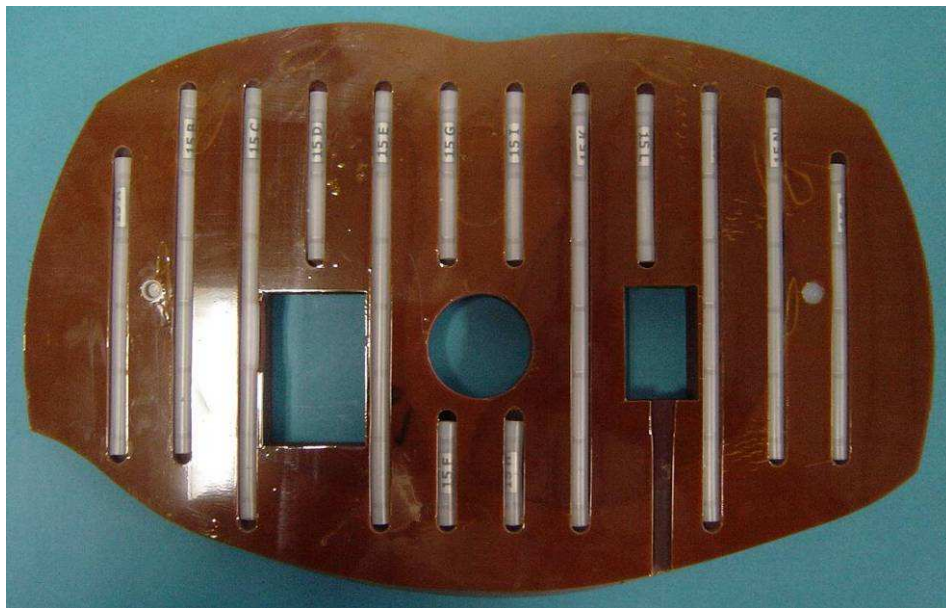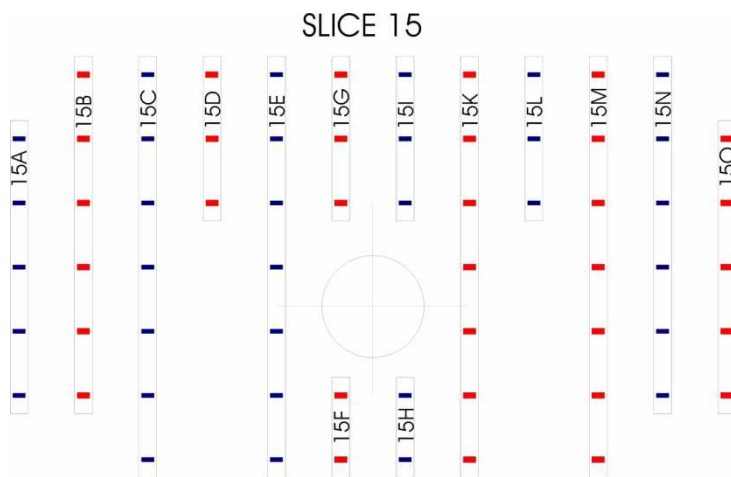
Fig. A.5. Distribution of detector tubes within the Matroshka phantom slice 15; cut-outs for integration of the lung organ box and a SSD.
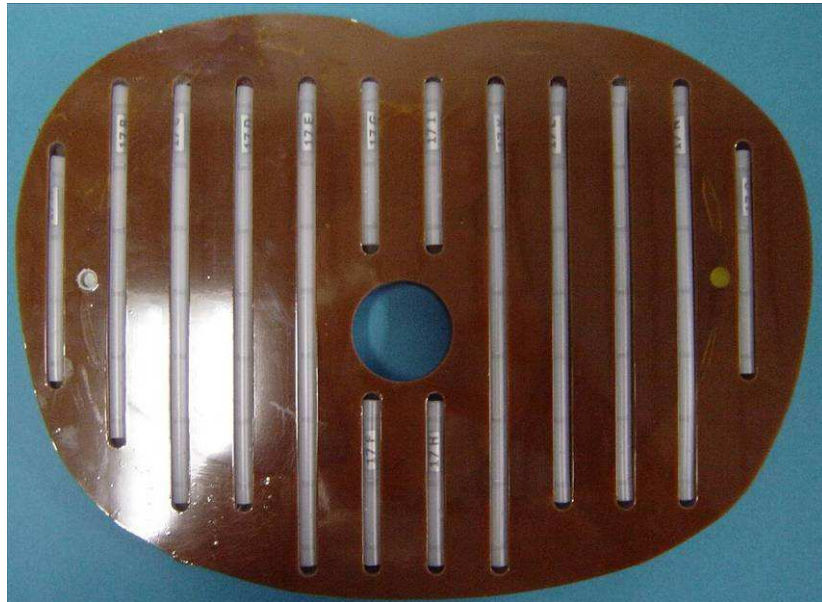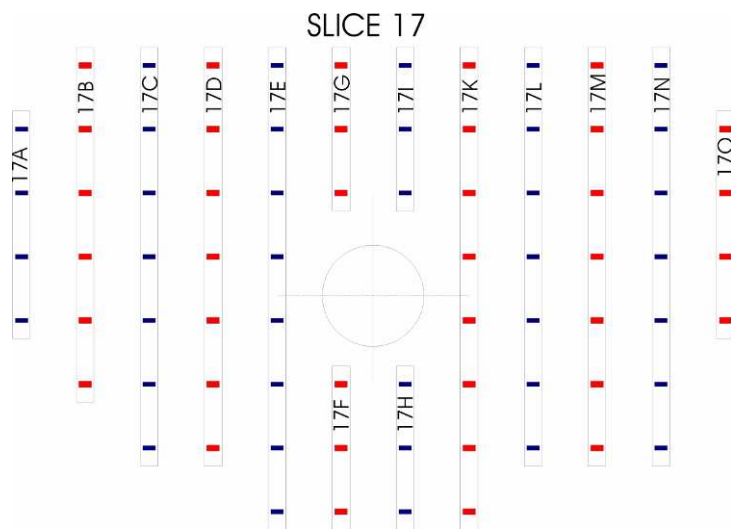
SLICE 17

Fig. A.6. Distribution of detector tubes within the Matroshka phantom slice 17.
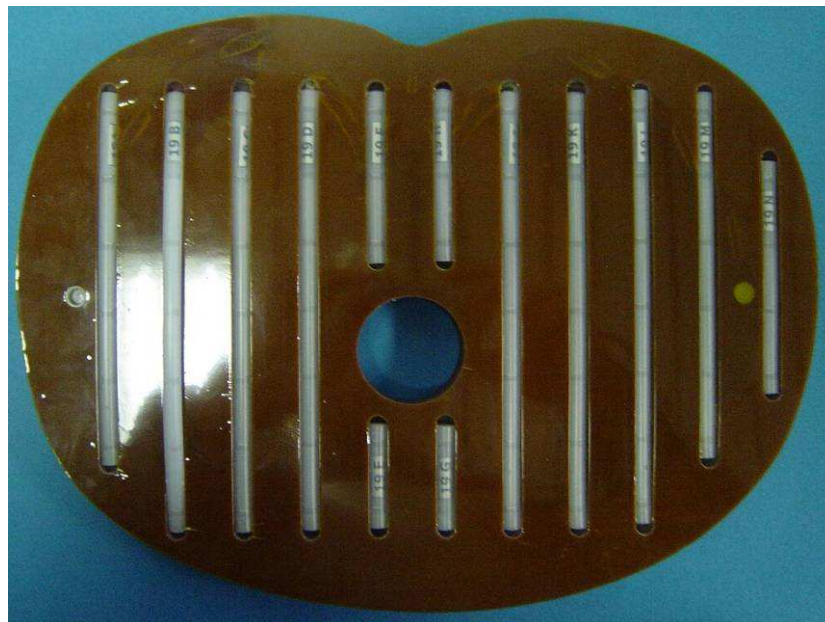
Fig. A.7. Distribution of detector tubes within the Matroshka phantom slice 19.

SLICE 21

Fig. A.8. Distribution of detector tubes within the Matroshka phantom slice 21.

Fig. A.9. Distribution of detector tubes within the Matroshka phantom slice 23.

Fig. A.10. Distribution of detector tubes within the Matroshka phantom slice 25.

Fig. A.11. Distribution of detector tubes within the Matroshka phantom slice 27; cut-outs for integration of the intestine organ box and a SSD.

Fig. A.12. Distribution of detector tubes within the Matroshka phantom slice 29.

Fig. A.13. Distribution of detector tubes within the Matroshka phantom slice 31.

Fig. A.14. Distribution of detector tubes within the Matroshka phantom slice 33.
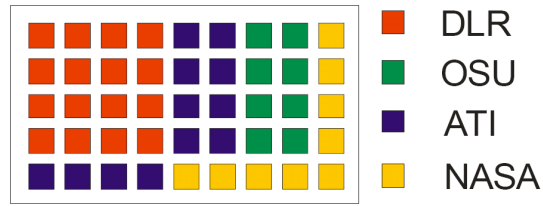
Fig. A.15. TL detector distribution for Matroshka eye organ box in slice 3
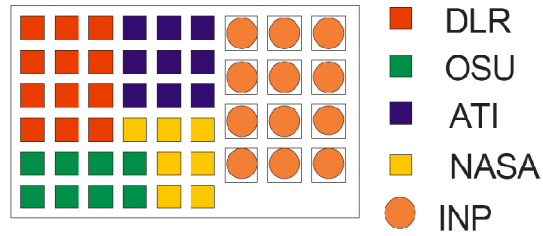
Fig. A.16. TL detector distribution for Matroshka lung organ box in slice 15
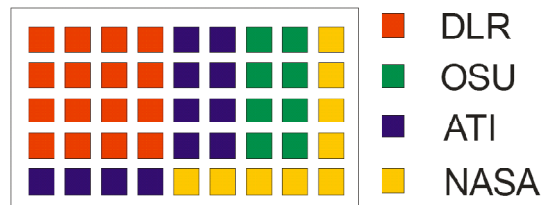
Fig. A.17. TL detector distribution for Matroshka stomach organ box in slice 20
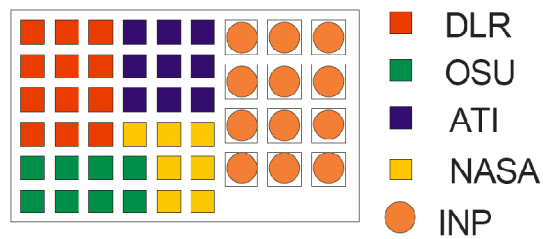
Fig. A.18. TL detector distribution for Matroshka kidney organ box in slice 22
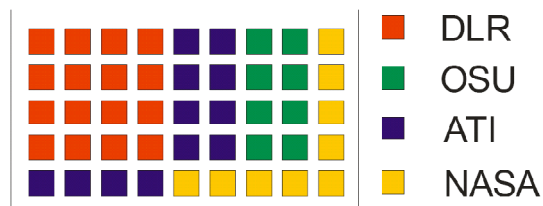
Fig. A.19. TL detector distribution for Matroshka intestine organ box in slice 27
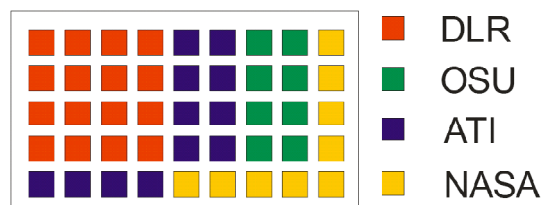
Fig. A.20. TL detector distribution for Matroshka detector box on top of the head
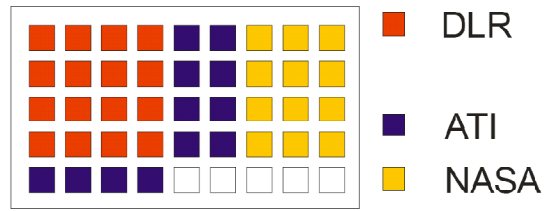
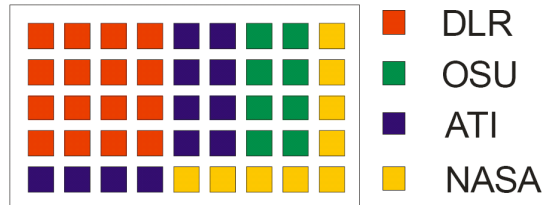**Fig. A.21.** TL detector distribution for Matroshka poncho detector box 1

Fig. A.22. TL detector distribution for Matroshka poncho detector box 2
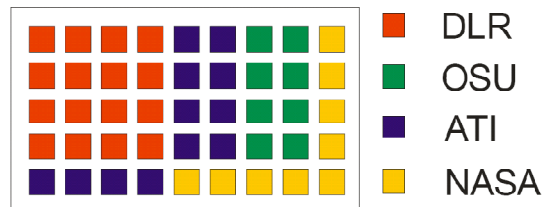

Fig. A.23. TL detector distribution for Matroshka poncho detector box 3
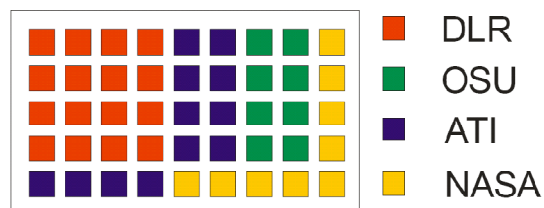

Fig. A.24. TL detector distribution for Matroshka poncho detector box 4
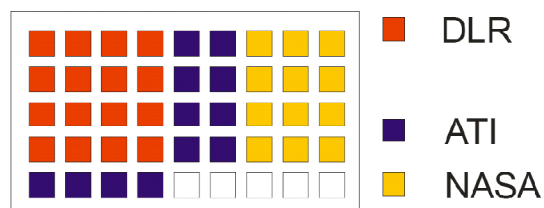

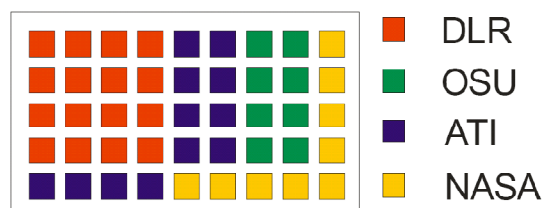**Fig. A.25.** TL detector distribution for Matroshka poncho detector box 5

Fig. A.26. TL detector distribution for Matroshka poncho detector box 6

117

6 REFERENCES

[1]   Inter-Agency Space Debris Coordination Committee, *IADC- 02/01: IADC Space Debris Mitigation Guidelines*. Oct. 2001.

[2]   National Council on Radiation Protection and Measurements, *NCRP Report No. 132: Radiation Protection Guidance for Activities in Low-Earth Orbit*. Bethesda, Maryland : NCRP ,Dec. 2000.

[3]   E.R. Benton and E.V. Benton, "Space Radiation Dosimetry in Low-Earth Orbit and beyond," *Nuclear Instruments and Methods in Physics Research B*, vol. 184, pp. 255-294, June 2001.

[4]   G.D. Badhwar, V.V. Kushin, Yu A. Akatov and V.A. Myltseva," Effects of Trapped Proton Flux anisotropy on Dose Rates in Low Earth Orbit," *Radiation Measurements*, vol. 30, pp. 415-426, Feb. 1999.

[5]   NASA Facts, FS-2002-10-080-JSC, *Understanding Space Radiation*. Lyndon B. Johnson Space Center, Houston Texas: NASA , Oct. 2002.

[6]   W. Stolz, *Radioaktivität: Grundlagen – Messung – Anwendungen*, 5th Edition. Wiesbaden: B.G. Teubner Verlag/ GWV Fachverlage GmbH, 2005, pp. 87-111.

[7]   G.Reitz, R.Facius and H.Sandler, "Radiation Protection in Space," *Acta Astronautica*, vol.35, No. 4/5, pp.313-338, 1995.

[8]   M. Stanford, J.A. Jones, "Space Radiation Concerns for Manned Exploration", *Acta Astronautica*, vol. 45, pp.39-47, Jan. 1999.

[9]   P. Spillantini et al., "Shielding from Cosmic Radiation for Interplanetary Missions: Active and Passive Methods," *Radiation Measurements*, vol. 42, pp.14-23, 2007.

[10]   National Aeronautic and Space Administration (NASA), "NASA-International Space Station," *NASA*, 2010 [online] Available: http://www.nasa.gov/mission_pages/station/main/index.html [Accessed: Jan. 6, 2010].

[11]   National Aeronautic and Space Administration (NASA), "Press Kit April 2011: Expedition 27 and 28 Stocking the Sation" NASA, April 2011, [online] Available: http://www.nasa.gov/pdf/537988main_ex27_28_pk_042211.pdf [Accessed: April. 28, 2011].

[12]   National Aeronautic and Space Administration (NASA), "The Space Shuttle's Return to Flight: Mission STS-114 Press Kit" NASA, July 2005, [online] Available: http://www.nasa.gov/pdf/112301main_114_pk_july05.pdf [Accessed: Jan. 6, 2010].

[13]   National Aeronautic and Space Administration (NASA), "NASA-International Space Station," *NASA*, 2010 [online] Available: http://www.nasa.gov/mission_pages/station/structure/elements/pirs.html [Accessed: April 28, 2011].

[14]   NASA Facts, IS-1999-09-ISS019JSC, *The Service Module: A Cornerstone of Russian International Space Station Modules*. Lyndon B. Johnson Space Center, Houston Texas: NASA , Jan. 1999.

[15]   J. Dettmann, G. Reitz, G. Gianfiglio, „MATROSHKA-The First ESA external PAYLOAD on the International Space Station," *Acta Astronautica*, vol. 60, pp.17-23, Sept. 2006.

[16]   G. Reitz et al., "Astronaut's Organ Doses Inferred from Measurements in a Human Phantom Outside the International Space Station," *Radiation Research*, vol. 171, pp.225-235, 2009.

[17] Y.S. Horowitz, O. Avila, M. Rodriguez-Villafuerte, "Theory of Heavy Charged Particle Response (Efficiency and Supralinearity) in TL Materials," *Nuclear Instruments and Methods in Physics Research B*, vol. 184, pp.85-112, March 2001.

[18] A.J.J Bos, "Theory of Thermoluminescence," *Radiation Measurements*, vol. 41, pp.45-56, 2007.

[19] S.W.S McKeever, *Thermoluminescence of Solids*. Cambridge: Cambridge University Press, 1985, pp.206-235.

[20] N. Vana, R. Erlach, M. Fugger, W. Gratzl and I. Reichhalter, "A computerized TL-Readout System for Dating and Phototransfer Measurements," *Nuclear Tracks Radiation Measurements*, vol. 14, p 181, 1988.

[21] M. Hajek, N. Vana, "Radiation Dose Distribution within the Matroshka Human Phantom Torso onboard ISS," Vienna University of Technology Atomic Institute of the Austrian Universities, Vienna, Austria, Tech. Rep. Final Report Phase A AIAU 27602, 2007.

[22] Human Model MATROSHKA for Radiation Exposure Determination of Astronauts (HAMLET), "Matroshka Timeline," *HAMLET* [online] Available: http://www.fp7-hamlet.at/index.php/matroshka/timeline [Accessed: March 11, 2010].

[23] T.Berger and M.Hajek, "On the linearity of the high-temperature emission from ^{7}LiF:Mg,Ti (TLD-700)," *Radiation Measurements*, vol.43, pp.1467-1473, 2008.

[24] M.Hajek et al., "LET dependence of Thermoluminescent Efficiency and Peak Height Ration of CaF$_2$:Tm ," *Radiation Measurements,* vol. 43 pp.1135 – 1139, 2008.

[25] R. Bergmann, M. Hajek, N. Vana, "RADIS: Study of Depth Dose Distribution inside a Human Phantom Using the MATROSHKA Facility Onboard the Russian Segment of the International Space Station," Vienna University of Technology Institute of Atomic and Subatomic Physics, Vienna, Austria, Final Report Phase 2: Exposure Onboard Zvezda ASAP-WV-215/05, 2009.

[26] M.L. Alexander, "Radiation Damage in the Developing Germ Cell of Drosophila Virilis from Fast Neutrons Treatment," *Genetics* vol. 43(3), pp. 458-469, 1958.

[27] International Commission on Radiological Protection, *ICRP Publication 60, Annals of the ICRP 21: Recommendations of the International Commission on Radiological Protection.* New York: ICRP, 1990.

[28] T. Berger, M. Hajek, "HAMLET WP3 D3.1 Phantom Data Intercomparison I," Vienna University of Technology Institute of Atomic and Subatomic Physics, Vienna, Austria and German Aerospace Center Institute of Aerospace Medicine Radiation Biology, Cologne, Germany, review report HAMLET-WP3-D3.1-001, 2010.

[29] T. Berger, M. Hajek, "HAMLET WP3 D3.3 Passive Data Intercomparison I, " Vienna University of Technology Institute of Atomic and Subatomic Physics, Vienna, Austria and German Aerospace Center Institute of Aerospace Medicine Radiation Biology, Cologne, Germany, review report HAMLET-WP3-D3.3-003, 2010.

[30] T. Berger, M. Hajek, "HAMLET WP3 D3.5 Active Data Intercomparison I," Vienna University of Technology Institute of Atomic and Subatomic Physics, Vienna, Austria and German Aerospace Center Institute of Aerospace Medicine Radiation Biology, Cologne, Germany, review report HAMLET-WP3-D3.5-001, 2010.

[31] M. Hajek, "Radiation exposure of space and aircrew," presented at third European IRPA Congress, 2010, Helsinki, Finland. 2010.